9-15-2011

Phase History Decomposition for Efficient Scatterer Classification in SAR Imagery

Dane F. Fuller

PHASE HISTORY DECOMPOSITION FOR EFFICIENT SCATTERER CLASSIFICATION IN SAR IMAGERY

DISSERTATION

Dane F. Fuller, Lieutenant Colonel, USAF

AFIT/DEE/ENG/11-09

DEPARTMENT OF THE AIR FORCE
AIR UNIVERSITY

AIR FORCE INSTITUTE OF TECHNOLOGY

Wright-Patterson Air Force Base, Ohio

The views expressed in this document are those of the author and do not reflect the official policy or position of the United States Air Force, the United States Department of Defense or the United States Government.

AFIT/DEE/ENG/11-09

PHASE HISTORY DECOMPOSITION FOR EFFICIENT SCATTERER CLASSIFICATION IN SAR IMAGERY

DISSERTATION

Presented to the Faculty

Graduate School of Engineering and Management

Air Force Institute of Technology

Air University

Air Education and Training Command

in Partial Fulfillment of the Requirements for the

Degree of Doctor of Philosophy

Dane F. Fuller, B.S.E.E., M.S.E.E.

Lieutenant Colonel, USAF

15 September 2011

APPROVED FOR PUBLIC RELEASE; DISTRIBUTION UNLIMITED

AFIT/DEE/ENG/11-09

PHASE HISTORY DECOMPOSITION FOR EFFICIENT SCATTERER CLASSIFICATION IN SAR IMAGERY

Dane F. Fuller, B.S.E.E., M.S.E.E.
Lieutenant Colonel, USAF

Approved:

//signed//	04 September 2011
Maj Michael A. Saville, PhD Dissertation Advisor	Date
//signed//	04 September 2011
Dr. Richard K. Martin Committee Member	Date
//signed//	04 September 2011
Dr. Matthew C. Fickus Committee Member	Date

Accepted:

//signed//	04 September 2011
Marlin U. Thomas Dean, Graduate School of Engineering and Management	Date

Abstract

A new theory and algorithm for scatterer classification in synthetic aperture radar (SAR) imagery is presented. The automated classification process is operationally efficient compared to existing image segmentation methods requiring human supervision.

The algorithm reconstructs coarse resolution subimages from subdomains of the SAR phase history. It analyzes local peaks in the subimages to determine locations and geometric shapes of scatterers in the scene. Scatterer locations are indicated by the presence of a stable peak in all subimages for a given subaperture, while scatterer shapes are indicated by changes in pixel intensity. A new multi-peak model is developed from physical models of electromagnetic scattering to predict how pixel intensities behave for different scatterer shapes. The algorithm uses a least squares classifier to match observed pixel behavior to the model. Classification accuracy improves with increasing fractional bandwidth and is subject to the high-frequency and wide-aperture approximations of the multi-peak model.

For superior computational efficiency, an integrated fast SAR imaging technique is developed to combine the coarse resolution subimages into a final SAR image having fine resolution. Finally, classification results are overlaid on the SAR image so that analysts can deduce the significance of the scatterer shape information within the image context.

To my Lord and Savior, Jesus, who has shown me great mercy.

To my beautiful wife and wonderful children, who make life sweet.

To my father and mother, who taught me the importance of dedication and service.

Acknowledgements

This dissertation would not have been possible without the patient instruction and guidance of my advisor, Professor Mike Saville, to whom I am deeply indebted. His dedication to this research project produced great benefit for me and the readers of this document.

Additional thanks are due to my committee members who gave me guidance at critical points during my research. Professor Matt Fickus provided key advice on asymptotic analysis of the wide-angle approximation and on the calculation of weights to control window approximation error in frequency. Professor Rick Martin provided key advice on frequency parameter estimation and the relationship between likelihood ratio testing and the least squares classifier.

Some AFIT faculty members also provided key support to my research. Professor Pete Collins guided me to important publications related to my research and supported me with several computational resources necessary to conduct my research. Professor Julie Jackson also guided me to important publications related to my research and provided key advice on canonical scatterer models.

Finally, I want to acknowledge my classmate, Dan Hack, whom I came to rely on for collegial support and feedback. Dan also produced synthetic phase histories of canonical scatterers and a range-Doppler imaging algorithm all of which greatly aided me in my research.

Dane F. Fuller

Table of Contents

Page

Page

List of Figures

Figure Page

Figure Page

List of Tables

List of Abbreviations

Abbreviation		Page
SAR	synthetic aperture radar	1
SPLIT	spectrum parted linked image test	2
MF	matched filter	13
CBP	convolution backprojection	13
DTED	digital terrain elevation data	14
RMS	root mean squared	15
IFFT	inverse fast Fourier transform	19
SLICY	Sandia Laboratories implementation of cylinders	20
GO	geometric optics	20
GTD	Geometric Theory of Diffraction	20
RCS	radar cross section	22
DAP	dispersive, anisotropic, and polarimetric	39
IFT	inverse Fourier transform	71
PFA	polar format algorithm	77
ISAR	inverse SAR	91
CV	civilian vehicle	104
RVs	random variables	114
AWGN	additive white Gaussian noise	114
iid	independent and identically distributed	114
SNR	signal-to-noise ratio	115
SCR	signal-to-clutter ratio	116
SIR	signal-to-interference ratio	117

Abbreviation		Page
PSF	point spread function	142

PHASE HISTORY DECOMPOSITION FOR EFFICIENT SCATTERER CLASSIFICATION IN SAR IMAGERY

I. Introduction

This chapter provides an introduction and overview of the dissertation document. Section 1.1 is an executive summary of the research motivation, hypotheses, and findings. Section 1.2 highlights the operational needs which are addressed by this dissertation. Section 1.3 lists the conference papers, journal articles, and other deliverables which have been produced in connection with this dissertation. Section 1.4 wraps up with an outline of the document and the organization of its chapters.

1.1 Executive Summary

Resource management is an ongoing need in defense operations. As a result, synthetic aperture radar (SAR) imaging and classification algorithms are needed to rapidly queue human operators and precision algorithms to regions of high interest. This dissertation describes a new SAR imaging and classification theory as a foundation from which to build rapid queuing solutions for improved operational efficiency. The theory is demonstrated in a new algorithm based on efficient imaging and classification techniques.

Phase history decomposition is a highly efficient technique for SAR image reconstruction, where subimages are produced as an intermediate step of the imaging process. The subimages have coarser resolution than the final image, but have been shown to provide insight into the anisotropic and dispersive nature of objects in the image scene. While research on the anisotropic nature of scatterers in subimages

has been on-going for some time, research on the dispersive nature of scatterers in subimages is quite nascent and worthy of additional investigation. In response, this dissertation investigates the concept of scatterer classification by subimage analysis and develops a fundamental and holistic theory for this emerging research area. This research hypothesizes that

- it is possible to locate and classify canonical scatterers by observing the intensities of subimage pixels, and
- phase history decomposition makes this approach to classification highly efficient.

The key findings of this research effort include

1. image peaks due to a distributed canonical scatterer can be modeled with a simple equivalent canonical point scatterer [58],
2. the intensities of subimage peaks reveal the locations and types of canonical point scatterers in a SAR scene [57],
3. the classification and imaging errors associated with phase history decomposition are controllable [58, 59], and
4. the proposed approach is novel, efficient, and foundational [58, 59].

The first key finding results from development and study of a new scattering model called the multi-peak model. The second key finding results from a new scatterer classification algorithm called the spectrum parted linked image test (SPLIT). Imaging accuracy in the third key finding and computational efficiency in the fourth result from a new integrated algorithm that combines fast SAR imaging techniques with scatterer classification. The greatest benefit of the new theory is the operational efficiency derived by automatically displaying scatterer classification results within the

context of the SAR image. This is a significant improvement over existing scatterer classification methods [3, 30, 46, 47, 48, 62, 73] that require human supervision to ensure accurate classification.

1.2 Operational Needs

One of the ongoing needs in defense operations is resource management due to the fact that there exists more imagery collection capability than processing capability [13, 19, 32, 102, 115]. Therefore, SAR imaging algorithms are needed to provide rapid queuing of operators and precision algorithms to regions of high interest [63, 142]. In general, precision algorithms are not adequate in meeting this need because they are computationally inefficient, operationally inflexible, or both [54, 80, 119, 127].

For instance, precision SAR imaging algorithms improve SAR image quality by using better geometric approximations commonly made in the imaging algorithm [24, 36, 76]. However, increasing the order of these geometric approximations comes at an increased computational cost [24, 36]. Therefore, computational resource management is optimized when use of precision SAR imaging algorithms is limited to regions where increased precision is warranted.

Precision target recognition algorithms are notoriously sensitive to operational conditions, which cause them to be inflexible outside of a specific operational scenario [54, 80, 119, 127]. In this case, the precision algorithms must be used selectively and queued by experienced analysts based on operational parameters and image context. Unfortunately, this creates an operational bottleneck by demanding human resources be used to manage precision target recognition algorithms. This is, in effect, the exact opposite of what is needed to improve resource management in defense operations.

In order to provide rapid queuing of operational resources, it is acceptable for a SAR imaging and classification algorithm to sacrifice some precision in order to obtain

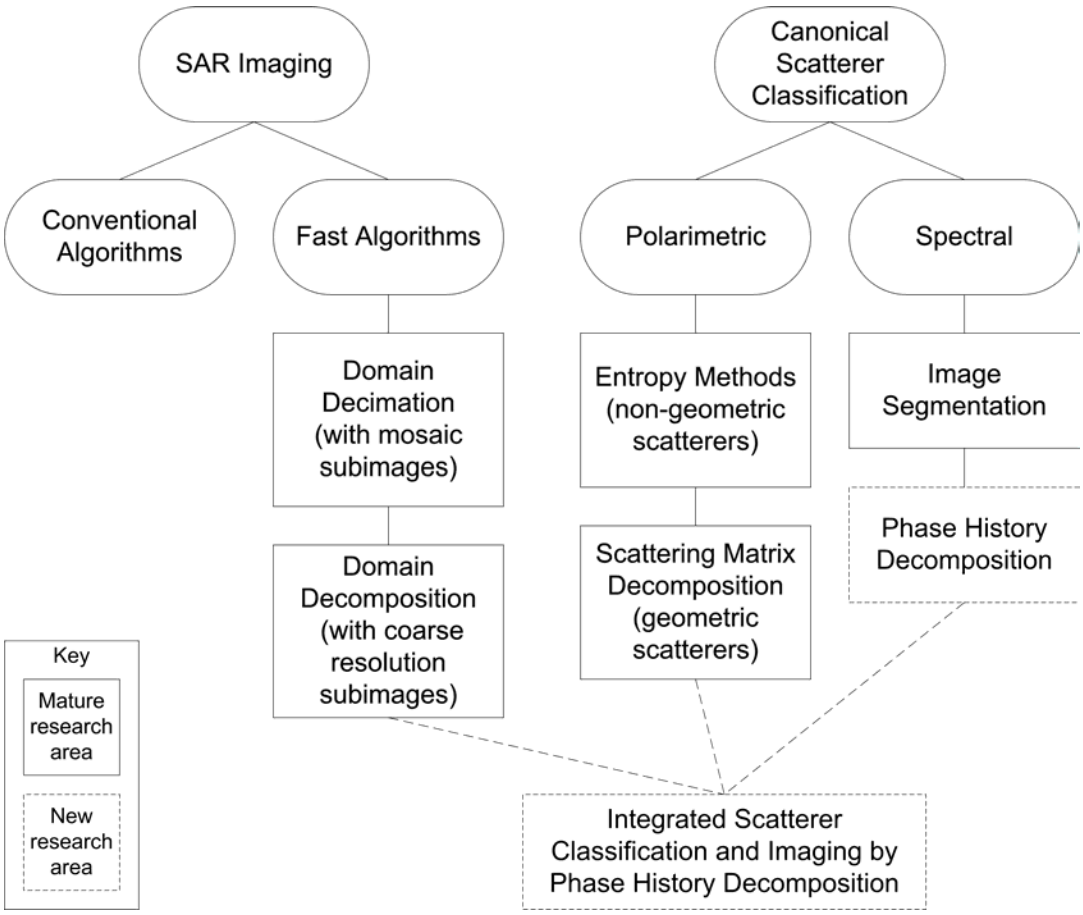

Figure 1. The dissertation research improves theoretical knowledge in two new areas.

efficiency and flexibility. In keeping with this principle, this dissertation describes a new SAR imaging and classification theory as a foundation from which to build rapid queuing solutions for improved operational efficiency.

1.3 Contributions

This dissertation research improves theoretical knowledge in two new areas, as shown in Figure 1. It develops new theory for Scatterer Classification by Phase History Decomposition and combines this with existing theories in Scattering Matrix Decomposition and Domain Decomposition Imaging. It also develops unique design

principles to address the particular difficulties associated with combining these into an integrated theory and algorithm.

The research presented in this dissertation resulted in three published conference papers and two journal article submissions [55, 56, 57, 58, 59]. In addition, a fast convolution backprojection and scatterer classification code was fully developed and will be provided to offices who sponsored elements of this work. It will also be considered for integration into the AFIT LORE Processing INtegrated Environment (ALPINE). From this code, alternate versions of the polar format algorithm, range Doppler algorithm, and omega-k algorithm were also developed for experimental purposes.

Last, this dissertation produces a theoretical foundation for follow-on research in the following areas:

- discontinuous phase histories,
- improved parameter estimation using advanced detection and estimation theory,
- extension to bi-static and 3D SAR,
- blended domain decomposition and decimation techniques, and
- additional uses for the multi-peak model and SPLIT algorithm.

These are described in more detail in Subsection 7.2 of the Conclusion.

1.4 Organization

The dissertation is organized as follows. Chapter II presents a survey of the mature research areas in Figure 1. Using a combination of tutorial and literature review, it presents theory and trends in the topics of SAR imaging, domain decomposition, canonical scattering models, and scatterer classification. Chapter III presents the research objective in general terms. It serves as a transition between the background

section and the more detailed theoretical developments and research findings contained in the remaining sections. Chapter IV develops the new multi-peak model for canonical scatterers. It describes how, under a wide-angle condition, the imaging process integrates out the azimuth dependency of distributed canonical scatterers. In this way, image peaks due to a distributed canonical scatterer can be modeled as due to an equivalent canonical point scatterer. Chapter V develops the SPLIT algorithm, which uses subimage pixel intensities to estimate the locations of canonical scatterers as well as their frequency dependencies. SPLIT classifies the observed canonical scatterers using the multi-point model to deduce the likelihood that a certain type of scatterer is present. Chapter VI develops the integrated algorithm which combines SPLIT-based classification with domain decomposition imaging. The integrated algorithm is shown to be efficient in that it provides scatterer classification information without increasing the computational complexity of SAR imaging algorithms. The combined results provide more information about the scene than a SAR image can provide alone. Chapter VII concludes with an overview of the key findings and contributions in this dissertation, a summary of the advantages and limitations of the algorithm, and suggestions for follow-on research.

II. Background

This chapter provides the background needed to understand the theory and trends in areas related to this research. It serves as a tutorial and includes reviews of the seminal and current literature, where appropriate, along with observations of trends. Section 2.1 begins with an overview of basic SAR imaging concepts. It builds on these basic concepts to present the more advanced concepts of phase history decomposition imaging and the sum of scattering centers model. Section 2.2 presents the set of canonical scatterers used to obtain a parsimonious sum of scattering centers. It explains how the amplitude and polarization responses of canonical scatterers are derived from physical models of electromagnetic scattering. Section 2.3 gives an overview of some basic principles of feature extraction and classification, to include the least squares classifier featured in this dissertation. It concludes with an example of least squares classification using the polarimetric model parameters for canonical scatterers.

2.1 SAR Phase History

SAR images are typically reconstructed from a SAR phase history, which represents the SAR signal in the spectral domain. This section presents how the SAR phase history is originated. Then it presents principles of SAR imaging, including domain decomposition imaging. Finally, it presents how the phase history can be modeled as a sum of phase histories due to multiple scattering centers.

2.1.1 Origination.

Monostatic SAR systems measure the electromagnetic reflectivity of objects in the radar field of view and rely on subsequent signal processing to reconstruct an

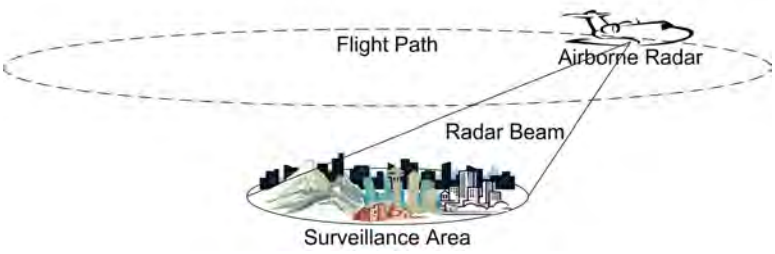

Figure 2. Notional airborne SAR system.

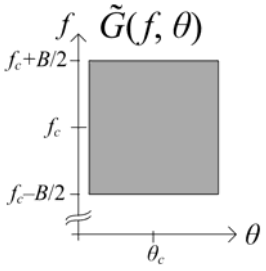

Figure 3. Notional phase history domain.

estimate of the reflectivity. The estimate is presented as a SAR image recovered from quadrature-demodulated samples of the backscattered electric field received at discrete and different frequencies and aspect angles along the synthetic aperture [24, 36, 37, 76, 133]. These discrete samples are collectively referred to as the SAR phase history. The term 'phase history' refers to the phase differences corresponding to the relative locations of each scatterer in the scene.

A notional airborne SAR system is depicted in Figure 2 where discrete samples of the scattered electric field are collected over the flight path. The phase history is typically displayed as a manifold at sample coordinates in the spectral domain [24, 76]. For example, a notional SAR phase history domain, which states $\tilde{G}$ is a function of (f, θ), is depicted in Figure 3, where the $\tilde{}$ symbol denotes that the phase history is a complex-valued function. The discrete samples are contained in the domain $\mathbf{\Omega} = [\mathbf{f}, \boldsymbol{\theta}]$, where $\mathbf{f}$ is a vector of sample points in frequency and $\boldsymbol{\theta}$ is

a vector of sample points in azimuth. For convenience, the individual phase history samples are not shown. This allows drawings of the SAR phase history to be readily differentiated from drawings of SAR imagery which explicitly show individual pixels. This convention is used throughout the dissertation.

The sample frequencies are determined by the transmitted electromagnetic field, usually produced with a linear frequency modulated (LFM) signal [24, 76]. For multiple polarization channels, a separate phase history is produced for each channel. A particularly important aspect of the SAR phase history is that it has frequency and azimuth diversity, and in the case of polarimetric SAR, it has polarimetric diversity as well. The remaining discussion assumes that the sampling rate is sufficient to prevent aliasing in the image and that all amplitude variations due to antenna gain pattern and spherical wave propagation are normalized between samples.

2.1.2 SAR Imaging.

The image, $\tilde{g}$, is reconstructed using an appropriate transformation from the spectral domain to the spatial domain. Recall that the phase history, $\tilde{G}$, is defined over finite regions of support, where f_c is the center frequency of the phase history with bandwidth B, and θ_c is the center angle of the phase history with aperture width Θ. In this case, the finite regions of support can be represented by a band-limited filter or window in frequency, $H_B(f - f_c)$, and an aperture-limited filter or window in azimuth, $H_\Theta(\theta - \theta_c)$, where the windows have region of support $H_B(f) \in [-B/2, B/2]$ and $H_\Theta(\theta) \in [-\Theta/2, \Theta/2]$, respectively. Hence, the 2D image is reconstructed from the windowed phase history as

$$\tilde{g}(x, y) = \mathcal{B}\left\{H_B(f - f_c)H_\Theta(\theta - \theta_c)\tilde{G}(f, \theta)\right\}, \tag{1}$$

where (x, y) are image coordinates and $\mathcal{B}\{\cdot\}$ is a Fourier-based imaging operator that maps from (f, θ) to (x, y). The choice of H_B and H_Θ depends on the need for image resolution versus image contrast. For convenience, the $\tilde{g}$ dependence on H_B and H_Θ is suppressed in the notation. Although the phase history and image are digitally sampled and processed in practice, the variables f, θ, x, and y are expressed as continuous for ease of notation. Note that if multiple polarization channels are available, the transformation is performed for each channel's phase history, resulting in a set of usually two to four polarization diverse images.

2.1.2.1 Subimages.

The relationship between spectral bandwidth in the phase history and spatial resolution in the SAR image is a manifestation of the Gabor limit [60]. In short, the spatial resolution is inversely proportional to the spectral bandwidth. Therefore, it is possible to produce coarse resolution subimages from subdomains of the phase history. An example of this is illustrated in Figure 4 where Figure 4(b) shows a coarse resolution subimage. In this case, the subwindows, $H_{B'}$ and $H_{\Theta'}$, decompose the spectral domain, where the regions of support for these subwindows, $B' < B$ and $\Theta' < \Theta$, are called subbands and subapertures, respectively. Multiple subdomains may be created by simply shifting the subwindows to a discrete number of center frequencies. In this case, center frequencies are annotated by subscripts i and j, and the short hand notations $H_{B'i} = H_{B'}(f - f_{ci})$ and $H_{\Theta'j} = H_{\Theta'j}(\theta - \theta_{cj})$ are used throughout the dissertation, where convenient. Thus, the reconstructed subimages are annotated accordingly as

$$\tilde{g}_{ij}(x, y) = \mathcal{B}\left\{H_{B'i} H_{\Theta'j} \tilde{G}(f, \theta)\right\}. \tag{2}$$

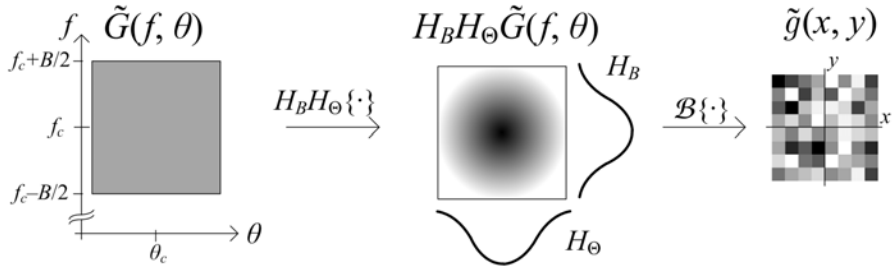

(a) A fine resolution SAR image is reconstructed from the full domain of the phase history.

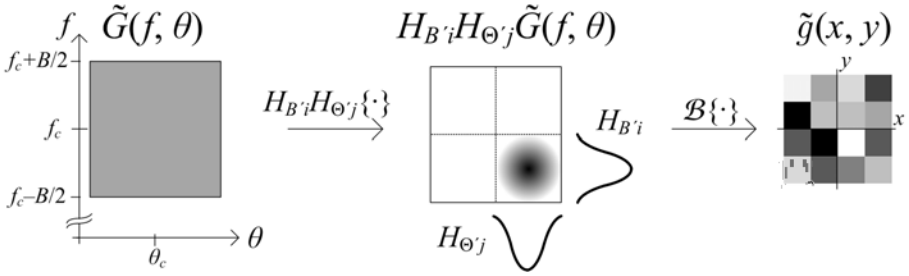

(b) A coarse resolution SAR subimage is reconstructed from a subdomain of the phase history.

Figure 4. Phase history decomposition produces multiple coarse resolution subimages.

When appropriate, the subscript, p, can be added to $\tilde{g}_{ij}$ and $\tilde{G}$ to denote subimages produced from phase histories obtained from different polarization channels.

2.1.2.2 Phase History Decomposition.

The phase history can be replicated by using a series of subwindows designed and weighted so that their summation approximates the desired fullband and full aperture windows. The summations are expressed as $H_B \approx \sum_i c_i H_{B'}(f - f_{ci})$ and $H_\Theta \approx \sum_j c_j H_{\Theta'}(\theta - \theta_{cj})$, where c_i and c_j are the weights. The shorthand notations $H_\Theta = H_\Theta(\theta - \theta_c)$ and $H_B = H_B(f - f_c)$ are used here and throughout the dissertation, as appropriate. In this case, the resulting coarse resolution subimages can be interpolated to a finer resolution and summed, where the result approximates the fine resolution image conventionally reconstructed from the full domain of the phase his-

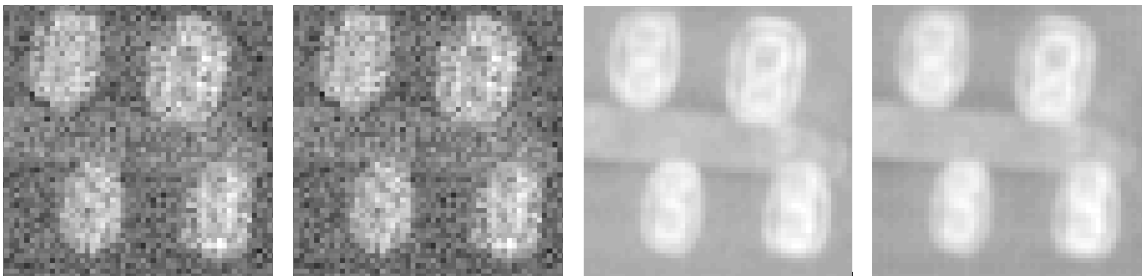

(a) subaperture imaging.

(b) domain decomposition imaging.

(c) subaperture imaging with multilook.

(d) domain decomposition imaging with multilook.

Figure 5. Examples of domain decomposition imagery of four automobiles in a parking lot taken from the Gotcha public release data set.

tory [12]. This assumes a linear imaging operator, as is common [76], and is expressed as

$$\widehat{\tilde{g}} = \sum_j c_j \sum_i c_i \mathcal{I}\left\{\tilde{g}_{ij}\right\}. \tag{3}$$

where $\mathcal{I}\{\cdot\}$ is the interpolation operator and the $\widehat{\ }$ symbol indicates that the result is an approximation to the full domain image in Equation (1). This process is called domain decomposition imaging, where typical implementations have a controllable error in the approximation [12]. Examples of conventional imaging and domain decomposition imaging using cubic interpolation are shown in Figures 5(a) and 5(b), respectively. In this case, error in the approximation is sufficiently controlled so that the images are visually indistinguishable. The scene consists of four automobiles in a parking lot taken from the Gotcha public release data set [25].

Domain decomposition imaging is traditionally motivated by the desire to reduce the computational complexity of certain imaging algorithms by accepting a controllable error in imaging accuracy [12]. Efficiency is attained by an iterative, multi-level decomposition and aggregation of subimages. The overall computational complexity of multi-level domain decomposition algorithms is $O(N^2 \log N)$, for an $N \times N$ image [12]. Domain decomposition can be implemented with any of the conventional SAR

Table 1. Computational Complexity of Conventional SAR Imaging Algorithms [24, 36, 76].

Mode	Algorithm	Complexity
spotlight	Matched Filter	$O(N^4)$
	Convolution Backprojection	$O(N^3)$
	Polar Reformating	$O(N^2 \log N)$
stripmap	Range Doppler	$O(N^2 \log N)$
	Chirp Scaling	$O(N^2 \log N)$
	Omega-K	$O(N^2 \log N)$

imaging algorithms listed in Table 1. However, the benefit of a reduced order of computational complexity will only be realized for the matched filter and convolution backprojection algorithms.

2.1.2.3 *Observations.*

SAR imaging is a mature area of research with many textbooks dedicated to the various methods and their applications. While the matched filter (MF) algorithm provides the most flexibility and best image quality of the algorithms, its computational complexity of $O(N^4)$ is exceptionally high compared to other methods. The other algorithms obtain computational efficiency by use of batch processes with geometric approximations which limit imaging accuracy and flexibility. However, these limitations can be managed so that they are insignificant for most SAR applications. The algorithms with computational complexity of $O(N^2 \log N)$ obtain computational efficiency through 2D Fourier transforms of rectangular formatted phase history data. In contrast, the convolution backprojection (CBP) algorithm uses the projection slice theorem with polar formatted phase histories, resulting in a computational complexity of $O(N^3)$ with higher order [40]. Because of this, CBP is usually employed only when its superior flexibility in choosing the locations of image pixels is needed. An example situation where such flexibility is desired is the case of 2D imaging of the surface of the earth over very wide-angle or full 360° apertures. In this case, the CBP

algorithm allows for image pixel locations to be selected to match the digital terrain elevation data (DTED) of the scene for superior image quality.

The fast SAR imaging techniques ensure a computational complexity at or near $O(N \log N)$ with a controllable amount of image artifacts introduced into the final image. In general, the fast SAR imaging techniques only provide a computational advantage for the CBP and MF imaging algorithms, but they are not limited to these. There are two primary techniques for fast SAR imaging: domain decomposition and domain decimation. Domain decomposition imaging produces coarse resolution subimages with diversity in frequency, azimuth, and polarization, which can be exploited for scatterer classification. As such, a single level version of the multilevel domain decomposition technique in Reference [12] is used throughout this dissertation. Alternately, domain decimation produces full resolution subimages of limited extent that are diverse in location. The final image is reassembled from these subimages by a process resembling a mosaic. Because the pixel locations of the full resolution subimages can be adjusted with precision, domain decimation is the preferred method for applications where the image pixels are matched to DTED, such as with the Gotcha radar.

It is conceivable to combine the decimation and decomposition techniques, although this has not been reported in the literature. In this way, multilevel domain decimation could be used to form the coarse resolution subimages matching DTED. Then, the coarse resolution subimages can be used for scatterer classification and subsequent single-level domain decomposition can be used to form the final image.

2.1.2.4 Subaperture Imaging.

Subaperture imaging is a decomposition of the phase history in azimuth only and can be used with any of the conventional imaging algorithms. Its use is typi-

cally motivated by the need to limit azimuth resolution, reduce speckle, or both. In practice, SAR systems are often less restricted in angular bandwidth than frequency bandwidth. This relationship is particularly true for airborne circular SAR systems, like the one in Figure 2 of Section 2.1.1 which can orbit a given scene and produce a phase history sampled over a full 360° in azimuth. In this case, subapertures of the data are processed in turn. For surveillance applications, a series of subimages is often viewed in sequence to simulate frames of streaming video, called video SAR [18, 109]. In addition, when the subimages are registered to a common grid, they can be coherently summed to produce a full aperture image expressed as

$$\widehat{\tilde{g}}(x,y) = \sum_j c_j \mathcal{B}\left\{H_B H_{\Theta' j} G(f,\theta)]\right\} = \sum_j c_j \tilde{g}_j(x,y). \tag{4}$$

Figure 5(a) is an example of subaperture imaging. Here, multiple subimages are reconstructed from successive 2° subapertures and are summed to approximate a full 360° aperture SAR image.

The grainy look in Figures 5(a) and 5(b) is attributed to a common SAR imaging effect called speckle. Speckle in SAR imagery results from a combination of having multiple scatterers and only finite processing resolution. The phase histories of the unresolved scatterers produce a random sum with characteristic appearance in the SAR image, although not appearing in photographs of the same scene. In fact, speckle has been shown to be well-modeled by a random phase process [113]. By taking the root mean squared (RMS) of pixel values over multiple subaperture images, areas with highly random pixel intensities become smoother and the effects of speckle are reduced. This is also called multilook imaging and is expressed as [36]

$$\bar{g}(x,y) = \sqrt{\sum_j c_j \left|\tilde{g}_j(x,y)\right|^2}. \tag{5}$$

An example of multilook imaging is shown in Figure 5(c) using the same data and subapertures as in Figure 5(a). Speckle-reduced SAR imagery is often preferred because it can be easier to interpret and exploit, even for the case when the subaperture images have coarser resolution than the full aperture image [116]. Multilook can be combined with domain decomposition imaging as

$$\widehat{\tilde{g}}(x,y) = \sqrt{\sum_j c_j \left| \sum_i c_i \mathcal{I}\{\tilde{g}_{ij}\} \right|^2}, \tag{6}$$

where the $\widehat{\ }$ symbol indicates that the result is an approximation to the multilook image in Equation (5). An example of multilook domain decomposition imaging using cubic interpolation is given in Figure 5(d). In this case, error in the approximation is sufficiently controlled so that the multilook images in Figures 5(c) and 5(d) are visually similar. Note that the imaging process is repeated for each polarization channel separately. The resulting set of polarization diverse images can be non-coherently summed, if desired.

2.1.2.5 *Observations.*

With the recent availability of very-wide angle SAR systems, interest has increased in exploiting the benefits of these systems. As a result, many different methods and techniques for combining subimages have been proposed. However, even though other non-coherent summations of subaperture images have been discussed in the literature [110], the domain decomposition Equations (3) and (6) are commonly used in practice, and are exclusively used throughout this dissertation.

Figure 6. Vector from the antenna phase center to the qth scattering center.

2.1.3 Sum of Scattering Centers Model.

By linear superposition, a SAR phase history can be modeled as a sum of phase histories due to Q scattering centers expressed as [138]

$$\tilde{G}(f,\theta) = \sum_{q=0}^{Q-1} \tilde{S}_q(f,\theta) e^{-j2k|\mathbf{r}_q|}, \tag{7}$$

where $\tilde{S}_q(f,\theta)$ is the amplitude function, $k = 2\pi f/c$ is the wavenumber having speed of light, c, and $\mathbf{r}_q$ is a vector from the antenna phase center to the qth scattering center, as shown in Figure 6.

A linear imaging operator is commonly used in practice, and in this case, the SAR image can be modeled as a linear superposition of images due to Q scattering centers expressed as

$$\tilde{g}(x,y) = \sum_{q=0}^{Q-1} \tilde{s}_q(x,y), \tag{8}$$

where

$$\tilde{s}_q(x,y) = \mathcal{B}\left\{ H_B H_\Theta \tilde{S}_q(f,\theta) e^{-j2k|\mathbf{r}_q|} \right\} \tag{9}$$

is the resultant of the imaging operator acting on the qth windowed phase history in Equation (7).

Consider a scene consisting of a single scattering center. In this case, the phase history samples contain amplitude and phase differences corresponding to the amplitude function and location of the scatterer. If for every sample, one knows the distance from the SAR system to a reference point in the scene (usually the scene center), then one can infer the location of the scatterer with respect to the reference. Furthermore, by applying an appropriate phase shift, the samples will integrate coherently.

The exact locations of point scatterers are usually not known *a priori*. Therefore, the imaging operator integrates over a grid of locations, each corresponding to a unique phase shift. This grid determines the pixel locations of the SAR image, and in the 2D case, is called the imaging plane. The accuracy of the coherent integration, and thus the accuracy of the image, is limited to time-invariance of the scatterers, field geometry, and SAR system [76].

Typically the imaging operator assumes a scene comprised of ideal point scatterers. In this case, $\tilde{S}_q$ is set to a real constant, and $\tilde{s}_q$ is called the point spread function. Therefore, a conventional 2D SAR imaging operator is [76]

$$\mathcal{B}\{\cdot\} = \frac{1}{2\pi}\int_{-\infty}^{\infty}\int_{-\pi}^{\pi}\{\cdot\}e^{j2k|\mathbf{r}|}|f|d\theta df, \tag{10}$$

where $\mathbf{r}$ is a vector from the radar phase center to the spatial coordinates in a chosen imaging plane at any azimuth angle. Because most of the energy in a SAR scene is well-modeled by ideal point scatterers, imaging operators which assume an ideal point scatterer, such as Equation (10), are common and used exclusively throughout this dissertation.

Note that for 2D imaging, a scatterer does not need to physically lie in the imaging plane in order to integrate coherently. Coherent integration occurs when $|\mathbf{r}_q|$ of the scatterer equals $|\mathbf{r}|$ of the imaging operator. Thus, scatterers with height, z_q, per-

pendicular to the 2D imaging plane are modeled as appearing at off-set coordinates determined by a projection along the spherical wavefront into the imaging plane. This is effect is referred to as SAR layover [76]. As a result, $|\mathbf{r}_q|$ can be modeled as a function of x_q, y_q, and θ, where (x_q, y_q) are the offset coordinates due to layover effect, if any. As such, the shorthand notation

$$\tilde{S}_q(f,\theta)e^{-j2k|\mathbf{r}_q|} = \tilde{S}_q(f,\theta;x_q,y_q) \tag{11}$$

will be used throughout this dissertation.

2.1.3.1 *Observations.*

It has been observed that certain objects in a scene may exhibit non-ideal scattering behavior with amplitude functions that are anisotropic, dispersive, or both. In addition, moving objects have coordinates, (x_q, y_q), that vary with time. As a result of their non-ideal behavior, such objects may appear unfocused or displaced in the SAR image reconstructed from Equation (10). The insertion of additional filters into the imaging operator can cause an anisotropic, dispersive, or moving object to simulate ideal scattering behavior and become better focused in a SAR image, and adaptive filters, such as those used in multiple signal classification (MUSIC), can enhance the detection and of a pre-determined type of scatterer [39, 66, 70, 94, 126, 130, 145]. However, such filters have the negative consequence of defocusing other scatterers of interest, especially if the filters are non-adaptive.

The imaging algorithms with a computational complexity of $O(N^2 \log N)$ use an inverse fast Fourier transform (IFFT) in two dimensions, where the computational complexity of a single IFFT is $O(N \log N)$. Unfortunately, an FFT for polar coordinates is not known. Therefore, these algorithms transform the SAR phase history and imaging algorithm into a rectangular format before using the IFFT. This transfor-

mation and its associated approximations produce many of the limitations associated with the faster imaging algorithms. Therefore, the characterization and mitigation of these limitations comprise much of the literature on SAR imaging.

This dissertation assumes the data and imaging operator are in polar coordinates, as in Equations (7) and (10), throughout its development. However, the theory and algorithm are not limited to polar coordinates, and considerations for rectangular formatted data and imaging operators are discussed, where appropriate.

2.2 Physical Model of Canonical Scatterers

Unfortunately, the number of ideal point scatterers required to accurately model or simulate a SAR phase history is typically quite large, particularly for wide band or wide apertures data. A parsimonious sum is possible when the scattering centers are modeled as canonical scatterers [62]. Geometric objects in the scene, called canonical scatterers, have a predictable response to changes in frequency, azimuth, and polarimetry [83]. Examples of canonical scatterers include trihedrals, dihedrals, plates, cylinders, and spheres. Canonical scatterers are of interest because they are commonly associated with man-made objects [14, 106, 108, 149]. For example, the Sandia Laboratories implementation of cylinders (SLICY) is comprised of canonical scatterers as shown in Figure 7. Here, the cylinders are considered a special case of the general cone shape.

It is desirable to detect and classify canonical scatterers in SAR imagery using well-known, physical models of electromagnetic scattering [29, 122]. It has been shown that the amplitude functions for canonical scatterers are parameterized by physical models based on geometric optics (GO) and the Geometric Theory of Diffraction (GTD) [78]. A restricted set of possible geometrical shapes, combined with the high-frequency, far-field assumptions in GO/GTD, produce a model with only a few parameters.

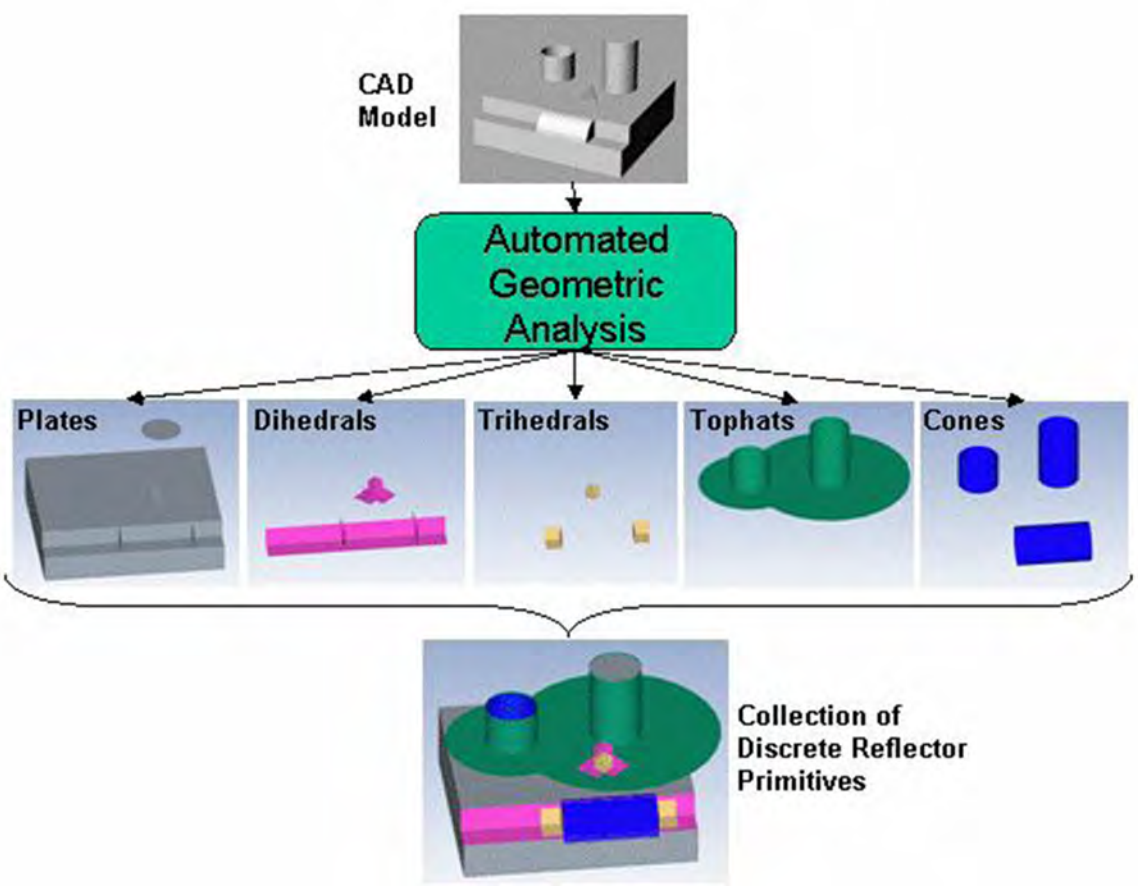

Figure 7. The SLICY can be modeled as a collection of canonical scatterers [149]. Note that a cylinder can be represented as a special case of a cone.

The model can be used to simulate a SAR phase history, or the parameters can be estimated from SAR data to detect or classify canonical scatterers in the scene.

In order to develop a canonical scatterer classification algorithm in the spatial domain, subimages are modeled as a sum of subimages due to Q canonical scatterers. This idea is developed in detail later in Chapter III. Meanwhile, the following subsections present the background needed to understand how the amplitude functions of canonical scatterers vary with changes in frequency and azimuth. They also present how the intensity of canonical scatterers responds to changes in polarimetry.

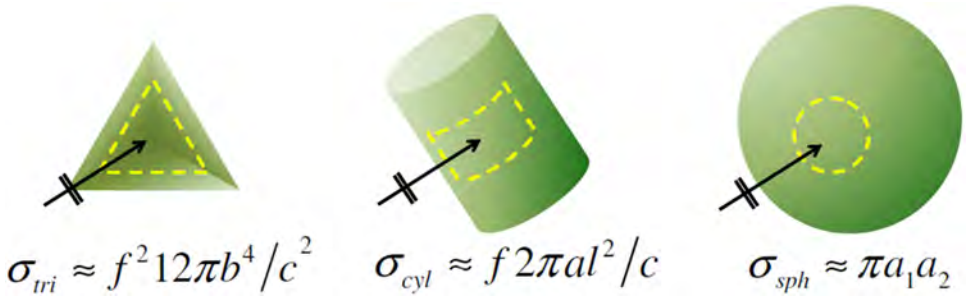

Figure 8. Canonical scatterer radar cross sections have a frequency dependency that depends upon the local curvature of the scatterer [83].

2.2.1 Amplitude Response in Frequency.

For a co-polarized channel, the amplitude response of the electric field backscattered from a canonical scatterer has a frequency response predicted by GO/GTD as [62, 78]

$$\tilde{S}_f(f; A, \alpha) = A(jf)^{\alpha/2}, \tag{12}$$

where A is a complex-valued amplitude related to the physical size of the canonical scatterer, f is the frequency of the incident electromagnetic field, and α is an integer value depending upon the local curvature of the canonical scatterer's shape. Note that this model assumes the canonical scatterers are perfect electrical conductors.

Figure 8 illustrates how frequency dependency of the radar cross section (RCS) for canonical scatterers depends upon the scatterer's local curvature. In this case, the RCS is the magnitude squared of the amplitude function given by $\sigma = |\tilde{S}_f|^2 \propto f^\alpha$. The trihedral, having no curvature, features a quadratic response (f^2); the cylinder, having curvature in one dimension, features a linear response (f^1); and the sphere, having curvature in two-dimensions, features a flat response (f^0). The values of α for common shapes are well known and listed in Table 2. Note that there is an ambiguity when discriminating between canonical scatterers by α only. For instance, plates, trihedrals, and dihedrals all have the frequency parameter, $\alpha = 2$.

Table 2. Traditional Frequency Response Parameter for Ideal Canonical Scattering Geometries [83].

Scattering geometry	α
plate, trihedral, dihedral	2
cylinder/cone, top hat	1
sphere, straight edge/wire	0

Note that diffraction from curved edges and tips of objects produce scattering with inverse frequency response of $\alpha = -1$ and $\alpha = -2$, respectively [62, 84, 121]. However, these have such a low RCS as to not be prevalent in SAR imagery. As a result, curved edge and tip scattering mechanisms are ignored throughout this dissertation, except in Section 5.4.2.

2.2.1.1 *Observations.*

The GO/GTD-based scattering models are limited by a high-frequency approximation. However, these models are preferred because backscattering which occurs at lower frequencies has less directivity, which lowers the received energy of the desired signal. For wavelengths greater than the object extent, the frequency response is governed by Rayleigh scattering [83]. In this case, there is little variation of the incident field across the object, and the incident field can be modeled as being quasi-static [83]. Under these conditions, relative intensities of scatterers can be determined, but the amplitude response is independent of object shape [83]. Because shape cannot be determined, no models exist for describing canonical scatterers when the wavelength of the incident field is greater than the extent of the canonical scatterer.

Alternately, when wavelengths approach the order of the object size, it has been shown that an object's size is related to its late-time resonance response [27, 79]. In this case, physical mechanisms cause EM energy to stay attached to the surface of an object in what are called surface waves [83]. Surface wave scattering produces a strong

early-time signal that is independent of object size [83]. However, it has been shown that the much weaker late-time signal will resonate in accordance with object size [79]. Models describing this late-time resonance response have been successfully used to classify objects, but only in ideal scenarios where noise, clutter, and interference are constrained.

In general, the performance of late-time resonance approaches to scatterer classification is limited because of the low energy of the late-time response. Thus, in practice, accurate feature extraction requires a prohibitively high signal-to-noise ratio. Matched filter techniques, such as those found in singularity expansion method [9], have been shown to reduce noise sensitivity, but at the expense of requiring *a priori* knowledge of the target. Despite these limitations, interest in late-time resonance response models continues, as evidenced by recent publications [61, 105]. Nevertheless, limiting factors restrict the usefulness of resonance response models in distinguishing canonical scatterers.

2.2.2 Amplitude Response in Azimuth.

At a single azimuth angle or over an extremely narrow aperture, the amplitude responses for all canonical scatterers are well modeled by Equation (12) [121]. However, for typical SAR apertures, the amplitude response of the backscattered field for distributed scatterers has an azimuth dependency dominated by a sinc-like pattern. This response is in relation to the slant plane containing the synthetic aperture. Common distributed scatterers include flat plates at broadside aspect, dihedrals with fold-lines parallel to the slant plane, cylinders with axes of rotation parallel to the slant plane, and edges or wires lying parallel to the slant plane. Of these, the dihedral, in particular, is often present in SAR imagery of man-made structures. For example, the side of a building and the ground form a dihedral with a fold-line often

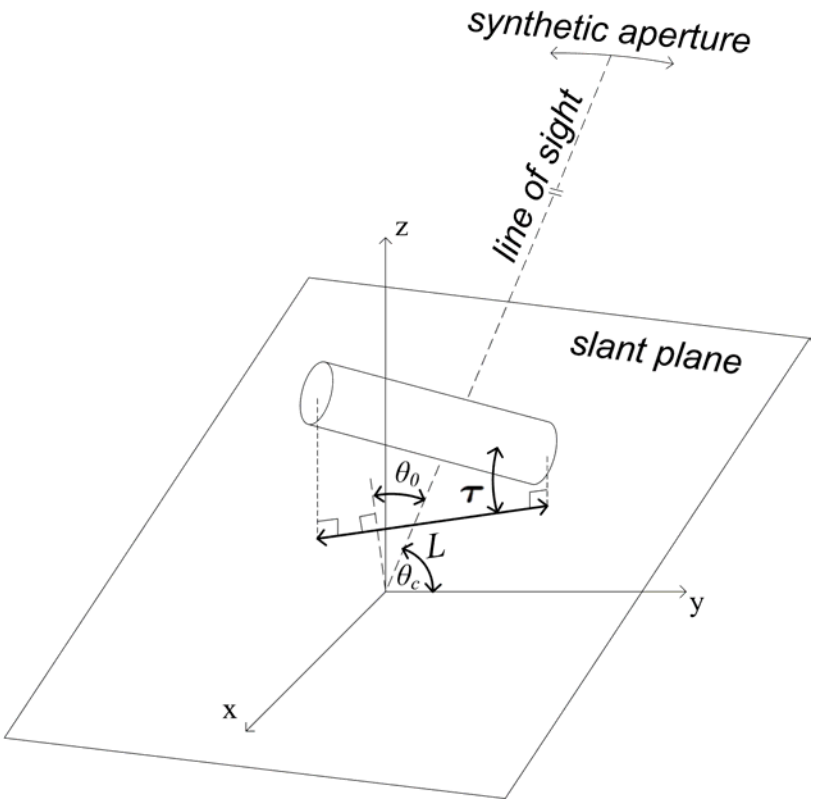

Figure 9. Example model parameters for a cylinder with axis of rotation projected into the slant plane.

lying parallel to the slant plane. The amplitude response as a function of azimuth is well-modeled by [6, 62]

$$S_\theta(f, \theta; L, \theta_0) = \text{sinc}\left[\tfrac{2}{c} f L \sin(\theta - \theta_0)\right], \tag{13}$$

where the sinc function is defined as $\text{sinc}(t) = \frac{\sin(\pi t)}{\pi t}$, L is the effective length of the scatterer as projected onto the slant plane, and θ_0 is the orientation angle normal to this projection and referenced to the center angle of the aperture, θ_c [62]. The dependence upon θ_c is suppressed in the notation because the simplification $\theta_c = 0$ can often be made without loss of generality. An example of the effective length and orientation angle for a cylinder is illustrated in Figure 9.

It has been shown that most scatterers have an angular persistence of less than twenty degrees [43]. Furthermore, for flat plates, there is an extra $\cos(\theta)$ factor in the azimuth response of Equation (13) [6]. For these reasons, it is prudent to place a restriction of $\Theta < 20^\circ$ on the aperture width for which Equation (13) is valid. However, in practice any aperture greater than 20° will likely be decomposed into narrower subapertures before imaging; so this restriction is deemphasized throughout the dissertation.

2.2.2.1 *Observations.*

For very narrow angle imaging, scatterer anisotropy is generally negligible because large variations in target aspect are not expected [125]. However, anisotropy should be accounted for any time large variations in aspect are encountered, such as for wide-angle SAR applications [134]. These include strip-map data collected from air and spaceborne radar platforms operating at P- or L-band [51], data collected from RCS measurement facilities where targets are placed on turn-tables, and circular SAR data collected from airborne radar platforms [110]. Much of the early research in target anisotropy was motivated by radar imaging at low-frequencies for foliage and ground penetration. The use of low-frequencies drove this early research to examine the late-time resonance response of targets [8, 85].

Before the mid-1990s, such wide-angle SAR data collections were not common. However, recent technological advances have enabled the collection of coherent data over very wide apertures [110]. These developments have spurred interest over the last decade in studying methods and models that predict and leverage the anisotropic behavior of scatterers. A review of the current literature reveals that directional filters are the most common approach to leveraging anisotropic behavior for target detection and discrimination [1, 47, 130, 136]. Directional filters denote subaperture techniques

where the subaperture filter is often chosen according to expected target anisotropy. When ultra-wide band data is available, the directional filters are often extended to 2D filtering to account for both anisotropic and dispersive analysis. In addition to filters, the parametric model in Equation (13) [31, 50, 74] and a sparse dictionary method [144] have also been proposed to characterize and identify anisotropic scattering.

2.2.3 Intensity Response in Polarization.

This subsection presents the theoretical background needed to understand how the intensities of canonical scatterers are polarization dependent. Specifically, it presents Krogager decomposition of the scattering matrix as a way to differentiate between odd-bounce and even-bounce scattering mechanisms. The proportions of odd-bounce and even-bounce scattering energy are very useful in determining the geometric shape of canonical scatterers.

2.2.3.1 The Scattering Matrix.

The scattering matrix can be used to specify polarimetric properties of electromagnetic scattering. That is, the polarization pairs of the scattered field are determined via matrix multiplication of the scattering matrix with the polarization pairs of the incident field [112]

$$\mathbf{E^s} = \begin{bmatrix} E_x^s \\ E_y^s \end{bmatrix} = \frac{1}{\sqrt{4\pi r}} \mathbf{A} \mathbf{E^i} e^{-jkr} = \frac{1}{\sqrt{4\pi r}} \begin{bmatrix} A_{xx} & A_{xy} \\ A_{yx} & A_{yy} \end{bmatrix} \begin{bmatrix} E_x^i \\ E_y^i \end{bmatrix} e^{-jkr}, \tag{14}$$

where the elements of the scattering matrix are complex, $A_{ij} \in \mathbb{C}$, and r is the distance between the receive antenna and the reference plane at the scatterer. The polarization pairs can be expressed in either linear or circular polarizations. This choice is often dictated by the antenna design of the radar system. Standard coordinate system

conventions for linear polarization pairs use $x = H$ for horizontal polarization and $y = V$ for vertical polarization [112]. While, similar conventions for circular polarization pairs use $x = L$ for left circular and $y = R$ for right circular [112].

The definition of the scattering matrix is not unique because the existence of many equivalent coordinate systems introduces an ambiguity. However, two particular coordinate systems and resulting scattering matrix definitions are commonly used. The Jones matrix is popular because it presents a right-handed system with regard to the conventional definition of wave propagation [112]. In contrast, the Sinclair matrix, $\mathbf{S}$, presents a left-handed system. A left-handed system would not normally be desirable, but the Sinclair matrix has the distinct advantage that $S_{xy} = S_{yx}$ for the case of monostatic backscattering. The dissertation is limited to the case of monostatic backscattering only; therefore, the Sinclair scattering matrix given by

$$\mathbf{S} = \begin{bmatrix} S_{xx} & S_{xy} \\ S_{yx} & S_{yy} \end{bmatrix} \tag{15}$$

will be used exclusively throughout the remaining discussion. In this case, the transformation from the linear polarization basis to the circular polarization basis is given by [88]

$$\begin{aligned} S_{RR} &= jS_{HV} + \tfrac{1}{2}(S_{HH} - S_{VV}) \\ S_{LL} &= jS_{HV} - \tfrac{1}{2}(S_{HH} - S_{VV}) \\ S_{RL} &= \tfrac{1}{2}(S_{HH} + S_{VV}), \end{aligned} \tag{16}$$

where $S_{LR} = S_{RL}$ for monostatic radar systems.

2.2.3.2 Krogager Decomposition of the Sinclair Scattering Matrix.

Several decompositions of the Sinclair scattering matrix have been proposed for canonical scatterer analysis. The most common being Pauli [33], Krogager [87], and

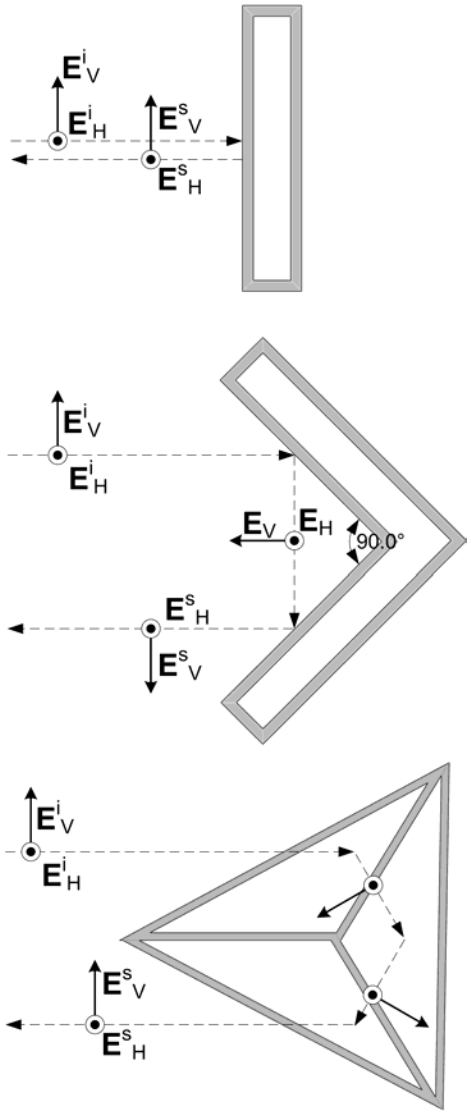

Figure 10. Reflection behavior for linearly polarized electric fields. The orientation of both the vertical and horizontal components of the electric field are unperturbed after an odd number of bounces (top and bottom). However, the vertical component of the electric field becomes inverted following a double bounce (middle) [6].

Cameron [20]. Figure 10 uses linear polarization pairs to illustrate the motivation behind such canonical scatterer analysis. The orientations of both the vertical and horizontal components of the electric field are unperturbed after a single bounce as shown in the top diagram. In contrast, the vertical component of the electric field, $\vec{E}_V$, becomes inverted after a double bounce as shown in the bottom diagram. After

a triple bounce, such as may be experienced in the well of a trihedral, a double inversion will cause the scattered field to return to its original orientation as shown in the bottom diagram. As such, the vertical component of the electric field is inverted for all even-bounce geometries and is unchanged for all odd-bounce geometries. The linear polarization Sinclair matrix for ideal odd-bounce geometries is thus given by

$$\mathbf{S_o} = \begin{bmatrix} 1 & 0 \\ 0 & 1 \end{bmatrix}. \tag{17}$$

While the linear polarization Sinclair matrix for ideal even-bounce geometries is given by

$$\mathbf{S_e} = \begin{bmatrix} 1 & 0 \\ 0 & -1 \end{bmatrix}. \tag{18}$$

In fact, these matrices comprise two terms of the matrix decomposition based on Pauli spin matrices (referred to as Pauli decomposition)[92]

$$\mathbf{S} = \begin{bmatrix} S_{HH} & S_{HV} \\ S_{VH} & S_{VV} \end{bmatrix} = a \begin{bmatrix} 1 & 0 \\ 0 & 1 \end{bmatrix} + b \begin{bmatrix} 1 & 0 \\ 0 & -1 \end{bmatrix} + c \begin{bmatrix} 0 & 1 \\ 1 & 0 \end{bmatrix} + d \begin{bmatrix} 0 & -j \\ j & 0 \end{bmatrix}, \tag{19}$$

where a, b, c, and d are complex valued and given by [92]

$$a = \frac{S_{HH} + S_{VV}}{2} \quad b = \frac{S_{HH} - S_{VV}}{2} \quad c = \frac{S_{HV} + S_{VH}}{2} \quad d = j\frac{S_{HV} - S_{VH}}{2}. \tag{20}$$

Note that for monostatic backscatter, $d = 0$.

In order to better understand Pauli decomposition, it is beneficial to further examine the double-bounce mechanism depicted in the middle diagram of Figure 10. Note that the horizontal component of the incident electric field, $\vec{E}_H^i$, is parallel to the dihedral fold line. If the situation were altered by rotating the dihedral fold line

by 90°, then the vertical component of the incident electric field, $\vec{E}_V^i$, would become parallel to the fold line. Conversely and according to this new orientation, $\vec{E}_H$ would be inverted while $\vec{E}_V$ would remain unchanged overall. Such a change in orientation is referred to as a roll. In Equation (19), a 90° roll would simply invert the sign of b, leaving the magnitude unchanged. However, in general, the magnitude of b depends upon roll angle.

The third term of Equation (19) can be interpreted to represent backscatter from a dihedral with a fold line rotated 45-degrees, as compared to that shown in the middle diagram of Figure 10 [92]. Therefore, dihedrals of arbitrary roll contribute to both the second and third terms of the Pauli decomposition. In response, Krogager proposed a roll-invariant decomposition of the Sinclair scattering matrix [86, 87]. The Krogager decomposition expressed in circular polarization bases can be modeled as [91]

$$\mathbf{S} = \begin{bmatrix} S_{RR} & S_{RL} \\ S_{LR} & S_{LL} \end{bmatrix} = K_o \begin{bmatrix} 1 & 0 \\ 0 & 1 \end{bmatrix} + K_e \begin{bmatrix} 1 & 0 \\ 0 & -1 \end{bmatrix} + K_h e^{-j2\varphi} \begin{bmatrix} 0 & 1 \\ 1 & 0 \end{bmatrix}, \quad (21)$$

where the phase difference between HH and VV polarizations is assumed to be zero and φ is called the helix phase angle.

The coefficients K_o, K_e, and K_h can be extracted from polarization diverse SAR images on a pixel-by-pixel basis using [90]

$$\begin{aligned} K_o &= |S_{RL}|, \\ K_e &= \min(|S_{LL}|, |S_{RR}|), \\ K_h &= \text{abs}(|S_{RR}| - |S_{LL}|)|, \end{aligned} \quad (22)$$

where the coefficients represent the strength of odd-bounce, even-bounce, and helical scattering, respectively. This interpretation is valid for all canonical scatterers [92].

Table 3. Krogager and Frequency Response Parameters for Canonical Point Scattering Geometries.

Scattering geometry	α	κ_o	κ_e
flat plate or trihedral	2	1	0
dihedral	2	0	1
cylinder/cone specular	1	1	0
top hat	1	0	1
sphere	0	1	0
straight edge/wire specular	0	0.5	0.5

The relative strengths of odd-bounce and even-bounce scattering can be determined by

$$\kappa_o = \frac{|K_o|}{\sqrt{|K_o|^2 + |K_e|^2 + |K_h|^2}}, \tag{23}$$

$$\kappa_e = \frac{|K_e|}{\sqrt{|K_o|^2 + |K_e|^2 + |K_h|^2}}, \tag{24}$$

where κ_o and κ_e are real-valued, normalized scattering intensities measured at a given image location or pixel. In this case, the amount of helical scattering can be interpreted as relating to the purity of the even-bounce scattering [88].

By simply combining these Krogager parameters with the frequency parameter from Table 2, some of the ambiguity between scatterers can be resolved in three dimensions. A listing of ideal canonical point scatterers based on these three parameters is given in Table 3.

2.2.3.3 *Observations.*

The goal of scattering matrix decomposition is to produce a set of basis matrices which can give insight into the type of scattering present in a radar signal [92]. Such insight has been shown to aid target detection and image segmentation as described in the survey books [92, 112] and papers [33, 140]. These surveys describe how scattering matrix decomposition is fundamentally driven by the time-varying nature

of the target's polarimetric signal. If the signal can be approximated as time-invariant, then coherent scattering matrix decompositions are appropriate. However, if the signal is time-variant, then power-type matrix decompositions are required [112].

When applicable, coherent scattering matrix decompositions are preferred because they can better describe physical scattering mechanisms [112]. Furthermore, coherent scattering matrices for backscattering have only five independent variables as compared to ten for the power-type matrices [112]. Fortunately, the scatterer classification algorithm developed in this dissertation only extracts polarimetric features from pixels where the response from a single canonical scatterer dominates. In this case, the polarization response can be approximated as time-invariant, and the coherent scattering matrix decomposition is applicable [92].

There are three well-established coherent scattering matrix decompositions that have been proposed in the literature. These are Pauli [33], Krogager [87], and Cameron [20]. The Pauli decomposition is adopted from the Pauli spin matrices originating in physics and optics. It results in orthogonal basis matrices which for radar backscattering can be interpreted as a sphere, a dihedral with a zero-degree roll, and a dihedral with a 45-degree roll. The Krogager decomposition is presented as a roll invariant alternative to the Pauli decomposition. It has the advantage of separating odd-bounce from even-bounce backscattering. The basis matrices for Krogager decomposition can be interpreted as a sphere (odd-bounce), a dihedral (even-bounce), and a helix. A disadvantage of Krogager decomposition is that the basis matrices are not orthogonal. This results in backscatter from double dihedrals to appear as helical. The Cameron decomposition attaches a great deal of importance to a class of targets which Huynen termed symmetric [71]. A symmetric target has an axis of symmetry in the plane orthogonal to the radar line of site. For these targets, decomposition follows a decision tree where very detailed target information can be gleaned.

Table 4. Comparison of Coherent Scattering Matrix Decompositions.

Decomp.	Recent Publications	Advantages	Limitations
Pauli	2010 Inci [72] 2010 Brigui [16]	orthogonal basis	not roll invariant
Krogager	2008 Ainsworth [2] 2010 Zou [154]	roll invariant	not an orthogonal basis
Cameron	2009 Cameron [21] 2009 Martorella [101]	details symmetric targets	wide apertures degrade symmetry high-order feature space
Touzi	2008 Brisco [17]	roll invariant orthogonal basis	focused toward non-coherent decomposition new and relatively unproven

It is important to note that Touzi has also made some significant contributions to the study of coherent scattering matrix decompositions. He recently presented a coherent decomposition that is both orthogonal and roll invariant [139], combining the strengths of the Pauli and Krogager decompositions, respectively. His intent was to produce a decomposition that was useful for both coherent scattering matrix and power-type matrix decomposition. Cameron recently raised the question of the uniqueness of his approach [21], and at this time, it is unclear if the Touzi decomposition will rival the popularity of the three well-established coherent scattering matrix decompositions previously discussed.

A summary of the advantages and limitations of each method is provided in Table 4. Because the primary contribution of this dissertation lies in the development of a new method for characterizing the anisotropic and dispersive characteristics of scatterers, the choice of scattering matrix decomposition method is secondary. The Krogager decomposition is chosen because of its simplicity and roll-invariance. Although the Cameron decomposition would potentially provide more information, this comes at the expense of increasing the dimensions of the feature space and at the restriction of narrow apertures to preserve symmetry.

2.3 Feature Extraction and Classification

This section provides an introduction to some basic concepts in feature extraction and classification, as well as an overview of the feature extraction and least squares scatterer classification method featured in this dissertation. The subsections present some specific examples of feature selection, feature extraction, and least squares classification for canonical scatterers. These focus on use of the parameters for frequency, azimuth, and polarization dependency discussed previously in this chapter.

2.3.1 Feature Selection.

Feature selection is an engineering art, where the goal is to replace unwieldy high-order representations of objects with elegant lower-order approximations [108]. Within the limits of the approximation, this allows automated object detection and classification to be tractable on modern computers using signal detection and estimation theory. The features are derived from model-based parameters, statistical-based parameters, or both. An example model-based parameter is the order of the amplitude response with frequency, parameterized by α in Equation (12) of Section 2.2.1, which is shown in Table 3 to be useful in discriminating between some types of scatterers.

An example statistical-based parameter is the expected value of the pixel intensity associated with a given object. For instance, at X-band ($f = 9$ GHz) and referring to Figure 8 of Section 2.2.1, the radius of a sphere must be 360 meters in order to produce the same backscattered energy of a 1 meter long trihedral. Because such a large sphere is not expected in the scene, certain high-intensity pixels are not expected to be associated with a sphere. Alternately, statistical parameters are often derived from statistical pattern recognition techniques using training data. An example of training data is phase histories from scenes containing known objects at known locations. Because training data is scenario specific and this dissertation seeks a general theory

for scatterer classification, statistical parameters are excluded from the remaining discussion.

2.3.2 Feature Extraction.

Model-based feature extraction is accomplished by a series of linear and non-linear estimation techniques, depending upon the types of features being extracted. For instance, model parameters are easily extracted from SAR data by fitting measured data points and curves to responses predicted by the models. An example is image peak detection, which can be used to estimate the location (x_q, y_q) of the qth scattering center. Another example is least squares fitting of the main lobe of the sinc function in azimuth to a quadratic approximation in the spectral domain parameterized by L [3]. A final example is pixel summation from images of different polarizations to obtain the Krogager coefficients.

After the parameters are extracted, they are recorded in a feature vector. For canonical scatterers, all of the model parameters previously introduced in this chapter can be arranged in the feature vector

$$\mathbf{w} = [x, y, |A|, \angle A, \alpha, L, \theta_0, \kappa_o, \kappa_e]. \tag{25}$$

2.3.3 Least Squares Scatterer Classification.

Scatterer classification is accomplished by a likelihood ratio test, where the measured feature vector is compared to a set of ideal feature vectors, each representing a particular scatterer type. The simplest form of likelihood ratio test is the least squares classifier, where the vectors are represented in a Euclidean space and are compared using the Euclidean norm. The simplicity of the least squares classifier makes it the clearest method by which to test the hypotheses of this dissertation. Once the new

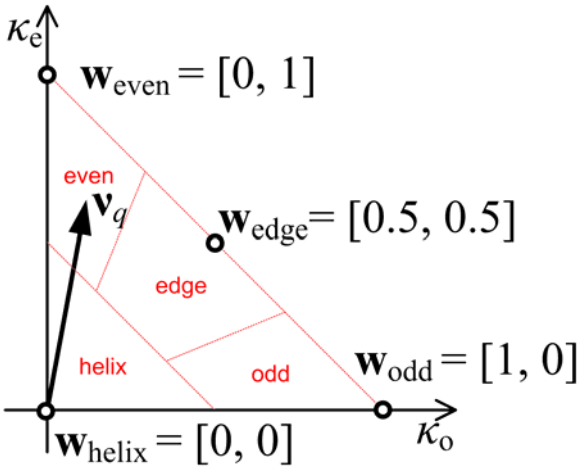

Figure 11. An example 2D feature space for a least squares classifier and four classes. The extracted feature vector, $\mathbf{v}_q$, is superimposed on a feature space divided into four regions by classification basis represented by ideal feature vectors $\mathbf{w}_{even}$, $\mathbf{w}_{edge}$, $\mathbf{w}_{odd}$, and $\mathbf{w}_{helix}$.

theory for scatterer classification via domain decomposition is established, follow-on work with more sophisticated classifiers can be accomplished.

An illustration of least squares classification with a two-dimensional feature vector, $\mathbf{w} = [\kappa_o, \kappa_e]$, is given in Figure 11. There are four ideal feature vectors, each corresponding to a different class of scatterer. The Euclidean norm divides the feature space into four regions, one for each class. An example extracted feature vector for the qth scatterer is illustrated by $\mathbf{v}_q$, which is nearest $\mathbf{w}_{even}$, as measured by the Euclidean norm. In this case, the qth scatterer is most likely a canonical scatterer producing an even-bounce, such as a dihedral.

2.3.3.1 *Observations.*

The entire gamut of pattern recognition techniques have been adapted for characterizing and identifying objects in SAR imagery [63, 142]. While, some of these techniques have proven useful in different applications, many approaches are limited by the dilemma of combinatorial complexity, especially as the number of features

increases [119]. In contrast, the use of simple physical models with only a few parameters has the advantage of producing efficient and optimal solutions, by the principle of Occam's razor [11].

Furthermore, scatterer classification results can be used as a first step in a tree algorithm or as an initialization mechanism for higher-order classification algorithms. For example, Reference [149] describes how information gleaned from a canonical scatterer classifier enables a secondary target classification algorithm to produce better separation between classes for subsequent hypothesis testing.

A least squares classifier is optimal when the desired signal is corrupted only by additive white Gaussian noise (AWGN). The thermal noise of a SAR system produces AWGN in the phase history [133]. Likewise, the image contains AWGN with a scaled variance due to coherent processing of the imaging operator [133]. However, because the frequency and polarimetric parameters are taken from the magnitude or intensity of an image, the noise affecting these parameters is expected to be colored. Furthermore, the interference due to neighboring scatterers and clutter is expected to be colored as well. As a result, the performance of the least squares classifier used in this dissertation is expected to be suboptimal.

Fortunately, there are some scenarios where the noise, clutter, and interference can be minimized, particularly for simple targets in free-space. Examples include stealthy aircraft in flight, streamlined spacecraft, and simple objects inside anechoic chambers. For other scenarios, such as imaging of the earth's surface or imaging of complex targets comprised of many scatterers in close proximity, the performance of the least squares classifier is expected to be suboptimal. Nonetheless, a least squares classifier is sufficient to illustrate the usefulness of the phase history decomposition method for scatterer classification.

III. Research Objective

This chapter serves as a foundation for the work in this dissertation. It presents the motivation for the research as well as some of the expected benefits and limitations of the new approach to imaging and scatterer classification based on phase history decomposition.

3.1 Motivation

SAR images contain bright spots representing locations where strong backscatterers are present in the scene. Within these bright spots are pixels having localized peak intensities, called image peaks. For example, Figure 12 is a SAR image of a residential scene taken from the moving and stationary target acquisition and recognition (MSTAR) data set, where bright spots and image peaks are noticeable throughout the image [38, 80].

Because the imaging operator assumes a scene consisting of ideal point scatterers, the dispersive, anisotropic, and polarimetric (DAP) characteristics of bright spots and peaks are not revealed in the image. Rather, these characteristics must be determined through additional analyses. By analyzing the DAP characteristics of bright spots and peaks, it is possible to measure the likelihood that a bright spot corresponds to a specific type of object. So, one may ask: By analyzing these characteristics in Figure 12, is it possible to determine whether the bright spots in ovals A and B are more likely due to automobiles or construction equipment or is it possible to determine if the bright line in oval C is more likely due to a fence or pipeline?

In general, the number of possible inquiries is unlimited, and reasonable answers depend upon contextual clues which are best deduced by human operators. Therefore, it is desirable to succinctly present the DAP characteristics of bright spots and peaks

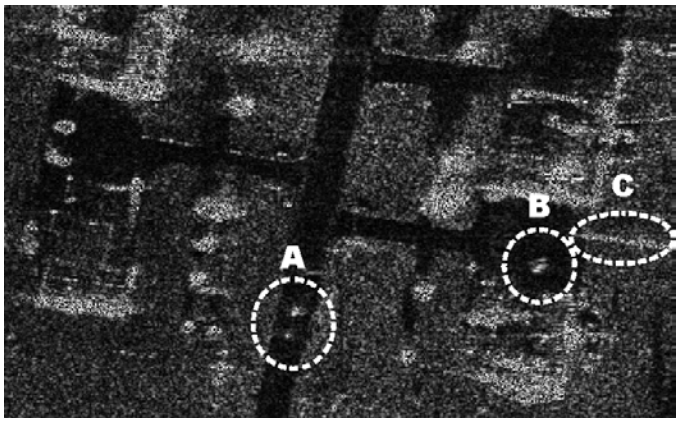

Figure 12. SAR image of a residential scene. Ovals A, B, and C represent bright spots of interest.

within the context of the image. Because SAR signals are processed in both the spatial and spectral domains, it is helpful to categorize dispersive and anisotropic analysis methods into two categories — image segmentation and phase history decomposition — according to the domain in which they decompose the signal. (The most common polarimetric analyses are performed in the spatial domain).

Image segmentation methods decompose the SAR signal in the spatial domain. The basic steps of the image segmentation methods are depicted in Figure 13. First, the segments are localized to bright spots or known locations of interest, such as segments A, B, and C. Then, a time-frequency transform is applied to each segment to produce a coarse resolution spectrum for further analysis. Image segmentation methods are best represented by two research projects: the hyperimage concept developed at ONERA, the French Aerospace Lab, [46, 47, 48] and parametric scatterer classification developed at The Ohio State University [3, 30, 62, 73]. Other image segmentation methods in the literature are generally a variation of these two primary methods.

The hyperimage concept simply displays the 2D resultant of a time-frequency transform. An example hyperimage is shown in Figure 14. Unfortunately, a human

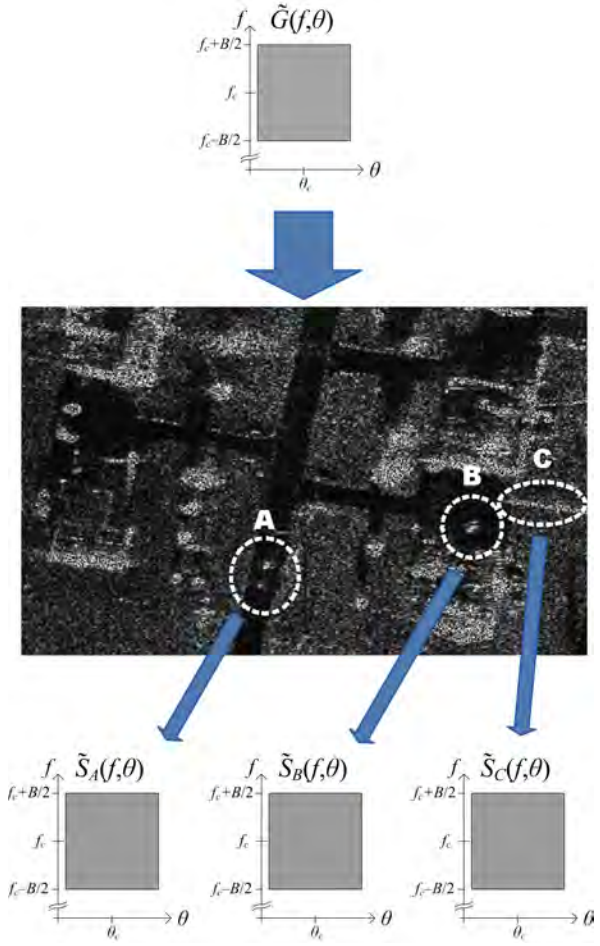

Figure 13. Basic steps of the image segmentation methods.

analyst must manually select the image segments and transforms. Then the analyst must scrutinize the resultants, each of which are displayed separately and outside the image. Thus, the hyperimage concept is best suited for highly trained analysts having ample time to conduct the analyses.

Parametric scatterer classification goes the extra step to match image segments and their spectra to the spectral and polarimetric responses expected for a set of ideal canonical scatterers. The set of canonical scatterers is limited, so that classification results can be succinctly represented by a small set of symbols and displayed as an overlay within the image context. Alternately, the classification results can be used

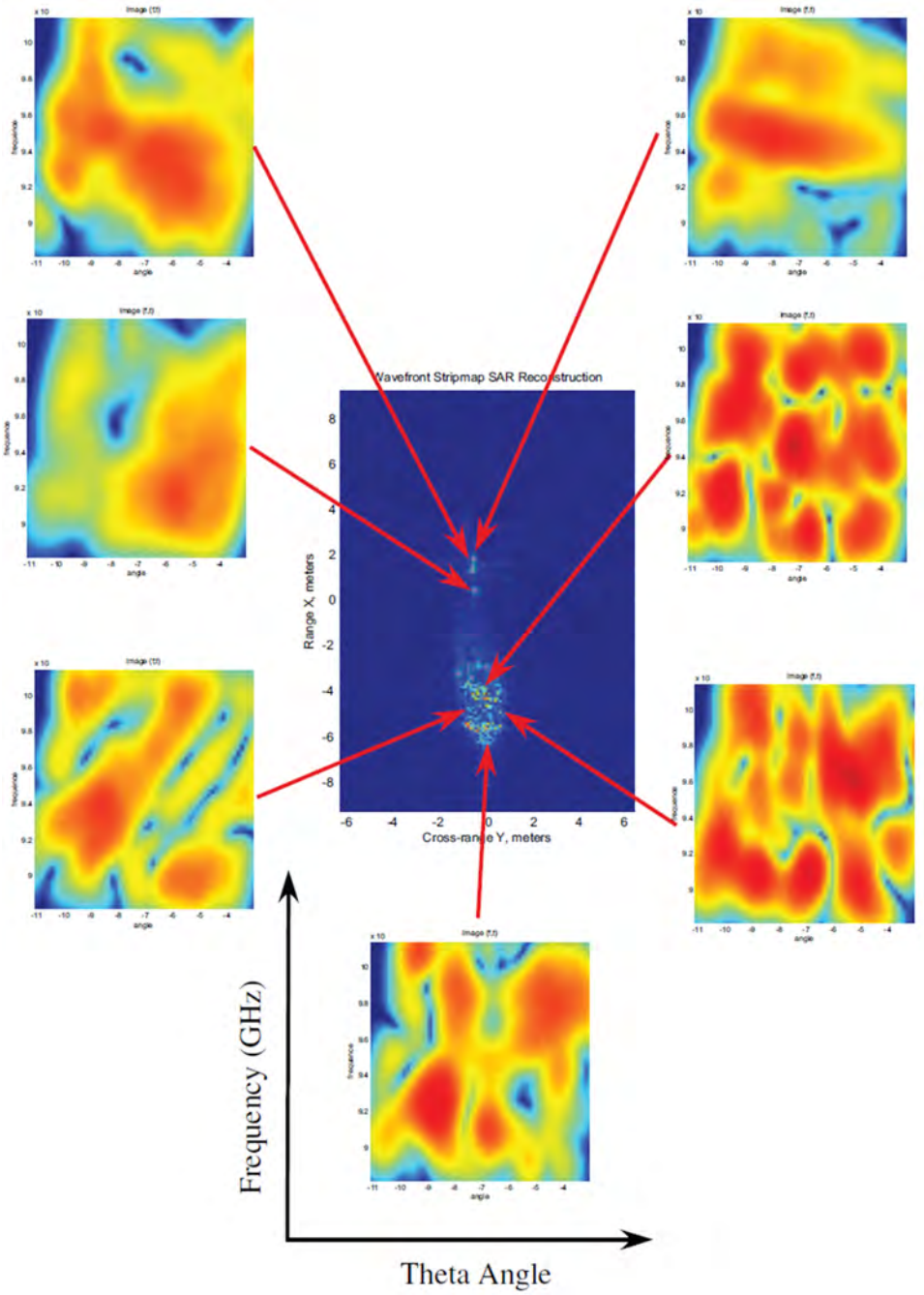

Figure 14. SAR image of a helicopter with example hyperimage displaying the spectra of seven image segments [46].

to simulate the phase history as a sum of canonical scatterers. From this simulated phase history, the bright spots in the original image can be reconstructed as shown

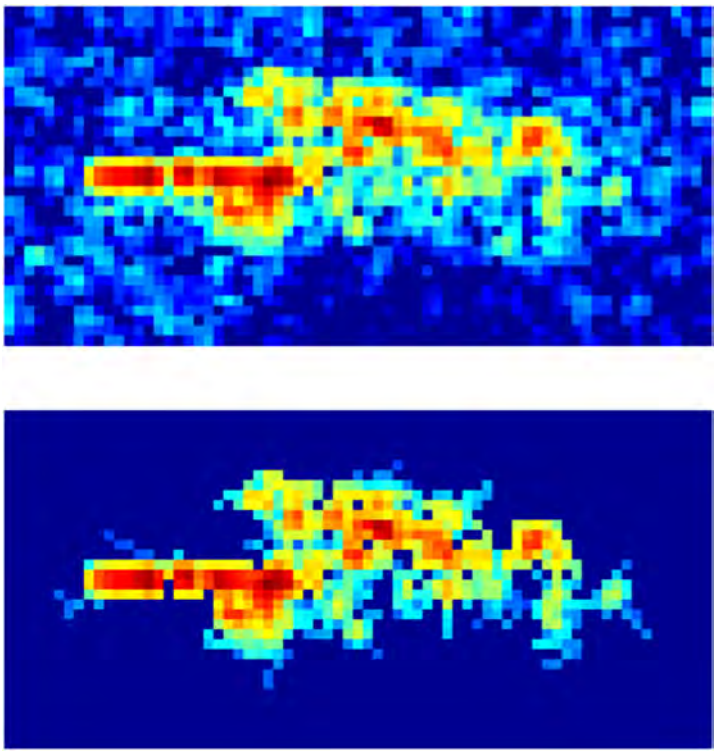

Figure 15. SAR image of T-72 tank from measured data (top) and simulated SAR image reconstructed from a canonical scatterer model (bottom). The model parameters were estimated using parametric scatterer classification with human supervision [30, 111].

in Figure 15. Classification accuracy is highly dependent upon the non-linear image segmentation process, and for typical scenes, human supervision is needed to ensure quality image segmentation [3, 62, 73]. In addition, when image segments contain energy from more than one canonical scatterer, the selection of model order, Q, also requires human supervision to ensure estimates of the model parameters are accurate [3, 62, 73]. Finally, classification accuracy suffers when image segments contain non-canonical scatterers, such as resonant cavities. Therefore, in practice, parametric scatterer classification demands human supervision at some point in the process to ensure accuracy. Unfortunately, existing image segmentation methods cannot succinctly present the DAP characteristics of bright spots and peaks within the image context in an operationally efficient, automated way.

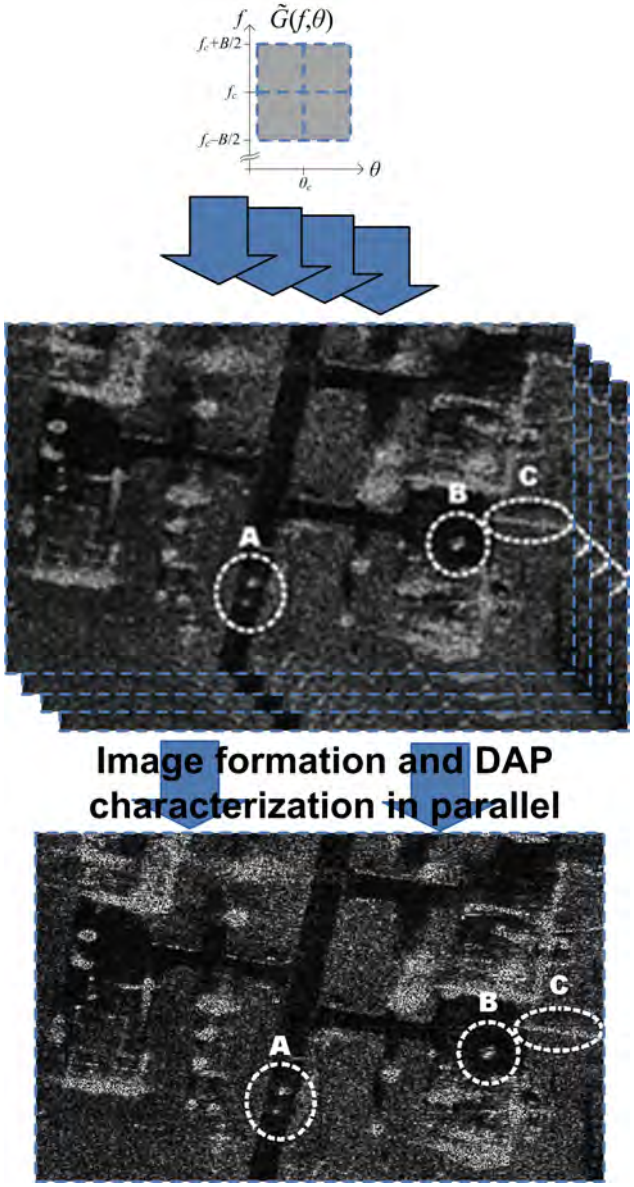

Figure 16. Basic steps of the phase history decomposition methods.

Phase history decomposition methods decompose the SAR signal in the spectral domain, as previously described in Section 2.1.2.2. The basic steps of phase history decomposition methods are depicted in Figure 16. The phase history is subdivided by regular intervals into subdomains, and coarse resolution subimages are reconstructed from each subdomain for further processing. In practice, angular bandwidth is less

restricted than frequency bandwidth; therefore, the most common decompositions are in azimuth, as previously described in 2.1.2.4. The full aperture is subdivided into two or more subapertures of equal width. The resulting subimages are diverse in azimuth, but with coarser resolution in cross-range than a full aperture image. These subimages reveal the anisotropic scattering behavior of each image pixel, which can be analyzed, or in the case of multilook SAR, averaged over the full aperture.

Similarly, for decompositions in frequency, the bandwidth is subdivided into two or more subbands. Because the available bandwidth is often limited, the subbands are usually equal to half of the full bandwidth. The resulting subimages are diverse in frequency, but with coarser resolution in range than a fullband image. These subimages reveal the dispersive scattering behavior of each image pixel, which can be analyzed or directly displayed in tri-color as shown in Figure 17.

By employing domain decomposition techniques, the coarse resolution subimages can be interpolated and summed to closely approximate a fine resolution image reconstructed from the full aperture, fullband SAR signal. Therefore, phase history decomposition methods are computationally efficient. In addition, DAP characteristics of bright spots or peaks can be automatically extracted from the subimages and succinctly presented within the image context without the need for image segmentation, spectral analysis, or most importantly, human supervision. Finally, note that polarimetric analyses commonly performed on images are also valid for use with subimages. Because of the advantages in operational and computational efficiency and the fact that canonical scatterers often comprise objects of interest, this dissertation develops a new SAR imaging and scatterer classification theory based on phase history decomposition.

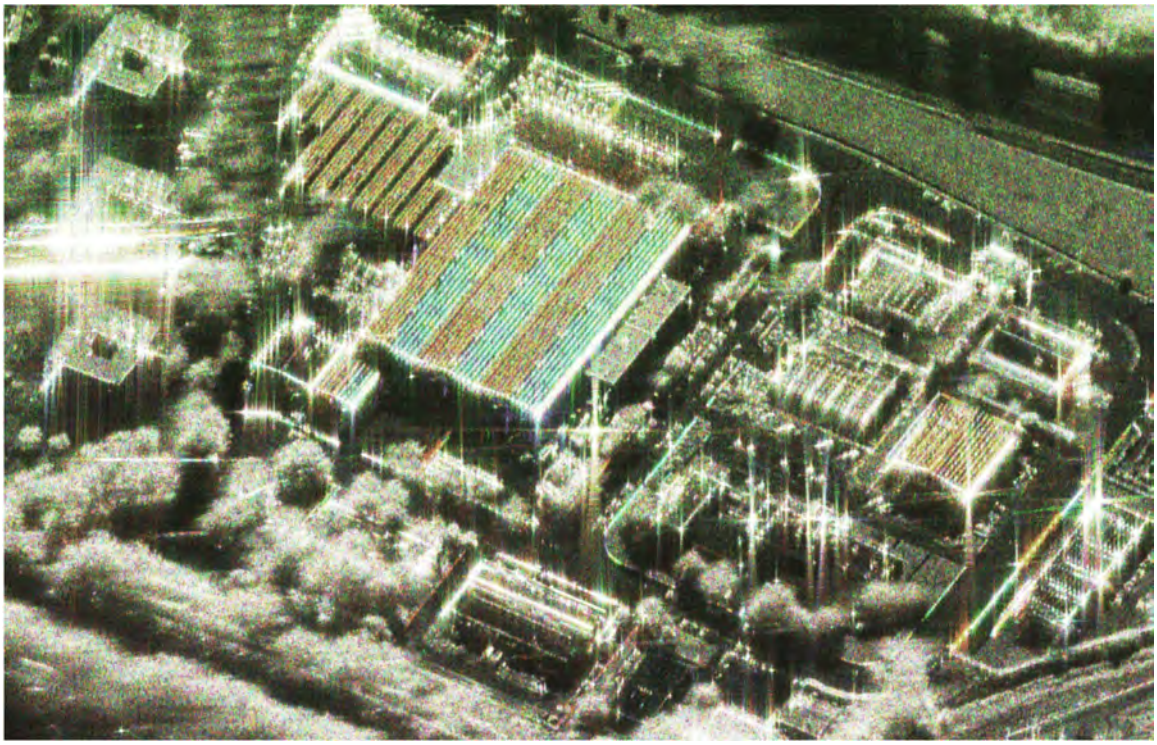

Figure 17. SAR image highlighting the dispersive characteristics of subimage pixels. Subbands centered on frequencies 8.8 GHz, 9.4 GHz, and 10 GHz are coded as red, green, and blue channels, respectively [46].

3.2 Proposed Solution

The new SAR imaging and scatterer classification theory centers around two hypotheses:

- it is possible to locate and classify canonical scatterers by observing the intensities of subimage pixels, and
- phase history decomposition makes this approach to classification highly efficient.

The first hypothesis requires development of a new model to predict the intensity of subimage peaks due to canonical scatterers. Such models are called peak models. For SAR signals, spatial resolution is inversely proportional to spectral bandwidth. This

is a manifestation of the Gabor limit [60]. Therefore, phase history decomposition methods essentially operate by sacrificing spatial resolution information to obtain spectral bandwidth information. Typically, the spectral diversity of the subimages is limited in order to maintain reasonable precision for scatterer localization. As a result, only slowly varying pixel intensities can be accurately measured by subimage analysis.

All canonical scatterers have a slowly varying amplitude response to changes in frequency, in accordance with Equation (12). However, only canonical point scatterers, defined as having $L \approx 0$ in Equation (13), have a slowly varying amplitude response to changes in azimuth. Canonical point scatterers, such as a trihedral, are characterized by the fact that their peak intensities are located at a *single* location, or point, in the image, similar to the peak of a digitized sinc function [42, 45, 57, 77, 122, 123, 131, 152, 153].

In contrast, distributed canonical scatterers, defined as having $L > 0$ in Equation (13), have a rapidly varying, sinc-like amplitude response in azimuth [62, 122]. Distributed canonical scatterers, such as the common dihedral with a fold-line oriented parallel to the imaging plane, are characterized by the fact that their energy usually spreads across multiple pixels. This is representative of a digitized rect function with a region of support over multiple samples and ripple in accordance with Gibbs phenomenon [107]. Thus, distributed scatterers often appear as a *set of in-line peaks* of approximately the same amplitude. For example, in Figure 16, Oval C shows a likely example of a distributed canonical scatterer, while Ovals A and B show likely examples of canonical point scatterers.

Peak models have already been developed to predict the intensity of subimage peaks due to canonical point scatterers [5, 57, 81, 117, 147, 150]. However, *no model exists to predict the intensity of subimage peaks due to distributed canonical scatterers.*

This dissertation develops a new multi-peak model to approximate the amplitudes of localized image peaks that typically appear at a single pixel or an in-line group of pixels in a SAR image. The multi-peak model assumes high frequencies and uses a wide angle approximation, but is an improvement over existing peak models because it explicitly accounts for distributed scatterers. It replaces the rapidly varying azimuth dependency of the amplitude function in the spectral domain with a slowly varying frequency dependency. In this way, the multi-peak model accounts for distributed scatterers while promoting the efficiencies associated with phase history decomposition methods.

The multi-peak model for a canonical scatterer with peak amplitude at location (x_q, y_q) can be expressed mathematically as

$$\begin{aligned} |\tilde{s}_q(x_q, y_q)| &= \left| \mathcal{B}\left\{ H_B H_\Theta \tilde{S}_q(f, \theta; \mathbf{w}_q) \right\}(x_q, y_q) \right| \\ &\approx \left| \mathcal{B}\left\{ H_B H_\Theta \tilde{S}_q(f; \mathbf{w'}_q) \right\}(x_q, y_q) \right|, \end{aligned} \tag{26}$$

where $\mathbf{w}_q$ is the set of parameters describing the amplitude function of the qth distributed canonical scatterer, while $\mathbf{w'}_q$ is a reduced set of parameters describing the amplitude function of the equivalent canonical point scatterer. The equivalent canonical point scatterer has an *azimuth-independent*, scaled amplitude function in the spectral domain and a frequency dependency of reduced order. The approximation is suitable for scatterers of sufficient electrical length and apertures of sufficient width. These are the high-frequency and wide-angle assumptions of the multi-peak model. Chapter IV develops the multi-point model and discusses the error due the approximation, as well as the conditions for which the error is well-controlled.

Not all image peaks are due to canonical scatterers. Therefore, there must be a process for separating image peaks due to canonical scatterers from image peaks due to non-canonical scatterers. Because non-canonical scatterers have amplitude

responses that are rapidly varying or discontinuous in frequency, their image peaks tend not to persist in subimages reconstructed from diverse subbands. Conversely, canonical scatterers have a slowly varying amplitude response in frequency and tend to persist. Therefore, the SPLIT algorithm uses a persistence criterion to reject non-canonical scatterers from the scatterer classification process.

For each persistent peak, SPLIT compares the peak intensities from all subimages to those predicted by the new multi-peak model. For example, in the case of two subimages, the ratio of subimage peak intensities is related to the subband center frequencies by [57]

$$\frac{|\tilde{g}_{1j}(x_q, y_q)|^2}{|\tilde{g}_{2j}(x_q, y_q)|^2} \approx \left(\frac{f_{c1}}{f_{c2}}\right)^{\alpha'+2}, \tag{27}$$

where α' is the parameter describing the order of the frequency dependency. Hence, the value of α' is estimated from the sampled image intensities on the left-hand side and known center frequencies on the right-hand side. Alternately, when more than two subimages at different subband center frequencies are analyzed, the estimation of α' becomes a straightforward curve fitting exercise [57]. When multiple polarizations are available, the SPLIT algorithm also extracts the Krogager parameters from the subimages. A least squares classifier compares the extracted parameters to the ideal parameters for each type of canonical scatterer, as listed in Table 5. The SPLIT algorithm and the error due to the narrow band approximation in Equation (27) are developed in detail in Chapter V.

The multi-peak model and SPLIT algorithm support the first hypothesis, while the second hypothesis is supported by the integrated algorithm. The integrated algorithm combines SPLIT-based classification with a domain decomposition imaging algorithm. The result is a computationally efficient scatterer classification algorithm that autonomously presents classification results within the image context. The computational complexity and cost of the integrated algorithm are presented in detail in

Table 5. Extended Frequency Response and Polarimetric Parameters for Ideal Canonical Scattering Geometries.

Scattering geometry	α'	κ_o	κ_e
trihedral	2	1	0
dihedral_{90}	2	0	1
cylinder_{90}	1	1	0
top hat	1	0	1
sphere, plate	0	1	0
edge/wire_{90}	0	0.5	0.5
dihedral_0	0	0	1
cylinder_0	-1	1	0
edge/wire_0	-2	0.5	0.5
helical	any	0	0

Chapter VI. Furthermore, all SAR imagery for the experiments in Chapter V were produced using the integrated algorithm.

In summary, the multi-peak model, SPLIT algorithm, and integrated algorithm form the foundation of a new theory for efficiently classifying canonical scatterers through phase history decomposition. The operational efficiency is the key motivation where DAP characteristics not readily available in the SAR image are made available automatically in a computationally efficient way. These characteristics can be succinctly displayed within the context of the SAR image and have the potential to highlight areas of interest to aid in the management of high precision tools and algorithms for SAR image analysis.

IV. New Multi-Peak Model

This chapter presents the new multi-peak model to approximate the amplitudes of localized image peaks that typically appear at a single pixel location or as an in-line set of pixels in a SAR image. The multi-peak model is derived from a wide-angle approximation of the well-known parametric model for canonical scatterers [62, 121], which in turn, is based on physical models of electromagnetic scattering. In this way, the multi-peak model is an improvement over existing peak models which poorly represent distributed canonical scatterers, such as the common dihedral with a fold-line oriented parallel to the imaging plane.

The multi-peak model approximates the image peak amplitudes due to distributed canonical scatterers as if they are due to an equivalent point scatterer with an azimuth-independent, dispersive amplitude function in the spectral domain. The approximation results from the action of the imaging operator, which integrates the sinc-like reflectivity pattern in azimuth over a sufficient aperture width. The relative error due to the approximation is shown to be two percent or less when a tapered window is used in azimuth, canonical scatterers are ten wavelengths long or longer, and aperture widths are ten degrees wide or wider. In addition, because scatterers with tilt angles near 0° behave as distributed scatterers and those with tilt angles near 90° behave as point scatterers, another advantage of the multi-peak model is that scatterer tilt angles near 0° and near 90° can be discriminated without the need for fully-polarimetric SAR data.

The chapter is organized as follows. Section 4.1 gives the mathematical expression for an image peak due to a canonical scatterer. It discusses how and under what conditions the imaging operator integrates the sinc-like amplitude response in azimuth to produce a point-like amplitude response for distributed scatterers. Section 4.2 presents numerical analysis to verify that error due to the approximation

is two percent or less when canonical scatterers are ten wavelengths long or longer and aperture widths are ten degrees wide or wider. Section 4.3 presents asymptotic analysis which further reveals that the model error is best controlled with the use of a tapered window in azimuth, such as the raised cosine windows employed in SAR imaging algorithms. Section 4.4 presents the new multi-peak model and describes how the model provides a reduced feature vector for scatterer classification by phase history decomposition. Section 4.5 presents some additional considerations for using the multi-point model with stripmap mode SAR collection geometries, where the synthetic aperture is usually limited to a few degrees. Finally, Section 4.5.1 summarizes the benefits and limitations of the new multi-peak model.

4.1 A Peak Model

From the scatterer models in Equations (7) of Section 2.1.3, (12) of Section 2.2.1, and (13) of Section 2.2.2, the phase history due to a canonical scatterer is parameterized by

$$\tilde{S}_q(f,\theta;\mathbf{w}_q) = \tilde{S}_f(f;A_q,\alpha_q) \times S_\theta(f,\theta;L_q,\theta_{0q})e^{-j2k|\mathbf{r}_q|}, \tag{28}$$

where $L_q > 0$ for a distributed canonical scatterer and $L_q \approx 0$ for a canonical point scatterer, setting $S_\theta \approx 1$. Thus, from Equations (9) and (10) of Section 2.1.3, the image due to the qth canonical scatterer is

$$\begin{aligned}\tilde{s}_q(x,y) = \frac{1}{2\pi}\int_{-\infty}^{\infty}\int_{-\pi}^{\pi} & H_B(f-f_c)H_\Theta(\theta-\theta_c)\tilde{S}_f(f;A_q,\alpha_q) \\ & \times S_\theta(f,\theta;L_q,\theta_{0q})e^{j2k(|\mathbf{r}|-|\mathbf{r}_q)|}|f|d\theta df.\end{aligned} \tag{29}$$

The peak amplitude of Equation (29) resides at location (x_q, y_q) in the image where $|\mathbf{r}| = |\mathbf{r}_q|, \forall\theta$. Thus, the peak amplitude is

$$\tilde{s}_q(x_q, y_q) = \frac{1}{2\pi} \int_{-\infty}^{\infty} H_B(f - f_c)\tilde{S}_f(f; A_q, \alpha_q)|f| \times \int_{-\pi}^{\pi} H_\Theta(\theta - \theta_c)S_\theta(f, \theta; L_q, \theta_{0q})d\theta df. \tag{30}$$

Note that the integral in azimuth of Equation (29) represents an inverse Fourier transform which affects the image of point scatterers and distributed scatterers differently. A point scatterer with $L \approx 0$ has a constant or slowly varying amplitude response in azimuth, and the image will contain a single peak in accordance with Equation (30). However, a distributed scatterer with $L \gg 0$ has a sinc-like amplitude function in azimuth, and given a sufficient aperture width, the image will contain a rectangular function with ripple. The ripple is a manifestation of Gibbs phenomenon [107] and results in one or more image peaks, depending upon the length of the scatterer and the dimensions of the image pixels. In this case, Equation (30) predicts the amplitude of the rectangular function, including any peaks caused by ripple. The multi-peak model derives its namesake from this effect, where distributed canonical scatterers typically appear as an in-line group of multiple peaks in the image.

Consider a distributed canonical scatterer oriented so that the main lobe of the sinc function is contained within the azimuth window. In this case, the resultant of the inner integral of Equation (30) is dominated by the area under the main lobe. Indeed, the sidelobes are small, diminished by the azimuth window, and add destructively, so as to contribute very little to the result. Note also that the width of the main lobe is inversely proportional to $\frac{2fL}{c}$. Thus, for a distributed canonical scatterer of fixed physical length and oriented so that the main lobe of the sinc function is contained within the azimuth window, the resultant of the inner integral has a magnitude that is inversely proportional to frequency.

This idea can be expressed by the mathematical approximation

$$\int_{-\pi}^{\pi} H_{\Theta}(\theta - \theta_c) S_{\theta}(f, \theta; L, \theta_0) d\theta \approx \frac{c\hat{A}}{2fL}, \quad \Theta > \Theta_{min}, \tag{31}$$

where Θ_{min} is the minimum aperture width for which the area under the main lobe of the sinc function dominates. Note that the $\hat{A}$ dependency on H_{Θ} and θ_0 is suppressed in the notation. This is a matter of convenience due to the assumption that azimuth window and orientation angle are fixed during phase history decomposition.

Note that the approximation in Equation (31) depends upon the electrical length of the scatterer, but this parameter is not usually controlled by the radar engineer. Thus, an appropriate minimum of $L \gtrsim 10\lambda$ is chosen in accordance with the high-frequency approximations of the underlying GO/GTD models [83]. Note also that the approximation depends upon aperture width to capture the mainlobe of the sinc function, and azimuth window to suppress the sidelobes of the sinc function. Both of these are controllable by the radar engineer and are of primary importance. The error introduced by the approximation and the window and aperture conditions for which the error is well-controlled are best understood and illustrated by numerical and asymptotic analysis.

4.2 Numerical Analysis

Numerical integration of Equation (31) for a range of frequencies and aperture widths is shown in Fig. 18, for the case of $L = 1$ meter and a Hanning window for H_{Θ}. Figures 18(a) and (b) reveal that $\hat{A}$ becomes independent of frequency when $\Theta \gtrsim 10^{\circ}$ and $f \gtrsim 3$ GHz for this case. Figure 18(c) also shows that this criteria is met for varying orientation angles θ_0. Because raised cosine windows, other than Hanning, are often used in SAR imaging [76], these were also investigated and were

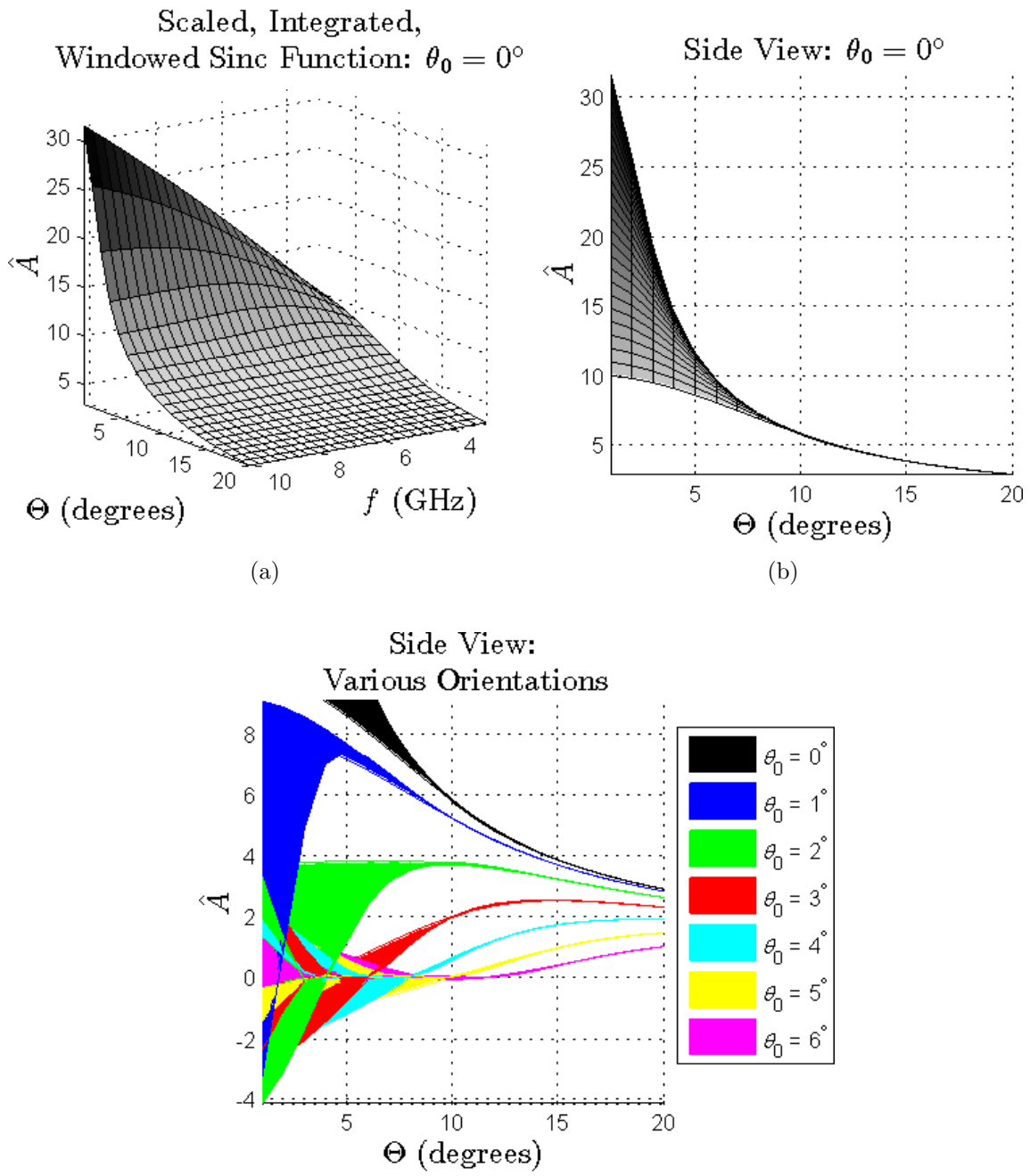

Figure 18. Numerical results for Eq. (31) where H_Θ is a Hanning function with region of support equal to Θ. The distributed scatterer is of length $L = 1$-meter.

observed to produce similar results to that shown in Fig. 18. The accuracy of the approximation decreases gradually as the scatterer becomes electrically shorter, that

is as f decreases or as L decreases in units of wavelength. The wavelength is defined as $\lambda = c/f$.

Because the model in Equation (29) is based on GO/GTD, it is most accurate for electrically large scatterers, where $L \gtrsim 10\lambda$. This is sometimes referred to as the physical optics region or high frequency approximation for electromagnetic scattering. Accordingly, the numerical integration results in Figure 18 are truncated at $f_{min} = 3$ GHz, where the $L = 1$ meter scatterer is ten wavelengths long. Therefore, $\Theta_{min} \approx 10°$ is sufficient to support a high frequency approximation for electromagnetic scattering, and for the purposes of this paper, apertures greater than ten degrees are considered to constitute wide-angle SAR. In other contexts, the definition for wide-angle SAR is constrained to the condition where bandwidth in frequency is much more limited than bandwidth in azimuth [96, 110, 146], but Equation (31) is not limited to this condition.

4.3 Asymptotic Analysis

Setting the limits of integration in Equation (31) to the region of support for H_Θ, $\theta \in [\theta_c - \frac{\Theta}{2}, \theta_c + \frac{\Theta}{2}]$, with the constraint $\frac{\Theta}{2} < \frac{\pi}{2} - |\theta_0|$ and setting $\theta_c = 0$ without loss of generality gives

$$\int_{-\frac{\Theta}{2}}^{\frac{\Theta}{2}} H_\Theta(\theta)\,\mathrm{sinc}\left[\tfrac{2}{c} f L \sin(\theta - \theta_0)\right] d\theta. \tag{32}$$

The change of variables $a = \frac{2fL}{c}$ and $x = \sin(\theta - \theta_0)$ further simplifies the integral to

$$\hat{A} \approx \int_{-1}^{1} \left[\frac{H_\Theta(\theta_0 + \sin^{-1} x)}{\sqrt{1 - x^2}}\right] a\,\mathrm{sinc}(ax) dx, \tag{33}$$

where the earlier constraint causes the limits of integration to be constrained to the interval $\left[\sin\left(-\frac{\Theta}{2} - \theta_0\right), \sin\left(\frac{\Theta}{2} - \theta_0\right)\right]$, or more generally $x \in [-1, 1]$. As a approaches infinity, the second factor in Equation (33) is a form of the Dirac delta function [95].

Under this limit, the sinc function becomes a sampling function so that the first factor is sampled at $x = 0$, and

$$\lim_{a\to\infty} \hat{A} = \lim_{a\to\infty} \int_{-1}^{1} \left[\frac{H_\Theta(\theta_0 + \sin^{-1} x)}{\sqrt{1-x^2}} \right] a\,\mathrm{sinc}(ax)dx$$

$$= H_\Theta(\theta_0), \tag{34}$$

where $H_\Theta(\theta_0)$ is assumed positive for $|\theta_0| < \frac{\Theta}{2}$ and zero otherwise. Under the limit, $\hat{A}$ equals a constant; therefore, the error introduced by the wide-angle approximation in Equation (31) is bounded. That is, for any typical azimuth window, the error bound diminishes with increasing frequency, or equivalently as the distributed scatter increases in electrical length.

Bounded error alone is not sufficient to make the wide-angle approximation generally useful for time-frequency analysis of SAR imagery. It is also important that $\hat{A}$ be insensitive to changes in frequency, or equivalently, changes in a. This sensitivity is revealed by taking the partial derivative with respect to a of the right hand side of Equation (33), where a partial derivative equal to zero reveals that $\hat{A}$ is independent of a. Thus, noting that $\frac{\partial(a\,\mathrm{sinc}(ax))}{\partial a} = \cos(\pi a x)$, the wide-angle approximation relative error is defined as

$$\epsilon(H_\Theta, a, \theta_0) = \frac{\left| \int_{-1}^{1} \left[\frac{H_\Theta(\theta_0 + \sin^{-1} x)}{\sqrt{1-x^2}} \right] \cos(\pi a x)dx \right|}{H_\Theta(\theta_0)}, \tag{35}$$

where $\epsilon = 0$ indicates that $\hat{A}$ is independent of a. Plots of the error are shown in Fig. 19 for the case of $\theta_0 = 0$ and for cases $a = 20$ and $a = 40$. The plots compare the errors of a rectangular azimuth window and three other windows commonly used in SAR image processing [76]. All windows are in accordance to Matlab® default definitions. The Hanning window appears to perform best overall, while the Taylor

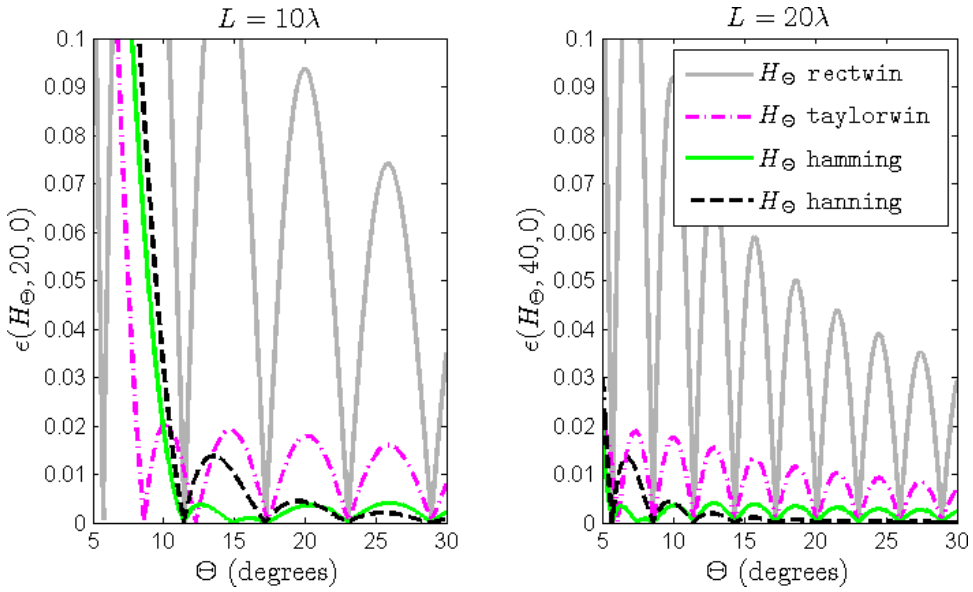

Figure 19. Wide-Angle approximation relative error for a rectangular window in azimuth and three other windows commonly used in SAR image processing.

window performance is marginal, and the rectangular window performance is notably poor. Similar results are obtained for larger values of a, but with lower overall error, as expected. Also as expected, the error increases rapidly for an aperture width less than ten degrees, regardless of window type. In addition, the results are similar for varying values of θ_0. Because a rectangular window in azimuth causes much larger error than that caused by a tapered window, the multi-peak model is recommended for use with tapered windows, such as the family of raised cosine windows typically employed for SAR imagery.

4.4 The Multi-Peak Model

Based on the azimuth limitations of the model, the peak amplitude of the qth scattering center in Equation (30) is approximated as

$$\tilde{s}_q(x_q, y_q) \approx \frac{1}{2\pi} \int_{-\infty}^{\infty} H_B(f - f_c) A_q (jf)^{\alpha_q/2} |f| \left[\frac{c\hat{A}_q}{2fL_q} \right] df \tag{36}$$

for scatterers of sufficient length ($L \gtrsim 10\lambda$) and an aperture of sufficient width ($\Theta \gtrsim 10°$). Here, the phase history due to the qth scatterer is independent of θ. This result is derived from Equation (30) when expressed in polar coordinates, but a similar result can be obtained for rectangular coordinates using the far field approximation, $R(x,y) \approx x\cos\theta + y\sin\theta$, and the small angle approximation, $f = \sqrt{f_x^2 + f_y^2} \approx f_y$. Therefore, for rectangularly formatted phase histories, an additional aperture limitation of $\Theta \lesssim 20°$ is required in order to support a small angle approximation.

Because L is usually not known *a priori*, it is desirable to modify Equation (36) to account for both distributed and point scatterers with a single parameter, α'. Adopting the form of Equation (12), a convenient form for Equation (36) is

$$\tilde{s}_q(x_q, y_q) \approx \frac{1}{2\pi}\int_{-\infty}^{\infty}\int_{-\pi}^{\pi} H_B(f - f_c)H_\Theta(\theta - \theta_c)\left[A'_q(jf)^{\alpha'_q/2}\right]|f|d\theta df, \qquad (37)$$

where

$$\tilde{S}_q(f; \mathbf{w'}_q) = A'_q(jf)^{\alpha'_q/2}e^{-j2k|\mathbf{r}_q|} \qquad (38)$$

is the phase history for an equivalent point scatterer to Equation (28) of Section 4.1.

For canonical point scatterers, $L \approx 0$, which in turn causes $\alpha' = \alpha$ and $A' = A$. For distributed canonical scatters, $L \gtrsim 10\lambda$ and $\Theta \gtrsim 10°$, which in turn causes $\alpha' = \alpha - 2$ and $A' = \frac{Ac\hat{A}j}{2L\int H_\Theta(\theta-\theta_c)d\theta}$. This supports the hypothesis expressed in Equation (26) of Section 3.2 where $\mathbf{w} = [x, y, A, \alpha, L, \theta_0]$ from Equation (28) and $\mathbf{w'} = [x, y, A', \alpha']$ from Equation (38). Therefore, the SAR image peak amplitude due to a distributed canonical scatterer can be modeled as due to an equivalent canonical point scatterer having an azimuth-independent, scaled amplitude function in the spectral domain and a frequency dependency of reduced order.

The fact that image peaks due to *any* canonical scatterer can now be approximated as due to a canonical point scatterer is central to the high-frequency multi-peak model

Table 6. Extended Frequency Response Parameter for Ideal Canonical Scattering Geometries.

Scattering geometry	α'
trihedral, dihedral$_{90}$	2
cylinder$_{90}$, top hat	1
sphere, plate, edge/wire$_{90}$, dihedral$_0$	0
cylinder$_0$	-1
edge/wire$_0$	-2

for wide-angle SAR. This new model provides an extension of the traditional point model in Equation (12) of Section 2.2.1, and as a result, Table 2 of Section 2.2.1 expands to become Table 6. Aside from the plate, which is symmetric under the model in two dimensions, the distributed scatterers are discriminated from their point scatterer variants by tilt angles of 0° and 90°, as indicated by a subscript. A benefit of the multi-peak model is that scatterer tilt angles of $\tau \approx 0°$ and $\tau \approx 90°$ can be discriminated without the need for fully-polarimetric SAR data.

If fully polarimetric data is available, ambiguity between most scatters can be further resolved using a Krogager decomposition to obtain proportions of the odd-bounce, even-bounce, and helical scattering [86]. Table 5 lists the new frequency parameter α' with the odd and even bounce parameters κ_o and κ_e, respectively. Using this basis for classification, only the sphere and plate are ambiguous. When the phase history is imaged over multiple, wide-angle subapertures, then for reasonable elevation angles (e.g. less than 60°), point scatterers will tend to persist across multiple subaperture images, whereas, distributed scatterers do not persist. In this case, a persistence criteria can be used to further resolve ambiguity between distributed and point scatterers, such as the sphere and plate. The papers [26, 96, 110, 137] and their references contain information on scatterer persistence which, for brevity, are not addressed in this dissertation.

4.5 Stripmap Mode SAR Considerations

The multi-peak model is accurate for the case of $L \gtrsim 10\lambda$ and $\Theta \gtrsim 10°$. However, stripmap mode SAR systems often have aperture widths less than 10°. In addition, the multi-peak model also assumes an imaging operator that is a 2D transform between the spectral and spatial domains. However, some stripmap mode imaging algorithms do not operate in the 2D spectral domain. In response to these restrictions, this section examines the special considerations that govern the use of the multi-peak model with stripmap mode SAR systems.

The angular diversity in stripmap SAR signals is ultimately restricted to the width of the azimuth beamwidth. Furthermore, a narrow azimuth beamwidth is usually desired for two primary reasons. The first is a matter of antenna gain. A narrow beamwidth creates a higher antenna gain, improving the overall signal to noise ratio of the SAR system [36]. The second is a matter of pulse repetition frequency (PRF). The PRF determines the Doppler sampling rate, and so a higher PRF provides for a larger angular diversity without aliasing [36]. However, the PRF should also be low enough that the signal corresponding to the entire swath width can be received without range ambiguity [36]. These two requirements are in competition, and the PRF is usually chosen to limit angular diversity so as to obtain a wider swath width. Thus, as angular diversity is limited by PRF, very large azimuth beamwidths provide no additional advantage, in most cases.

The half-power beamwidth of a radar system can be approximated by [36]

$$\Theta \approx 0.88 \frac{c}{f_c l}, \tag{39}$$

where Θ is in units of radians, c is the speed of light, f_c is the center frequency of the radar signal, and l is the physical length of the antenna. For convenience, typical

Table 7. Azimuth Beamwidths of Various SAR System Types [52, 36, 37, 148, 129, 98, 128, 132, 97, 114, 69, 143].

Θ	System Type	Band	l(m)
$< 1^\circ$	spaceborne	X	5-15
$< 1^\circ$	spaceborne	C	8-15
1°	spaceborne	L	8-15
$1^\circ - 2^\circ$	airborne	X	0.6-1.1
$2^\circ - 4^\circ$	airborne	C	0.7-1.4
$7^\circ - 15^\circ$	airborne	L	0.7-1.6
$20^\circ - 115^\circ$	airborne	P	0.7-1.8

azimuth beamwidths for a variety of SAR systems are listed in Table 7. Here, typical wavelengths for X-, C-, L-band radars were approximately 9.6, 5.3, 1.3 GHz, respectively, while P-band frequencies varied.

For stripmap mode SAR, only airborne systems in L-band and P-band are expected to provide a large angular diversity, while other systems typically have an angular diversity of only a few degrees or less. For convenience, the remaining discussion equates the angular diversity or aperture of the SAR system to its half-power beamwidth in azimuth.

One significant limitation of the multi-point model is that it assumes azimuth integration is performed in the two-dimensional (2D) spectral domain. While integration of 2D spectral domain data is standard for most spotlight mode imaging algorithms, it is not standard for stripmap mode imaging algorithms. For instance, the range-Doppler algorithm (RDA) and the chirp scaling algorithm (CSA) perform azimuth integration in the range-Doppler domain, not the 2D spectral domain [36]. The range-Doppler domain is obtained by performing range-frequency integration before azimuth integration. As a result, the azimuth response of canonical scatterers is not integrated out at an appropriate level to allow the amplitude response of distributed canonical scatterers to become azimuth-independent. Therefore, a key assumption of the new multi-point model is violated for these imaging algorithms.

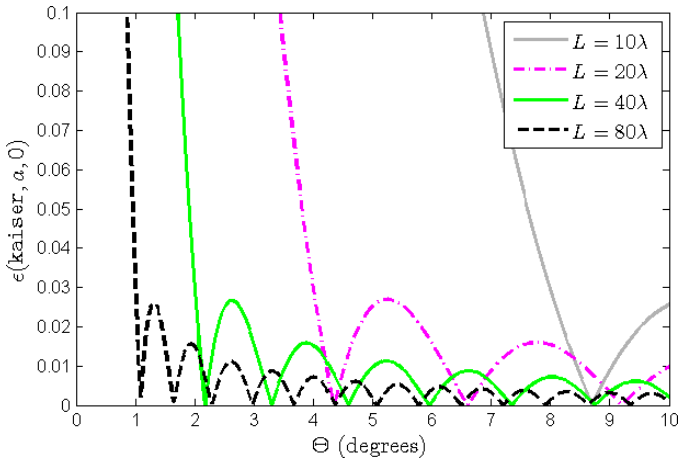

Figure 20. Relative wide-angle approximation errors for distributed canonical scatterers of varying lengths. H_Θ is a Kaiser window with a coefficient equal to 3.6 and a region of support equal to Θ.

Fortunately, the omega-K algorithm (OKA) is a stripmap mode imaging algorithm that has the advantage of processing data in the 2D spectral domain. In addition, the OKA is considered the most accurate of the stripmap mode imaging algorithms for SAR data collected over a wide-aperture [36]. For these reasons, the OKA is recommended for use with the new scatterer classification method for wide-angle SAR, whereas the RDA and CSA are not.

The accuracy of the multi-point model degrades with a narrowing aperture or a reduction in the electrical length of the scatterer. Specifically, as the scatterer becomes electrically longer, the model tolerates a narrower aperture. For example, plots of the relative wide-angle approximation error from Equation (35) for a Kaiser window with a coefficient equal to 3.6, an orientation angle of zero degrees, and a range of scatterer lengths are provided in Figure 20. (The Kaiser window simulates the azimuth beam pattern [36].) It can be seen that for a given subaperture width, the minimum length for which the multi-point model error is kept at near two-percent or less is $L_{min} \approx 80\lambda/\Theta$, where Θ is expressed in degrees. Using this error threshold

as an example and combining these results with Eq. 39, produces the relationship

$$L_{min} \approx 1.6l, \tag{40}$$

which can be used as a rule of thumb for estimating the minimum effective length of distributed scatterers which will be well modeled for a given SAR system. Additional analysis reveals that the factor 1.6 in Equation (40) is directly related to the broadening factor of the azimuth window. It follows that a window with a smaller broadening factor will produce a first null in the error function at a smaller aperture width, but at the expense of higher sidelobes. Sidelobes in the error function are controlled by choice of azimuth window. Additional analysis revealed that the raised cosine windows typically employed in radar imaging, such as Taylor, Hanning and Hamming, are sufficient to control modeling error. Such windows all have similar broadening factors which are not expected to have a great effect on the relationship given in Equation (40).

Using Equation (40) to evaluate the SAR systems listed in Table 7 reveals that the spaceborne radars possess antenna lengths which require distributed canonical scatterers with effective lengths of 10 to 20 meters in order to ensure accuracy of the multi-point model. In contrast, airborne radars are an order of magnitude shorter and effective lengths of only a few meters are sufficient. Last, note that the above analysis focused on distributed canonical scatterers, with an effective length $L > 0$. Recall that, canonical point scatterers, such as spheres and trihedrals, have a constant or slowly varying angular response in azimuth. Therefore, canonical point scatterers have an effective length of $L \approx 0$ and are modeled accurately, regardless of aperture width or antenna size.

4.5.1 Summary of Benefits and Limitations.

This chapter presented a new multi-peak model, as expressed in Equations (37) and (38) of Section 4.4, to predict the dispersive behavior of subimage peaks due to canonical scatterers. The model was shown to be an improvement over existing peak models because it accounts for common distributed canonical scatterers, including plates at broadside aspect, as well as dihedrals, cylinders, and edges/wires lying parallel to the imaging plane. For distributed canonical scatterers, the model approximates the amplitude response with a single factor having an inverse frequency dependency. This factor replaces the integration of the mainlobe of the sinc-like reflectivity pattern in azimuth as part of the imaging process. The approximation was shown to be valid for wide-angle SAR when the synthetic aperture is greater than ten degrees in azimuth. Furthermore, the model accuracy was shown to degrade gradually with a decrease in aperture width below ten degrees. The wide-angle approximation error was shown to be controllable, but is quite high for a rectangular window in azimuth. Therefore, the new multi-peak model is recommended for use with tapered windows.

The new multi-peak model is useful for scatterer classification by phase history domain decomposition methods. These methods sacrifice some precision in scatterer localization in order to gain efficiency by removing the need for human supervision typically required for image segmentation methods. Future follow-on research may reveal even more benefits of the new multi-peak model. However, notable limitations of the model include the following. Accuracy of the model is limited to the restricted apertures $\Theta \gtrsim 10^\circ$ for polar formatted data and $10^\circ \lesssim \Theta \lesssim 20^\circ$ for rectangular formatted data; scatterers must be of sufficient length ($L \gtrsim 10\lambda$) to support a high-frequency approximation; and a tapered window must be employed in azimuth to suppress the sidelobes of the sinc function. In addition, the multi-peak model is de-

veloped from GO/GTD scattering models which assume a perfect electrical conductor in the far field. Furthermore, the model assumes a normalized phase history accounting for antenna gain pattern, spherical wave propagation, and other losses. Lastly, for stripmap mode SAR, the accuracy of the model is limited to use of the Omega-K algorithm and distributed scatterers having an effective length approximately 1.6 times the physical length of the antenna.

V. SPLIT Algorithm

This chapter develops the SPLIT algorithm for classifying canonical scatterers. Section 5.1 explains how the SPLIT algorithm analyzes the pixels of all subimages within a given subaperture and extracts a feature vector based on the multi-peak model. Section 5.2 describes how these feature vectors are summed across multiple subapertures. Section 5.3 develops a least squares classification algorithm using the Euclidean norm for a set of ideal feature vectors, each representing a class of canonical scatterer. Section 5.4 presents SPLIT scatterer classification results for simulated and measured data. Finally, Section 5.5 examines the sensitivity of SPLIT classification accuracy to signal parameters, such bandwidth and interference due to neighboring canonical scatterers, clutter, and noise. It presents a statistical signal model with associated Monte Carlo simulations to illustrate the impact of bandwidth and interference on classification accuracy.

5.1 Subaperture Feature Extraction

The SPLIT algorithm analyzes the pixels of all subimages within a given subaperture and extracts a feature vector based on the multi-peak model. Given an $M \times N$ subimage, the feature vector for a peak at the subimage pixel (m, n) in the jth subaperture is

$$\mathbf{v}_j(m,n) = [\alpha', \kappa_o, \kappa_e]_j, \tag{41}$$

where α' is the frequency parameter of the multi-peak model and κ_o and κ_e are the proportion of odd-bounce and even-bounce scattering energy, respectively.

The following subsections describe the steps of the SPLIT algorithm. First, the scattering centers are localized to subimage pixels (m_q, n_q) using a peak detection algorithm. The peak detection algorithm identifies any peaks appearing at the same

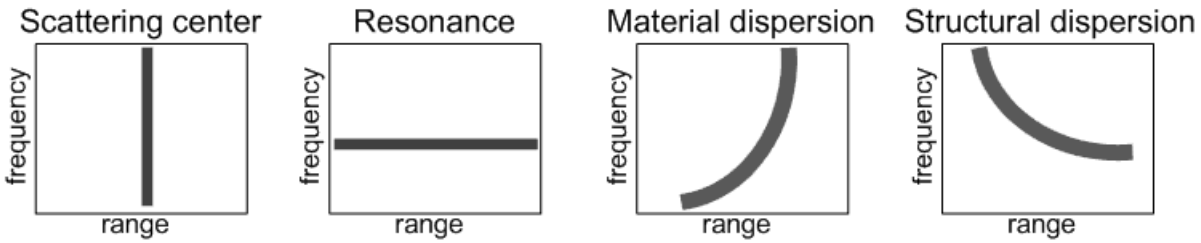

Figure 21. Scattering centers are stationary in range with changes in frequency [28].

location in all subimages. These stable peaks indicate a stationary and slowly varying amplitude response to changes in frequency, and thus, are likely due to canonical point scatterers. Next, SPLIT extracts the frequency parameter from the available co-polarization channels using a least squares estimator. Finally, SPLIT extracts the polarimetric parameters from each subimage using Krogager decomposition, as applicable.

5.1.1 Scattering Center Localization.

Scattering centers are stationary in range with changes in frequency, as illustrated by the simulated 1D range profiles of Figure 21. In addition, the multi-peak model predicts that image peaks due to canonical point scatterers have an amplitude that varies slowly with changes in frequency. Therefore, the subimage peaks due to canonical point scatterers are expected to be stable and occur at the same pixel coordinates in each subimage. In contrast, non-canonical scatterers, such as those due to resonance, material dispersion, structural dispersion, or scatter motion, are not expected to produce stable subimage peaks. In this way, the SPLIT algorithm determines the likely locations of canonical scatters using a stable subimage peaks detector.

The stable subimage peaks detector works as follows. For subimages of the jth subaperture, the SPLIT algorithm assigns a '1' to each pixel that is a local peak as compared to its neighboring pixels. It assigns all other pixels a '0.' The SPLIT

algorithm arranges the pixel values in an $M \times N$ array, one for each subimage. An illustrative example featuring three subimages is given by

$$|\tilde{g}_{1j}|^2 = \begin{bmatrix} 2 & 3 & 6 & 3 \\ 4 & 5 & 10 & 4 \\ 17 & 8 & 4 & 7 \\ 4 & 6 & 7 & 11 \end{bmatrix}, \quad |\tilde{g}_{2j}|^2 = \begin{bmatrix} 10 & 4 & 3 & 2 \\ 7 & 9 & 20 & 7 \\ 18 & 8 & 2 & 3 \\ 4 & 6 & 7 & 10 \end{bmatrix}, \quad |\tilde{g}_{3j}|^2 = \begin{bmatrix} 1 & 2 & 6 & 1 \\ 4 & 5 & 19 & 4 \\ 20 & 9 & 8 & 3 \\ 4 & 7 & 14 & 8 \end{bmatrix},$$

where the output of the peak detector, $\mathcal{D}\{\cdot\}$, for each subimage is

$$\mathcal{D}\left\{|\tilde{g}_{1j}|^2\right\} = \begin{bmatrix} 0 & 0 & 0 & 0 \\ 0 & 0 & 1 & 0 \\ 1 & 0 & 0 & 0 \\ 0 & 0 & 0 & 1 \end{bmatrix}, \quad \mathcal{D}\left\{|\tilde{g}_{2j}|^2\right\} = \begin{bmatrix} 1 & 0 & 0 & 0 \\ 0 & 0 & 1 & 0 \\ 1 & 0 & 0 & 0 \\ 0 & 0 & 0 & 1 \end{bmatrix}, \quad \mathcal{D}\left\{|\tilde{g}_{3j}|^2\right\} = \begin{bmatrix} 0 & 0 & 0 & 0 \\ 0 & 0 & 1 & 0 \\ 1 & 0 & 0 & 0 \\ 0 & 0 & 1 & 0 \end{bmatrix}.$$

The peak detector can be readily implemented using the `imregionalmax` function in Matlab®. The stable peaks are found by a simple element-wise multiplication, sometimes referred to as an array multiply. The result of the stable peak detector is

$$\bigotimes_{i=1}^{I} \mathcal{D}\left\{|\tilde{g}_{ij}|^2\right\} = \begin{bmatrix} 0 & 0 & 0 & 0 \\ 0 & 0 & 1 & 0 \\ 1 & 0 & 0 & 0 \\ 0 & 0 & 0 & 0 \end{bmatrix}. \tag{42}$$

where $\bigotimes$ represents array multiplication and $I = 3$ is the number of subimages. For the illustrative example in Equation (42), there are only two stable subimage peaks, and these pixel coordinates reveal the likely locations of canonical scatterers.

5.1.2 Frequency Parameter Estimation.

The SPLIT algorithm obtains a frequency parameter estimate by examining the intensities of the stable subimage pixels and comparing these intensities to those predicted by the multi-peak model. This section presents a mathematical development for a simple exponential relationship between the measured subimage pixel intensities and the known subband center frequencies. The exponent is directly related to the frequency parameter, α' of the multi-peak model. The relationship is based on a first order approximation using a narrow-band assumption. The following subsections examine the error due to the narrow-band approximation and describe a curve fitting procedure for estimating the frequency parameter from the peak intensity measurements.

5.1.2.1 First Order Approximation.

Starting with the multi-peak model for the qth scattering center from Equation (37) of Section 4.4 and signifying the wide-angle approximation with the $\widehat{\ }$ symbol gives the equality

$$\widehat{\tilde{s}}_q(x_q, y_q) = \frac{1}{2\pi} \int_{-\pi}^{\pi} H_\Theta(\theta - \theta_c) d\theta \int_{-\infty}^{\infty} H_B(f - f_c) \frac{A'}{j} (jf)^{1+\alpha'/2} df. \tag{43}$$

Setting $C = \frac{A'}{j2\pi} \int H_\Theta(\theta - \theta_c) d\theta$, assuming only positive frequencies, and applying a Taylor series expansion of $(jf)^{\alpha'/2}$ in the neighborhood of f_c gives

$$\widehat{\tilde{s}}_q(x_q, y_q) = C \int_{-\infty}^{\infty} H_B(f - f_c) \left[(jf_c)^{1+\alpha'/2} + \sum_{n=1}^{\infty} \frac{1}{n!} \left. \frac{d^n (jf)^{1+\alpha'/2}}{df^n} \right|_{f=f_c} (f - f_c)^n \right] df. \tag{44}$$

Defining $h_B(t)$ as the inverse Fourier transform (IFT) of $H_B(f)$ gives

$$\widehat{\tilde{s}}_q(x_q, y_q) = C(jf_c)^{1+\alpha'/2} h_B(0) + C \sum_{n=1}^{\infty} \frac{1}{n!} \left. \frac{d^n (jf)^{1+\alpha'/2}}{df^n} \right|_{f=f_c} \frac{h_B^{(n)}(0)}{j^n}, \tag{45}$$

where the second term contains higher-order functions resulting from the Taylor series expansion and frequency domain differentiation property of Fourier transforms [107].

Note that a symmetric azimuth window will cause all odd-ordered derivatives of $h_B^{(n)}(0)$ to become zero. Furthermore, for $\alpha' \in \{-2, 0\}$ the derivative with respect to f becomes zero for all n. These facts combined with a narrow-band assumption, causes the summation term in Equation (45) to be negligibly small in practice. For example, in the case of 4.0 GHz bandwidth at X-band, the relative error due to the approximation is less than one-percent. An analysis of the narrow-band approximation error is provided in the following subsection.

Consider the stable subimage pixel (m_q, n_q) dominated by the response due to a canonical scatterer at coordinates (x_q, y_q). In this case, a first-order approximation of the ratio of the pixel intensities between two subimages, having subwindows centered at two different center frequencies, f_{c1} and f_{c2} is

$$\frac{|\tilde{g}_{1j}(m_q, n_q)|^2}{|\tilde{g}_{2j}(m_q, n_q)|^2} \approx \frac{|C(jf_{c1})^{1+\alpha'/2} h_B(0)|^2}{|C(jf_{c2})^{1+\alpha'/2} h_B(0)|^2}. \tag{46}$$

Assuming a uniformity in the sampling and weighting of each subdomain (i.e. subwindows in azimuth are identical and each subband has an equal number of uniform samples) allows the constants in the numerator and denominator to cancel. This results in a simple relationship between the measured subimage pixel intensities and the subband center frequencies given by

$$\frac{|\tilde{g}_{1j}(m_q, n_q)|^2}{|\tilde{g}_{2j}(m_q, n_q)|^2} \approx \left(\frac{f_{c1}}{f_{c2}} \right)^{\alpha'+2}, \tag{47}$$

where the accuracy of the approximation is subject to three conditions:

1. the energy in the pixel is dominated by the backscattering from a canonical scatterer;

2. the wide-angle approximation error of the multi-peak model is well-controlled; and

3. the narrow-band approximation error resulting from ignoring the higher-order terms in Equation (45) is negligible.

The first assumption is addressed later in Section 5.5, the wide-angle approximation error was previously addressed in Sections 4.2 and 4.3, and the narrow-band approximation error is discussed in the following subsection.

5.1.2.2 Narrow-band Approximation Error.

This section examines the narrow-band approximation error, which results from ignoring the higher-order terms in Equation (45). The following derivation assumes that the subwindow in frequency is symmetric, with frequencies restricted to positive values, so that $f_c > 0$ and $B < 2f_c$. Under these conditions, the band limited integral of Equation (43) becomes

$$\widehat{\tilde{s}}_q(x_q, y_q) = C \int_{f_c - B/2}^{f_c + B/2} H_B(f - f_c)(jf)^{1+\alpha'/2} df. \tag{48}$$

Next, note that

$$(jf)^{1+\alpha'/2} = \left(\sqrt{j}\right)^{\alpha'+2} f^{1+\alpha'/2} = \left(\frac{\pm(1+j)}{\sqrt{2}}\right)^{\alpha'+2} f^{1+\alpha'/2}. \tag{49}$$

In order to analyze the error in the neighborhood of f_c, let

$$\begin{aligned}(jf)^{1+\alpha'/2} &= (jf_c)^{1+\alpha'/2} + (jf)^{1+\alpha'/2} - (jf_c)^{1+\alpha'/2} \\ &= \left(\frac{\pm(1+j)}{\sqrt{2}}\right)^{\alpha'+2} \left[f_c^{1+\alpha'/2} + f^{1+\alpha'/2} - f_c^{1+\alpha'/2}\right] \\ &= \left(\frac{\pm(1+j)}{\sqrt{2}}\right)^{\alpha'+2} f_c^{1+\alpha'/2} \left[1 + \left(\frac{f}{f_c}\right)^{1+\alpha'/2} - 1\right].\end{aligned} \tag{50}$$

Choosing to restrict the function $(jf)^{1+\alpha'/2}$ to positive roots, recalling that the window is centered on frequency f_c, setting $D = C\left(\frac{1+j}{\sqrt{2}}\right)^{\alpha'+2} f_c^{1+\alpha'/2}$, and substituting into Equation (48) gives

$$\begin{aligned}\widehat{\tilde{s}}_q(x_q, y_q) &= D\int_{f_c-B/2}^{f_c+B/2} H_B(f-f_c)\left[1 + \left(\frac{f}{f_c}\right)^{1+\alpha'/2} - 1\right] df \\ &= D\left\{h_B(0) + \int_{f_c-B/2}^{f_c+B/2} H_B(f-f_c)\left[\left(\frac{f}{f_c}\right)^{1+\alpha'/2} - 1\right] df\right\},\end{aligned} \tag{51}$$

where the first term represents the first order approximation of Equation (45) used in Equation (46) and the integral represents the error terms. The narrow-band relative error is defined as the magnitude of the error terms divided by the first order approximation term. With the change of variables $u = f - f_c$, the narrow-band relative error is

$$\varepsilon(H_B, \beta) = \frac{\left|\int_{-B/2}^{B/2} H_B(u)\left[\left(1 + \frac{u}{f_c}\right)^{1+\alpha'/2} - 1\right] du\right|}{h_B(0)}, \tag{52}$$

where the error is dependent upon the window function and fractional bandwidth, $\beta = B/f_c$.

A bound on the error can be derived by examining the integral in the numerator of Equation (52) partitioned about zero. Assuming a positive-valued window, $H_B(u) \geq 0$, then for the case of $\alpha' > -2$:

$$\int_{-B/2}^{0} H_B(u) \left[\left(1 + \frac{u}{f_c} \right)^{1+\alpha'/2} - 1 \right] du \leq 0 \leq \int_{0}^{B/2} H_B(u) \left[\left(1 + \frac{u}{f_c} \right)^{1+\alpha'/2} - 1 \right] du \tag{53}$$

Alternately, for the case of $\alpha' < -2$, the inequalities in Equation (53) are reversed. Note also that

$$\left| \int_{-B/2}^{0} H_B(u) \left[\left(1 + \frac{u}{f_c} \right)^{1+\alpha'/2} - 1 \right] du \right| \geq \left| \int_{0}^{B/2} H_B(u) \left[\left(1 + \frac{u}{f_c} \right)^{1+\alpha'/2} - 1 \right] du \right|. \tag{54}$$

Thus, from Equations (51) through (54) the error is bounded by

$$\begin{aligned} \varepsilon(H_B, \beta) \leq \frac{-\operatorname{sgn}(\alpha'+2)}{h_B(0)} \quad & \left\{ \int_{-B/2}^{0} H_B(u) \left[\left(1 + \frac{u}{f_c} \right)^{1+\alpha'/2} - 1 \right] du \right. \\ & \left. + \int_{0}^{B/2} H_B(u) \left[\left(1 + \frac{u}{f_c} \right)^{1+\alpha'/2} - 1 \right] du \right\}. \end{aligned} \tag{55}$$

Furthermore, assuming a rectangular window and applying the mean value theorem for integration produces an even tighter bound given by

$$\begin{aligned} \varepsilon(H_B, \beta) \quad \leq \quad & \frac{-\operatorname{sgn}(\alpha'+2)}{h_B(0)} \left\{ \int_{-B/2}^{0} H_B(u) \cdot \operatorname{mean} \left[\left(1 + \frac{u}{f_c} \right)^{1+\alpha'/2} - 1 \right] du \right. \\ & \left. + \int_{0}^{B/2} H_B(u) \cdot \operatorname{mean} \left[\left(1 + \frac{u}{f_c} \right)^{1+\alpha'/2} - 1 \right] du \right\} \\ \leq \quad & -\operatorname{sgn}(\alpha'+2) \left\{ \operatorname*{mean}_{-B/2<u<0} \left[\left(1 + \frac{u}{f_c} \right)^{1+\alpha'/2} - 1 \right] \right. \\ & \left. + \operatorname*{mean}_{0<u<B/2} \left[\left(1 + \frac{u}{f_c} \right)^{1+\alpha'/2} - 1 \right] du \right\}, \end{aligned} \tag{56}$$

where the mean values must be determined separately for the case of $\alpha' = -4$, because in this case, the exponent is -1.

For the case of $\alpha' \neq -4$:

$$\begin{aligned}
\underset{-B/2<u<0}{\text{mean}} \left[\left(1 + \frac{u}{f_c}\right)^{1+\alpha'/2} - 1 \right] &= \frac{2}{B} \int_{-B/2}^{0} \left[\left(1 + \frac{u}{f_c}\right)^{1+\alpha'/2} - 1 \right] du \\
&= \frac{2}{B} \left[\frac{2f_c}{4+\alpha'} \left(1 + \frac{u}{f_c}\right)^{2+\alpha'/2} - u \right] \Bigg|_{-B/2}^{0} \\
&= \frac{2}{B} \left[\frac{2f_c}{4+\alpha'} - \frac{2f_c}{4+\alpha'} \left(1 - \frac{B}{2f_c}\right)^{2+\alpha'/2} - \frac{B}{2} \right]
\end{aligned} \tag{57}$$

and

$$\begin{aligned}
\underset{0<u<B/2}{\text{mean}} \left[\left(1 + \frac{u}{f_c}\right)^{1+\alpha'/2} - 1 \right] &= \frac{2}{B} \int_{0}^{B/2} \left[\left(1 + \frac{u}{f_c}\right)^{1+\alpha'/2} - 1 \right] du \\
&= \frac{2}{B} \left[\frac{2f_c}{4+\alpha'} \left(1 - \frac{B}{2f_c}\right)^{2+\alpha'/2} - \frac{B}{2} - \frac{2f_c}{4+\alpha'} \right]
\end{aligned} \tag{58}$$

For the case of $\alpha' = -4$:

$$\begin{aligned}
\underset{-B/2<u<0}{\text{mean}} \left[\left(1 + \frac{u}{f_c}\right)^{-1} - 1 \right] &= \frac{2}{B} \int_{f_c - B/2}^{f_c} \left[\frac{f_c}{f} - 1 \right] df \\
&= \frac{2f_c}{B} \left[\ln(f) - \frac{f}{f_c} \right] \Bigg|_{f_c - B/2}^{f_c} \\
&= \frac{2f_c}{B} \left[\ln(f_c) - \ln\left(f_c - \frac{B}{2}\right) - \frac{B}{2f_c} \right]
\end{aligned} \tag{59}$$

and

$$\begin{aligned}\underset{0<u<B/2}{\text{mean}}\left[\left(1+\frac{u}{f_c}\right)^{-1}-1\right] &= \frac{2}{B}\int_{f_c}^{f_c+B/2}\left[\frac{f_c}{f}-1\right]df \\ &= \frac{2f_c}{B}\left[\ln\left(f_c+\frac{B}{2}\right)-\frac{B}{2f_c}-\ln(f_c)\right]\end{aligned} \tag{60}$$

From Equations (57) through (60) and recalling from Equation (45) that the error is zero for the case of $\alpha' = \{-2, 0\}$, the bound on the narrow-band approximation relative error is

$$\varepsilon(\text{rect},\beta) \leq \begin{cases} 0, & \alpha' \in \{-2,0\} \\ \dfrac{2}{\beta}\ln\left(\dfrac{2+\beta}{2-\beta}\right)-2, & \alpha' = -4 \\ \dfrac{-4\,\text{sgn}(\alpha'+2)}{\beta(4+\alpha')}\left[\left(\dfrac{2+\beta}{2}\right)^{2+\alpha'/2}-\left(\dfrac{2-\beta}{2}\right)^{2+\alpha'/2}\right] & \text{otherwise} \\ \qquad +2\,\text{sgn}(\alpha'+2), & \end{cases} \tag{61}$$

where the window in frequency is assumed to be a rect function given by $H_B(f) = \text{rect}[-B/2, B/2]$. The bounds for $\alpha' \in \{-1, 1, 2\}$ are shown in Figure 22 for a rect window. Note that the actual error is well below this bound for the case of a tapered window. For example, the results from a numerical analysis of Equation (52) for a Hanning window are shown in Figure 23. In this case, the error is less than one-percent for a fractional bandwidth of 0.5 or less.

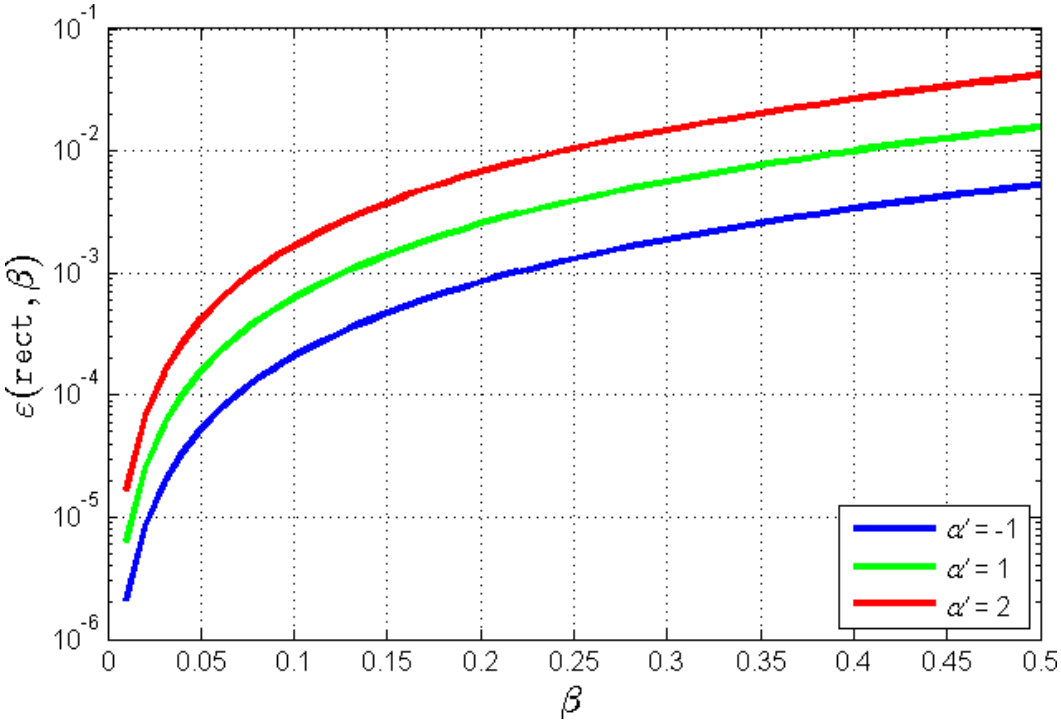

Figure 22. Narrow-band approximation relative error bounds in Equation (61) **as a function of fractional bandwidth for a rectangular window.**

5.1.3 Polar Reformatting Considerations.

The polar format algorithm (PFA) is a very common SAR imaging algorithm which deserves specific consideration. Recall that the derivation of Equation (47) assumed an imaging operator in polar coordinates with uniform sampling and weighting in each subdomain. However, the PFA features a rectangular imaging operator through a coordinate transformation that eliminates the $|f|$ factor, often referred to informally as the Jacobian [40]. Under the far field assumption and small angle approximation, $\Theta \lesssim 20°$, described earlier in Section 4.4, the multi-peak model is still valid. The far field assumption produces a polar to rectangular transformation given by $|f| df d\theta = df_x df_y$, $f = \sqrt{f_x^2 + f_y^2}$, and $\theta = \tan^{-1}(f_y/f_x)$ [76].

Note also that the effective sampling density changes during polar to rectangular reformatting as shown in Figure 24. In the case of an inscribed rectangle and

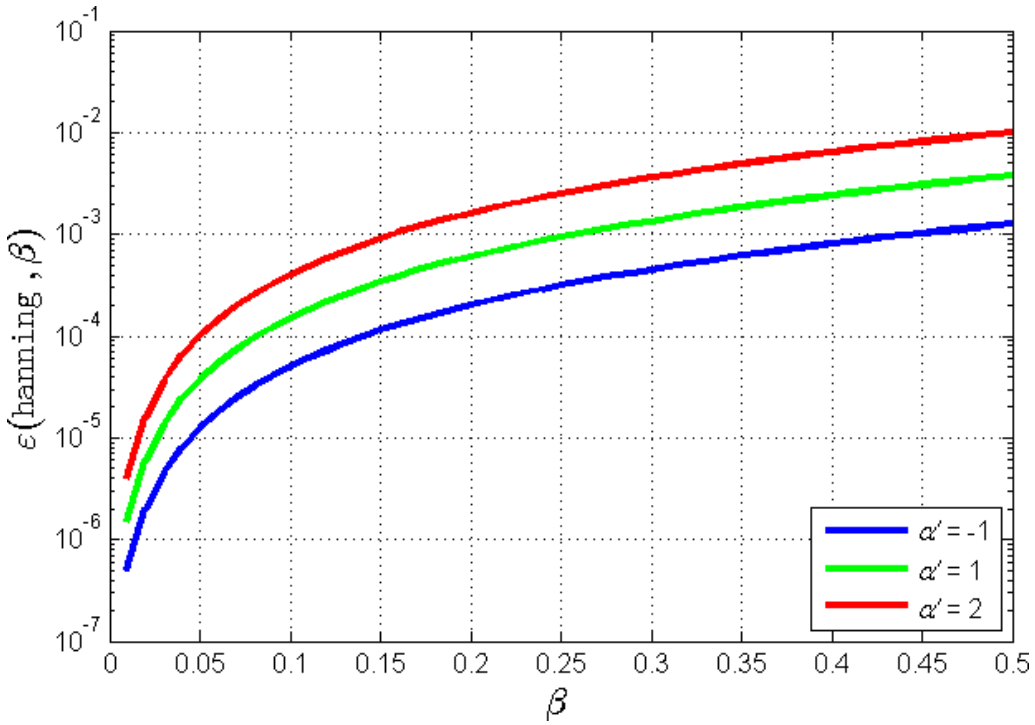

Figure 23. Narrow-band approximation relative error in Equation (52) numerically evaluated as a function of fractional bandwidth for a Hanning window.

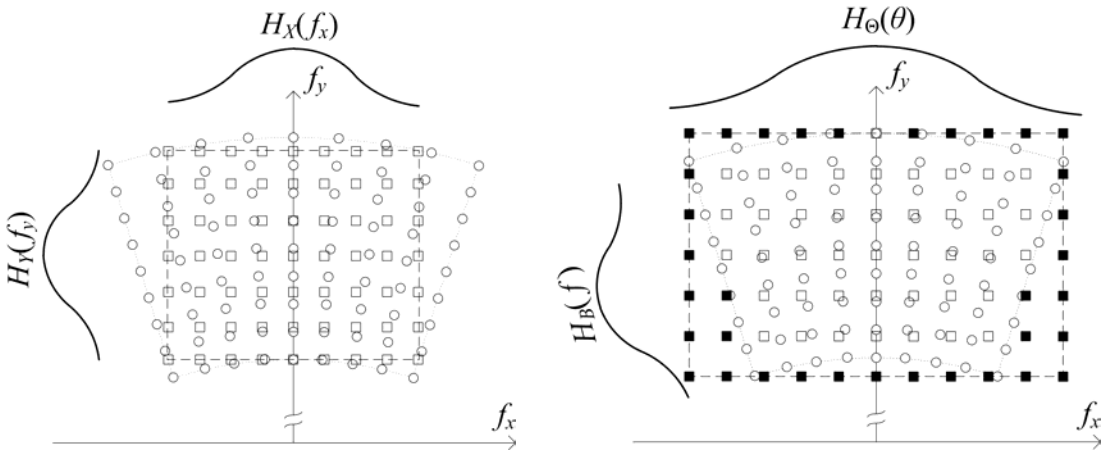

(a) Inscribed rectangle with rectangular windows

(b) Circumscribed rectangle with polar windows

Figure 24. Polar reformatting examples. Circles are the original samples in polar coordinates, and squares are the interpolated samples in rectangular coordinates. The black squares are assigned a value of zero.

rectangular windows, the sample density and weighting are uniform as shown in Figure 24(a). Here, the circles represent the original samples in polar coordinates and the squares are interpolated to be uniformly sampled in rectangular coordinates. As a result, the removal of the Jacobian causes the order of the exponent to reduce from $\alpha' + 2$ to α' for Equations (43) through (61).

Alternately, for the case of polar windows and a circumscribed rectangle, the weighting and zero-padding around the original annulus varies with frequency, as shown in Figure 24(b). Here, the black squares are assigned a value of zero. As a result, a Jacobian-like weighting of the phase history persists even after the Jacobian has been removed. Therefore, the order of the exponent from earlier discussions will remain unchanged due to the polar weighting of the samples.

For hybrids of the two schemes above, the exponent will need to be adjusted according to the effective weighting caused by the resulting sample densities. The polar reformatting algorithm is discussed at length in References [24] and [76].

5.1.3.1 Iterative Curve Fitting Algorithm.

For the case of two subimages, the frequency parameter is easily obtained from the measured subimage pixel intensities using Equation (47). However, for the case of more than two subimages, there are more than two subimage pixel intensity measurements. In this case, frequency parameter estimation requires curve fitting of the measurements to the set of normalized, ideal curves expected for a given α'. Typically, no truth data exists for these measurements; so any attempt to normalize the measurements creates an overdetermined system of equations. The iterative curve fitting algorithm developed in this section solves the overdetermined system of equations using a gradient decent technique [120, 10]. It assumes that there are I subimages for the jth subaperture.

Using the preselected subband center frequencies, a normalized frequency vector is defined as

$$\mathbf{f}(\alpha') = \frac{\left[(f_{c1})^{\alpha'+2}, (f_{c2})^{\alpha'+2}, ..., (f_{cI})^{\alpha'+2}\right]^T}{(f_c)^{\alpha'+2}}, \tag{62}$$

where ^{T} indicates the transpose and f_c is the center frequency of the full bandwidth, B. This vector can be interpreted as defining the normalized values (or curves) that a set of ideal, normalized intensity measurements will assume for a given α'. Similarly, an observation vector of the pixel intensities in each subimage is defined as

$$\boldsymbol{\sigma} = \left[|\tilde{g}_{1j}(m_q, n_q)|^2, |\tilde{g}_{2j}(m_q, n_q)|^2, ..., |\tilde{g}_{Ij}(m_q, n_q)|^2\right]^T. \tag{63}$$

Typically, no truth data exists, and so the correct normalization factor, ν, is unknown *a priori*. Therefore, there exists an overdetermined linear system defined as $\boldsymbol{\sigma}/\nu = \mathbf{f}(\alpha')$. In response, the iterative curve fitting algorithm obtains an estimate of α' using a greedy search method that continually reduces the total least squares error of the optimal normalization factor. This can be interpreted as adjusting α' to find the best possible fit to the family of curves defined by $\mathbf{f}(\alpha')$.

Beginning with Equation (47), the algorithm assigns the initial value

$$\alpha'_1 = \frac{\log\left(\frac{|\tilde{g}_{1j}(m_q, n_q)|^2}{|\tilde{g}_{Ij}(m_q, n_q)|^2}\right)}{\log\left(\frac{f_{c1}}{f_{cI}}\right)} - 2, \tag{64}$$

where the subscript on α' indicates the current iteration of the algorithm. In each iteration, the optimal normalization factor will minimize the norm of the residual expressed as $||\boldsymbol{\sigma}/\nu - \mathbf{f}(\alpha')||_2$. This is determined by setting the derivative of the square of the norm of the residual to zero [10, 120]. Thus, the optimal normalization

factor for the kth iteration is

$$\hat{\nu}_k = \frac{(\boldsymbol{\sigma}^T \boldsymbol{\sigma})}{\boldsymbol{\sigma}^T \mathbf{f}(\alpha'_k)}, \tag{65}$$

where the $\hat{}$ symbol indicates that this is an estimate of the normalization factor. This estimate may be refined by additional iterations of the curve fitting algorithm.

Next, the frequency parameter is adjusted by a scaled version of the norm of the residual expressed as

$$\delta_k = (0.95)^k ||\boldsymbol{\sigma}/\hat{\nu}_k - \mathbf{f}(\alpha'_k)||_2, \tag{66}$$

where the factor $(0.95)^k$ has a dampening effect that ensures convergence of the algorithm. This factor was selected experimentally; although any value less than unity will suffice, where higher values can cause a slower convergence rate and lower values can cause convergence to a local minima. The next value for α' is chosen via a greedy search method to obtain the smallest norm of the residual. This is expressed as

$$\alpha'_{k+1} = \begin{cases} \alpha'_k + \delta_k, & ||\boldsymbol{\sigma}/\hat{\nu}_k - \mathbf{f}(\alpha'_k + \delta_k)||_2 < ||\boldsymbol{\sigma}/\hat{\nu}_k - \mathbf{f}(\alpha'_k - \delta_k)||_2 \\ \alpha'_k - \delta_k, & \text{otherwise} \end{cases} \tag{67}$$

The algorithm iteratively adjusts α' until reaching a prescribed amount of precision expressed as $\delta_K < 0.01$, where K is the total number of iterations. At this point, the estimate of the frequency parameter is finalized as $\alpha' = \alpha'_{K+1}$. All experimental results contained in this dissertation used the exact procedure and prescribed values described above.

An example of the curve fitting algorithm for the stable peak at pixel (1,3) in Equation (42) of Section 5.1.1 is as follows. The observation vector is

$$\boldsymbol{\sigma} = [17, 18, 20]^T, \tag{68}$$

and given subband center frequencies of 9.25 GHz, 9.5 GHz, and 9.75 Ghz, the nor-

malized frequency vector is

$$\mathbf{f}(\alpha') = \frac{\left[9.25^{\alpha'+2}, 9.5^{\alpha'+2}, 9.75^{\alpha'+2}\right]^T}{9.5^{\alpha'+2}}. \tag{69}$$

The initial value for α' is given by

$$\alpha'_1 = \frac{\log\left(\frac{17}{20}\right)}{\log\left(\frac{9.25}{9.75}\right)} - 2 = 1.0871, \tag{70}$$

and the initial optimal normalization factor is given by

$$\hat{\nu}_1 = \frac{(\boldsymbol{\sigma}^T\boldsymbol{\sigma})}{\boldsymbol{\sigma}^T\mathbf{f}(\alpha'_1)} = 18.3095, \tag{71}$$

The adjustment to α' for this iteration is

$$\delta_1 = (0.95)^1||\boldsymbol{\sigma}/\hat{\nu}_1 - \mathbf{f}(\alpha'_1)||_2 = 0.0195. \tag{72}$$

Because $\delta_1 > 0.01$, another iteration is required. The adjustment to α' is

$$\alpha'_2 = \alpha'_1 + \delta_1 = 1.1066, \tag{73}$$

because

$$||\boldsymbol{\sigma}/\hat{\nu}_1 - \mathbf{f}(\alpha'_1 + \delta_1)||_2 = 0.0205 < ||\boldsymbol{\sigma}/\hat{\nu}_1 - \mathbf{f}(\alpha'_1 - \delta_1)||_2 = 0.0206 \tag{74}$$

The following concludes the curve fitting process:

$$\begin{gathered}
\hat{\nu}_2 = \frac{(\boldsymbol{\sigma}^T\boldsymbol{\sigma})}{\boldsymbol{\sigma}^T\mathbf{f}(\alpha_2')} = 18.3086, \\
\delta_2 = (0.95)^2||\boldsymbol{\sigma}/\hat{\nu}_0 - \mathbf{f}(\alpha_1')||_2 = 0.0185. \\
\alpha_3' = \alpha_2' + \delta_2 = 1.1251 \\
\alpha_4' = \alpha_3' + \delta_3 = 1.1426 \\
\alpha_5' = \alpha_4' - \delta_4 = 1.1260 \\
\alpha_6' = \alpha_5' + \delta_5 = 1.1418 \\
\alpha_7' = \alpha_6' - \delta_6 = 1.1267 \\
\vdots \\
\alpha_{16}' = \alpha_{15}' + \delta_{15} = 1.1292 + 0.0095 = 1.1387 \\
\delta_{15} < 0.01 \longrightarrow \alpha' = \alpha_{16}' = 1.14
\end{gathered} \tag{75}$$

An alternate example for the stable peak at pixel (3,2) in Equation (42) of Section 5.1.1 is as follows. The observation vector is

$$\boldsymbol{\sigma} = [10, 20, 19]^T, \tag{76}$$

and the initial value for α' is given by

$$\alpha_1' = \frac{\log\left(\frac{10}{19}\right)}{\log\left(\frac{9.25}{9.75}\right)} - 2 = 10.1924. \tag{77}$$

Note that $\alpha' = 10.1924$ is far outside the expected range for ideal frequency parameters. Using Table 5 of Section 3.2 as a guide, the ideal range is $\alpha' \in [-2, 2]$. As a result, the SPLIT algorithm rejects this pixel as non-canonical by halting the curve fitting algorithm and reassigning it a value of '0' in Equation (42) of Section 5.1.1.

In summary, the SPLIT algorithm requires that a subimage peak meet two criteria before extracting the frequency parameter. First, the peak must be stable, and sec-

ond, it must have a frequency parameter that is within or nearby the expected range for canonical scatterers. For the experimental results contained in this dissertation the estimated frequency parameter was required to be within the prescribed ranges of $\alpha'_1 \in [-6, 6]$ and $\alpha'_{K+1} \in [-4, 4]$.

5.1.4 Polarimetric Parameter Estimation.

The Krogager scattering matrix parameters are estimated from fully-polarized SAR data. This requires the availability of at least three phase histories, two co-polarization phase histories (HH and VV) and one cross-polarization phase history (HV or VH). The Krogager parameters were introduced earlier and discussed at length in Sections 2.2.3 and 2.3.3.

The Krogager parameters, κ_o and κ_e, for a subimage pixel having a stable peak are easily obtained by a coherent summation of the pixel values from the polarization-diverse subimages. The parameters represent the proportion of odd-bounce and even-bounce scattering in each pixel of the subimage, where it is convenient to define the proportion of helical scattering as $\kappa_h = 1 - \kappa_o - \kappa_e$.

In general, it has been noted that the polarimetric parameters of canonical scatterers can be estimated with greater accuracy than the other parameters. For this reason, the latest variant of the canonical scatterer classifier developed at The Ohio State University estimates canonical scatterer parameters from an image segment using a tiered approach, rather than a joint estimation approach. Because estimates of the polarization parameters are assumed to have the highest statistical confidence, these are estimated first, so as to restrict the possible values of the other parameters in subsequent tiers of the estimation scheme [73].

Deference to the polarimetric parameters is also adopted in this dissertation. The assumption is that the frequency parameter, α', has a much higher variance than

the Krogager parameters and is much more sensitive to modeling error, signal noise, and clutter. Because of this assumption, some ambiguities in the feature space are resolved by favoring instances of strong polarimetric response. For example, according to Table 5 from Section 3.2, the ideal feature vector for a horizontal cylinder is $\mathbf{w}_a = [\alpha', \kappa_o, \kappa_e] = [-1, 1, 0]$, while the ideal feature vector for a horizontal wire is $\mathbf{w}_b = [-2, 0.5, 0.5]$.

Consider the case of an extracted feature vector, $\mathbf{v} = [-2, 1, 0]$, where the Euclidean norms are $||\mathbf{w}_a - \mathbf{v}||_2 = 1$ and $||\mathbf{w}_b - \mathbf{v}||_2 = 0.707$. Clearly the norm is smaller for the horizontal wire; however, 'horizontal cylinder' is the best classification decision because both norms are large and the polarimetric response better matches that of the horizontal cylinder. In this way, the concept of polarimetric preference will impact the partitioning of the feature space for the SPLIT algorithm, as described later in Section 5.3.

5.2 Feature Vector Summation

The SPLIT algorithm extracts the frequency parameter from each co-polarization channel. The result is a single pixel having two estimates of the frequency parameter, α', when both HH and VV polarizations are available. In addition, the SPLIT algorithm extracts the polarization parameters from each subimage. This results in a single pixel having I estimates of the polarimetric parameters, $[\kappa_o, \kappa_e]$. Finally, the SPLIT algorithm extracts frequency and polarimetric features for each subaperture. Therefore, it is possible for the same pixel to be assigned multiple feature vectors, each extracted from a different subaperture. In these instances, the feature vectors for a single pixel are combined using a weighted average. Recall that pixels failing the canonical scatterer criteria of the SPLIT algorithm are assigned a feature vector weight of zero.

For the case of both HH and VV polarizations, the frequency parameter is equal to the weighted average

$$\alpha'_j = \frac{\sum_p \sigma_{jp} \alpha'_{jp}}{\sum_p \sigma_{jp}}, \tag{78}$$

where $\sigma_{jp} = \min_i\{|\tilde{g}_{ijp}(m_q, n_q)|^2\}$ is the minimum subimage pixel intensity for a given subaperture and polarization.

Likewise, the polarimetric parameters are equal the to weighted vector sum

$$[\kappa_o, \kappa_e]_j = \frac{\sum_i \sigma_{ij} [\kappa_o, \kappa_e]_{ij}}{\sum_i \sigma_{ij}}, \tag{79}$$

where $\sigma_{ij} = \min_p\{|\tilde{g}_{ijp}(m_q, n_q)|^2\}$ is the minimum subimage pixel intensity for a given subband and subaperture.

Finally, referring to Equation (41), the feature vector for a single pixel observed at multiple subapertures is equal to the weighted vector sum

$$\mathbf{v}(m_q, n_q) = \frac{\sum_j \sigma_j \mathbf{v}_j(m_q, n_q)}{\sum_j \sigma_j}, \tag{80}$$

where $\sigma_j = \min_i\{|\tilde{g}_{ij}(m_q, n_q)|^2\}$ is the minimum subimage pixel intensity for a given subaperture. This vector is referred to as the average feature vector.

An example of cross-aperture feature vector summation is as follows. Consider

the 4×4 feature vector arrays for subapertures $j = 1$ and $j = 2$ given as

$$\mathbf{V}_1 = \begin{bmatrix} \mathbf{0} & \mathbf{0} & \mathbf{0} & \mathbf{0} \\ \mathbf{0} & \mathbf{0} & \mathbf{0} & \mathbf{0} \\ 17[1.14, 0.22, 0.67] & \mathbf{0} & \mathbf{0} & \mathbf{0} \\ \mathbf{0} & \mathbf{0} & \mathbf{0} & \mathbf{0} \end{bmatrix}, \tag{81}$$

$$\mathbf{V}_2 = \begin{bmatrix} \mathbf{0} & \mathbf{0} & 42[1.79, 0.82, 0.11] & \mathbf{0} \\ \mathbf{0} & \mathbf{0} & \mathbf{0} & \mathbf{0} \\ 14[0.99, 0.25, 0.58] & \mathbf{0} & \mathbf{0} & \mathbf{0} \\ \mathbf{0} & \mathbf{0} & \mathbf{0} & \mathbf{0} \end{bmatrix}, \tag{82}$$

where $\mathbf{0}$ is the zero vector. Note that the feature vector array in Equation (81) is derived from the earlier examples in Equations (42) and (75). The weighted vector sum from Equation (80) computed for each pixel results in an array of average feature vectors expressed as

$$\mathbf{V} = \begin{bmatrix} \mathbf{0} & \mathbf{0} & [1.79, 0.82, 0.11] & \mathbf{0} \\ \mathbf{0} & \mathbf{0} & \mathbf{0} & \mathbf{0} \\ [1.07, 0.23, 0.63] & \mathbf{0} & \mathbf{0} & \mathbf{0} \\ \mathbf{0} & \mathbf{0} & \mathbf{0} & \mathbf{0} \end{bmatrix}, \tag{83}$$

where the pixels with non-canonical scattering have weights of zero and contribute nothing to the vector sum.

5.3 Canonical Scatterer Classification

The feature space for canonical scatterers can be partitioned using the ideal feature vectors in Table 5. However, these do not uniformly fill an entire Euclidean

feature space. Therefore, additional ideal feature vectors are added with deference to the polarimetric parameters, as described earlier in Section 5.1.4. First, the helical scatterer class is assigned five ideal feature vectors, $[-2, 0, 0]$, $[-1, 0, 0]$, $[0, 0, 0]$, $[1, 0, 0]$, and $[2, 0, 0]$. The assumption is that helical scattering can be associated with any value of α'. Next, the dihedral$_0$ scatterer class is assigned three ideal feature vectors, $[0, 0, 1]$, $[-1, 0, 1]$, and $[-2, 0, 1]$. Last, the cylinder$_0$ scatterer class is assigned two ideal feature vectors, $[-1, 1, 0]$ and $[-2, 1, 0]$.

The result is a set of seventeen ideal feature vectors, $\mathcal{W}$, assigned within a set of ten scatterer classes, $\mathcal{C}$. Scatterer classification is accomplished, pixel-by-pixel, by comparing each non-zero feature vector in the array of average feature vectors, $\mathbf{V}$, to the set of ideal feature vectors, $\mathcal{W}$. The classification decision can be accomplished using a likelihood ratio test informed by the statistical properties of each class and parameter, if available. However, for illustrative purposes, a simple a least squares classifier is preferred for demonstrating the SPLIT algorithm. A least squares classifier assumes uniform costs for misclassification and equal prior probabilities of each class. The least squares classifier and an associated, non-statistical measure of fitness is presented in this section and used throughout the remainder of this dissertation.

5.3.1 Least Squares Classifier.

For least squares classification, each non-zero average feature vector is compared to the set of seventeen ideal feature vectors, $\mathcal{W}$, using the Euclidean norm. Hence, each subimage pixel is declared a member of the class associated with the ideal feature vector for which the Euclidean norm is a minimum. The feature vector decision is succinctly represented as

$$d = \underset{k}{\operatorname{argmin}} \, ||\mathcal{W}_k - \mathbf{v}||_2, \tag{84}$$

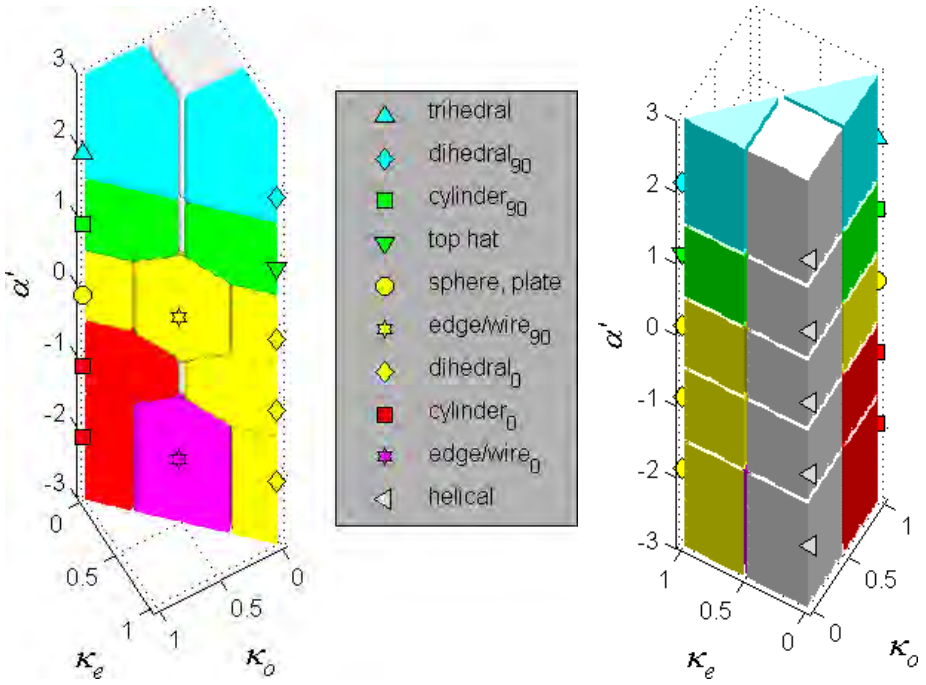

Figure 25. Feature space partitioned into scatterer classes according to a least squares classifier.

where $k \in \{1, 2, ..., 17\}$ provides an ordinal list of the ideal feature vectors and d is the index of the feature vector leading to the smallest norm in Equation (84). Hence, Equation (84) divides the feature space into seventeen regions according to a least squares "best fit" for the ideal canonical scatterers, as shown in Figure 25.

Finally, the scatterer classification decision is expressed using a scatterer classification operator, $\mathcal{S}$, as

$$\mathcal{S}\{\mathbf{v}\} = \mathcal{C}(\mathcal{W}_d), \tag{85}$$

where the class associated with ideal feature vector $\mathcal{W}_d$ determines the assigned class. For example, least squares classification using the array of average feature vectors in

Equation (83) results in

$$\mathbf{V} = \begin{bmatrix} - & - & \text{trihedral} & - \\ - & - & - & - \\ \text{tophat} & - & - & - \\ - & - & - & - \end{bmatrix}. \tag{86}$$

This is due to the fact that the average feature vectors $\mathbf{v}(3,1) = [1.79, 0.82, 0.11]$ and $\mathbf{v}(1,3) = [1.07, 0.23, 0.63]$ are closest to the ideal feature vectors $[2,1,0]$ and $[1,0,1]$, which in turn, are associated with the trihedral class and top hat class, respectively.

5.3.2 Measure of Fitness.

Some average feature vectors may reside near a boundary between two regions. Therefore, it is instructive to provide an additional measure of fitness. The measure of fitness is defined as

$$\gamma = 1 - \frac{||\mathcal{W}_d - \mathbf{v}||_2}{\min\limits_{\mathcal{W}_k \notin \mathcal{C}(\mathcal{W}_d)} ||\mathcal{W}_k - \mathbf{v}||_2}, \tag{87}$$

where the denominator is the Euclidean norm for the next best fit for ideal feature vectors not associated with the declared class, $\mathcal{C}(\mathcal{W}_d)$. Using a ratio of Euclidean norms causes the measure of fitness to be in the range $\gamma \in [0,1]$.

For example, beginning with Equation (83), the measures of fitness are

$$\gamma(1,3) = 1 - \frac{||[1,0,1] - [1.07, 0.23, 0.63]||_2}{||[1,0,0] - [1.07, 0.23, 0.63]||_2} = 0.35 \tag{88}$$

and

$$\gamma(3,1) = 1 - \frac{||[2,1,0] - [1.79, 0.82, 0.11]||_2}{||[1,1,0] - [1.79, 0.82, 0.11]||_2} = 0.69, \tag{89}$$

where the next best fits are a helical, $[1,0,0]$, and cylinder, $[1,1,0]$, respectively. Thus,

the array of measures of fitness for the example in Equation (83) is

$$\mathbf{\Gamma} = \begin{bmatrix} - & - & 0.69 & - \\ - & - & - & - \\ 0.35 & - & - & - \\ - & - & - & - \end{bmatrix}, \tag{90}$$

where Equations (86) and (90) represent example classification results produced by the SPLIT algorithm.

5.4 Experimental Results

This section presents experimental results using measured and simulated SAR data. The complexity of the scene increases with each experiment. First, isolated canonical scatterers are classified to demonstrate and validate the usefulness of the multi-peak model for scatterer classification. Then, inverse SAR (ISAR) radar measurements of a smooth metallic body, called D2, are evaluated. Even though the measurements are not fully-polarimetric, the D2 provides an excellent case study for modeling a simple object as a compilation of canonical scatterers. Next, simulated data of civilian vehicles provide a more challenging scenario for scatterer classification. These illustrate both the benefits and limitations of scatterer classification by phase domain decomposition for complex objects. Finally, the Gotcha multipass data, featuring measured SAR data of a calibration targets, is examined. Because the Gotcha data has only moderate bandwidth, poor coherency between pulses, and high clutter energy, the classification results are marginal, as expected.

Arrays similar to those in Equations (86) and (90) are used to create an overlay to display the classification results onto the SAR image. The classification results are displayed using the symbols and colors for the ideal feature vectors in Figure 25,

while the measure of fitness is displayed by symbol size. Note that the helical scatterer is given a neutral color in the legend, but each of the five ideal feature vectors will actually give a unique color in the overlay for each value of α'. The colors in ascending order are magenta ($\alpha' = -2$), red ($\alpha' = -1$), yellow ($\alpha' = 0$), green ($\alpha' = 1$), and cyan ($\alpha' = 2$).

The images presented in this Section were produced by integrating the SPLIT-based scatterer classification algorithm with a fast convolution backprojection imaging algorithm as described in the next chapter. The integrated algorithm employs domain decomposition to produce coarse-resolution subimages for subsequent analysis by the scatterer classifier. Then it interpolates, weights, and sums the subimages to form a fine-resolution SAR image.

5.4.1 Accuracy of the Multi-peak Model.

It is desirable to succinctly present the accuracy of the new multi-peak model for all canonical scatterer types and at several non-zero orientation angles. In addition, it is helpful to illustrate how the multi-peak model in Equation (37) is useful for classification of canonical scatterers in SAR imagery. Consequently, this section illustrates the applicability of the model to scatterer classification while reiterating some of the benefits and limitations of the model which were discussed previously.

Because frequency parameter estimation in Equation (47) uses the new multi-peak model parameterized by α', it is instructive to re-evaluate the applicability of the multi-peak model in Equation (37) for use with the SPLIT algorithm. From Equation (31) and assuming $\theta_c = 0$ without loss of generality, the ratio of integrated,

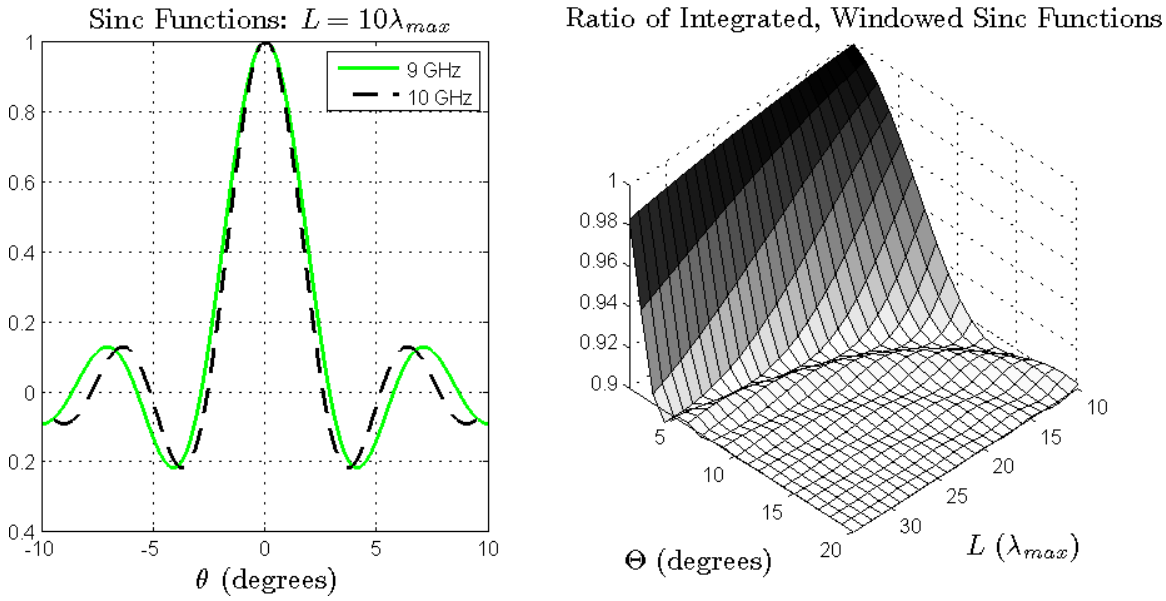

Figure 26. Under wide-angle conditions, the ratio of integrated, windowed sinc functions equals the inverse ratio of sinc frequencies. Here, $f_1 = 10$-Ghz, $f_2 = 9$-GHz, and $\theta_0 = 0°$.

windowed sinc functions must satisfy the relationship

$$\frac{\int_{-\pi}^{\pi} H_{\Theta}(\theta)\,\mathrm{sinc}\left(\frac{2}{c}f_1 L\sin(\theta-\theta_0)\right)d\theta}{\int_{-\pi}^{\pi} H_{\Theta}(\theta)\,\mathrm{sinc}\left(\frac{2}{c}f_2 L\sin(\theta-\theta_0)\right)d\theta} = \frac{f_2}{f_1}, \tag{91}$$

where $\Theta > \Theta_{min}$ and the minimum aperture width, Θ_{min}, can be determined by numerical integration. Numerical results for Equation (91) using a Hanning window are shown in Figure 26, where $f_1 = 10$ GHz and $f_2 = 9$ GHz. The graph on the right indicates that for $\Theta \gtrsim 10°$ the relationship in Equation (91) is satisfied, where $f_2/f_1 = 0.9$. Earlier analyses indicate that this relationship holds for varying frequencies and orientations angles as long as the aperture width is restricted to $\Theta \gtrsim 10°$ and the window function in azimuth is tapered.

Simulated phase histories were produced for fifteen canonical scatterers listed in Table 8 using canonical scattering models from Reference [75]. This data set contains

Table 8. Simulated Canonical Scatterer Specifications.

Index	Description	Height (m)	Width (m)	Radius (m)	L (m)	τ (deg)
(A)	square trihedral	1	1	n/a	0	0
(B)	dihedral_{90}	1	1	n/a	0	90
(C)	cylinder_{90}	1	n/a	0.5	0	90
(D)	top hat	1	n/a	0.5	0	0
(E)	point scatterer	n/a	n/a	n/a	0	n/a
(F)	sphere	n/a	n/a	0.5	0	n/a
(G)	plate, 15λ	1	0.5	n/a	0.5	0
(H)	plate, 30λ	1	1	n/a	1	0
(I)	plate, 60λ	1	2	n/a	2	0
(J)	$\text{dihedral}_0, 15\lambda$	1	0.5	n/a	0.5	0
(K)	$\text{dihedral}_0, 30\lambda$	1	1	n/a	1	0
(L)	$\text{dihedral}_0, 60\lambda$	1	2	n/a	2	0
(M)	$\text{cylinder}_0, 15\lambda$	n/a	0.5	0.5	0.5	0
(N)	$\text{cylinder}_0, 30\lambda$	n/a	1	0.5	1	0
(O)	$\text{cylinder}_0, 60\lambda$	n/a	2	0.5	2	0

Table 9. Radar Measurement Data Parameters.

Parameter	Value
Polarizations	HH, VV, VH
LFM Frequencies	8.6061 : 0.0081 : 10.5939 GHz
Azimuth	-5.0000 : 0.0859 : 4.9695 degrees
Elevation Angle	45 degrees

specific examples of the ideal canonical scatters in Table 5, to include six different point scatterers and three different distributed scatterers of varying lengths. The lengths were specifically chosen to illustrate the limitations of the high frequency approximation at X-band. The phase histories were simulated using a circular aperture according to the specifications in Table 9. Here, the azimuth angle is referenced counter-clockwise from the negative y-axis, and the frequency and azimuth are listed as `start:increment:end` values.

Classification accuracy is dependent upon model accuracy, bandwidth, and interference from neighboring canonical scatterers, clutter, and noise. However, in order

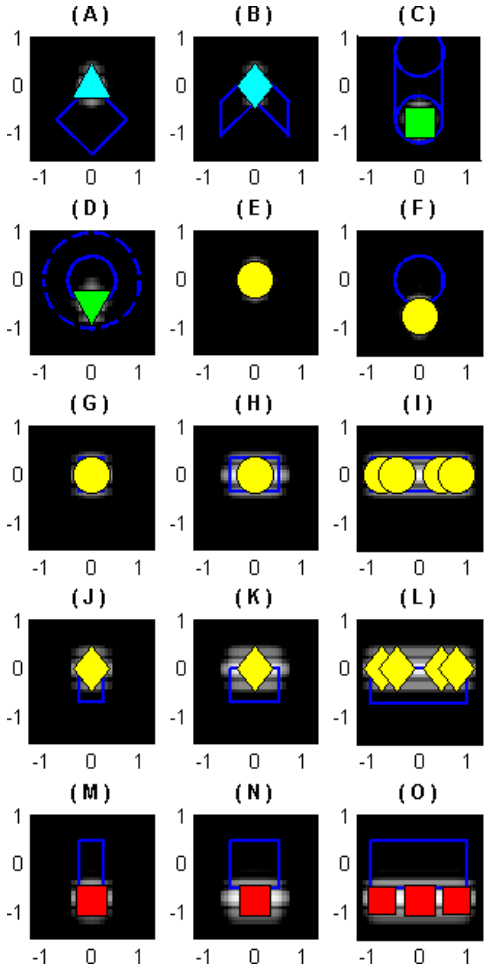

Figure 27. Classification results for $\Theta = 10°$. Scatterers (A) to (F) are point scatterers and (G) to (O) are distributed scatterers of varying lengths.

to isolate the effect of model accuracy on classification accuracy, the simulations are free of interference. The images and classification results below were produced using the integrated algorithm with $I = 3$ subbands. Also, the images are truncated to show only the top 45 dB of image intensity.

For the case of $\Theta = 10°$ shown in Figure 27, a single aperture is used to produce the classification results and images. Here, the classification results are annotated on the image using the symbology from Figure 25. For this case, all classification results are correct because the multi-peak model is accurate when the wide-angle condition is satisfied and all distributed scatterers are greater than ten wavelengths in length.

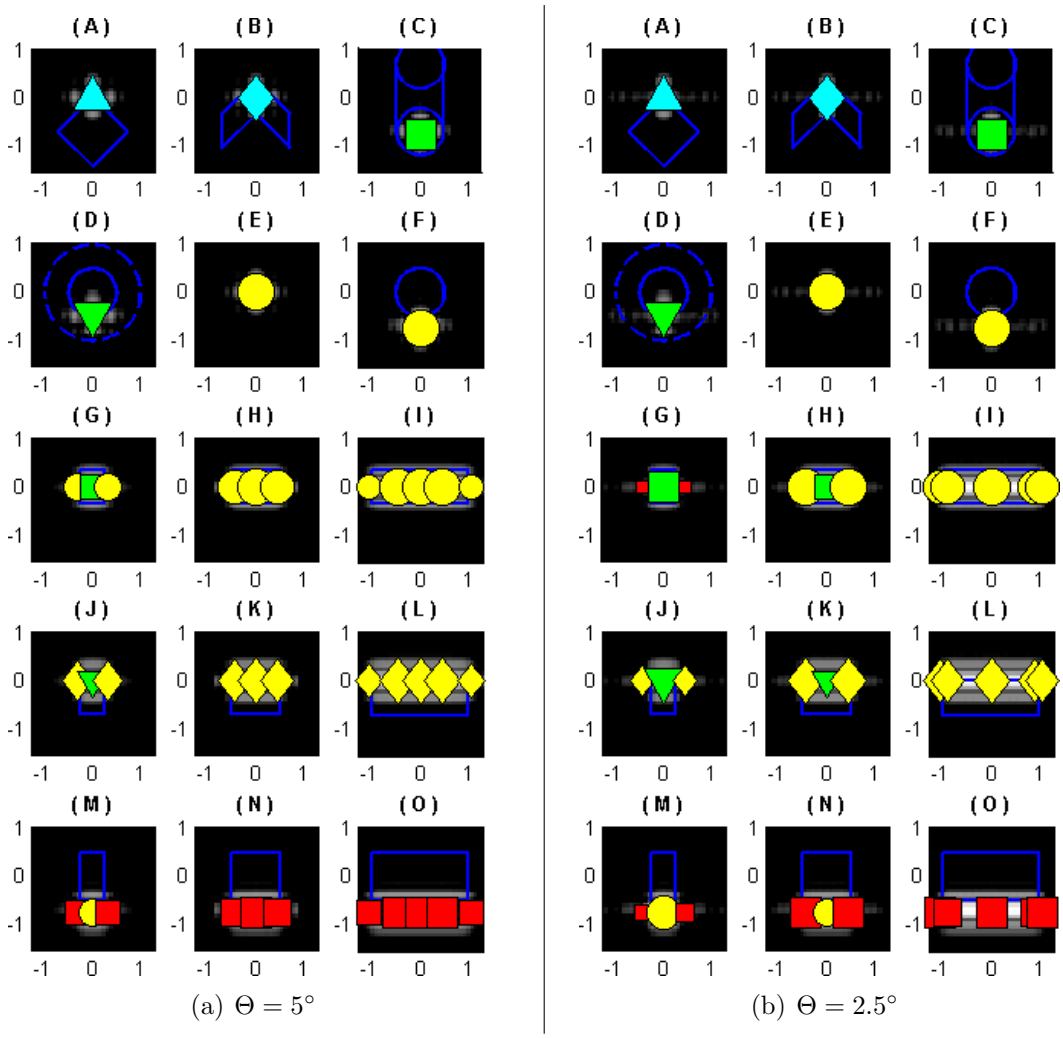

(a) $\Theta = 5°$ (b) $\Theta = 2.5°$

Figure 28. Classification results for narrow-angles. For the distributed scatterers, accuracy decreases as Θ or L decreases.

In this case, the longer distributed scatterers (I), (L) and (O), each produce a group of in-line peaks. The in-line peaks are a manifestation of Gibbs phenomenon due to the imaging operator, and illustrate a characteristic of distributed scatterers from which the multi-peak model derives its name.

For the case of $\Theta = 5°$ shown in Figure 28(a), three evenly spaced, overlapping subapertures were used to produce the classification results and images. In this case, the classification results are correct for all point scatterers (A) to (F) and for the longer distributed scatterers, as expected. Also as expected, the classification results

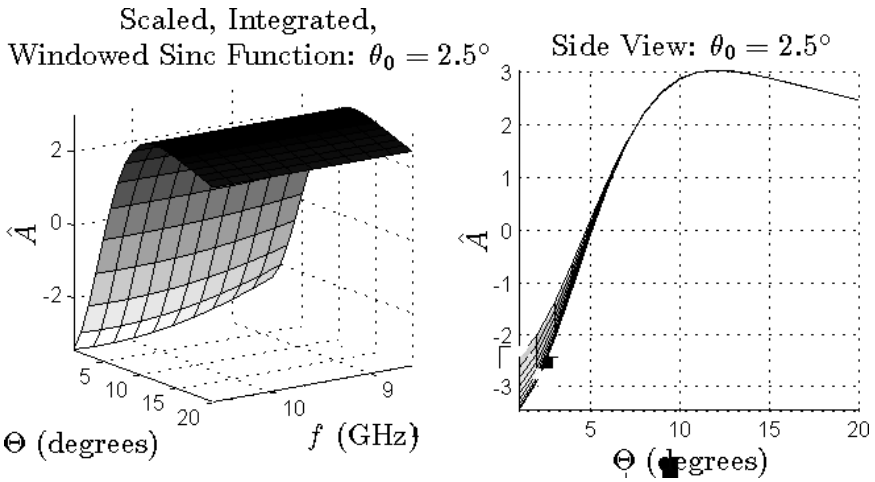

Figure 29. Numerical results for Eq. (31) where H_Θ is a Hanning function with region of support equal to Θ. The distributed scatterer is of length $L = 0.5$-meter.

are incorrect for the shortest distributed scatterers, (G), (J), and (M), because the accuracy of the new multi-peak model is degraded for the case of $\Theta = 5°$ and $L = 15\lambda$. These results were predicted by numerical analysis, where Figure 26 reveals that the model is only accurate when $L \lesssim 25\lambda$ for the case of $\Theta = 5°$. The two peaks which were correctly classified came from analysis of the subapertures at $\theta_0 = [-2.5, 2.5]$. It can be seen in Figure 29 that the model is valid at $\Theta = 5°$ because $\hat{A}$ is essentially independent of frequency for this case. However, the value at $\hat{A}$ is very small when $\Theta = 5°$, which results in low peak intensities. Low peak intensities are a well-known characteristic of long scatterers imaged at off-broadside aspects [83].

For the case of $\Theta = 2.5°$ shown in Figure 28(b), seven evenly spaced, overlapping subapertures were used to produce the classification results and images. In this case, the classification results are correct for all point scatterers (A) to (F) and for the longest distributed scatterers, as expected. Also as expected, the classification results are incorrect for the shorter distributed scatterers, (G), (H), (J), (K), (M), and (N), because the accuracy of the new multi-peak model has further degraded for this case. The reasons for this are analogous to the case of $\Theta = 5°$, and the results

Table 10. Peak Intensity Classification Results, $\Theta = 10°$.

Index	(x, y)		(x, y)		(x, y)		(x, y)		(x, y)	
θ_c	α'	σ	α'	σ	α'	σ	α'	σ	α'	σ
(A)	-		-		(0,0)		-		-	
0.0°	-	-	-	-	2.00	0 dB	-	-	-	-
(B)	-		-		(0,0)		-		-	
0.0°	-	-	-	-	2.00	0 dB	-	-	-	-
(C)	-		-		(0,-0.76)		-		-	
0.0°	-	-	-	-	0.97	0 dB	-	-	-	-
(D)	-		-		(0,-0.46)		-		-	
0.0°	-	-	-	-	1.00	0 dB	-	-	-	-
(E)	-		-		(0,0)		-		-	
0.0°	-	-	-	-	0.00	0 dB	-	-	-	-
(F)	-		-		(0,-0.76)		-		-	
0.0°	-	-	-	-	-0.02	0 dB	-	-	-	-
(G)	-		-		(0,0)		-		-	
0.0°	-	-	-	-	0.01	0 dB	-	-	-	-
(H)	-		-		(0,0)		-		-	
0.0°	-	-	-	-	0.01	0 dB	-	-	-	-
(I)	(-0.76,0)		(-0.46,0)		-		(0.46,0)		(0.76,0)	
0.0°	0.05	0 dB	-0.01	0 dB	-	-	-0.01	0 dB	-0.05	0 dB
(J)	-		-		(0,0)		-		-	
0.0°	-	-	-	-	0.01	0 dB	-	-	-	-
(K)	-		-		(0,0)		-		-	
0.0°	-	-	-	-	0.01	0 dB	-	-	-	-
(L)	(-0.76,0)		(-0.46,0)		-		(0.46,0)		(0.76,0)	
0.0°	0.05	0 dB	-0.01	0 dB	-	-	0.05	0 dB	-0.01	0 dB
(M)	-		-		(0,-0.76)		-		-	
0.0°	-	-	-	-	-0.98	0 dB	-	-	-	-
(N)	-		-		(0,-0.76)		-		-	
0.0°	-	-	-	-	-0.99	0 dB	-	-	-	-
(O)	(-0.76,-0.76)		-		(0,-0.76)		-		(0.76,-0.76)	
0.0°	-0.94	0 dB	-	-	-0.99	0 dB	-	-	-0.94	0 dB

are as expected based on Figure 26. Evidently, the model is accurate for $L = 60\lambda$ when $\Theta = 2.5°$, as can be seen by examining (I), (L), and (O).

If desired, the classification process for this experiment can be verified by examining the extracted frequency parameters provided in Tables 10, 11, and 12. All intensity values are normalized to the highest intensity sample for each scatterer, individually. The Krogager parameters are not listed, because the simulated data produced almost ideal Krogager values in each case.

In summary, all classification results, including incorrect classifications, were nicely predicted using the multi-peak model. The classification results were correct for the canonical point scatterers (A) to (F) and the longer distributed canonical scatterers

Table 11. Peak Intensity Classification Results, $\Theta = 5°$.

Index	(x, y)		(x, y)		(x, y)		(x, y)		(x, y)	
θ_c	α'	σ	α'	σ	α'	σ	α'	σ	α'	σ
(G)	-		(-0.31,0)		(0,0)		(0.31,0)		-	
−2.5°	-	-	-0.23	-36 dB	-	-	-0.23	-36 dB	-	-
0.0°	-	-	-	-	1.20	0 dB	-	-	-	-
2.5°	-	-	-0.22	-36 dB	-	-	-0.22	-36 dB	-	-
sum	-	-	-0.23	-30 dB	1.20	0 dB	-0.23	-30 dB	-	-
(H)	-		(-0.46,0)		(0,0)		(0.46,0)		-	
−2.5°	-	-	-0.12	-40 dB	-	-	-0.11	-40 dB	-	-
0.0°	-	-	-	-	-0.01	0 dB	-	-	-	-
2.5°	-	-	-0.12	-41 dB	-	-	-0.12	-41 dB	-	-
sum	-	-	-0.12	-34 dB	-0.01	0 dB	-0.12	-34 dB	-	-
(I)	(-1.07,0)		(-0.46,0)		(0,0)		(0.46,0)		(1.07,0)	
−2.5°	-0.28	-41 dB	-	-	-	-	-	-	-0.28	-41 dB
0.0°	-	-	-0.04	0 dB	0.00	0 dB	-0.04	0 dB	-	-
2.5°	-0.27	-42 dB	-	-	-	-	-	-	-0.26	-42 dB
sum	-0.27	-35 dB	-0.04	0 dB	0.00	0 dB	-0.04	0 dB	-0.27	-35 dB
(J)	-		(-0.31,0)		(0,0)		(0.31,0)		-	
−2.5°	-	-	-0.23	-36 dB	-	-	-0.23	-36 dB	-	-
0.0°	-	-	-	-	1.20	0 dB	-	-	-	-
2.5°	-	-	-0.21	-36 dB	-	-	-0.22	-36 dB	-	-
sum	-	-	-0.22	-30 dB	1.20	0 dB	-0.22	-30 dB	-	-
(K)	-		(-0.46,0)		(0,0)		(0.46,0)		-	
−2.5°	-	-	-0.11	-40 dB	-	-	-0.11	-40 dB	-	-
0.0°	-	-	-	-	-0.01	0 dB	-	-	-	-
2.5°	-	-	-0.11	-41 dB	-	-	-0.11	-41 dB	-	-
sum	-	-	-0.11	-34 dB	-0.01	0 dB	-0.11	-34 dB	-	-
(L)	(-1.07,0)		(-0.46,0)		(0,0)		(0.46,0)		(1.07,0)	
−2.5°	-0.27	-41 dB	-	-	-	-	-	-	-0.27	-41 dB
0.0°	-	-	-0.04	0 dB	0.00	0 dB	-0.04	0 dB	-	-
2.5°	-0.26	-42 dB	-	-	-	-	-	-	-0.26	-42 dB
sum	-0.27	-35 dB	-0.04	0 dB	0.00	0 dB	-0.04	0 dB	-0.27	-35 dB
(M)	-		(-0.31,-0.76)		(0,-0.76)		(0.31,-0.76)		-	
−2.5°	-	-	-1.23	-37 dB	-	-	-1.21	-37 dB	-	-
0.0°	-	-	-	-	0.21	0 dB	-	-	-	-
2.5°	-	-	-1.19	-37 dB	-	-	-1.21	-37 dB	-	-
sum	-	-	-1.21	-31 dB	0.21	0 dB	-1.21	-31 dB	-	-
(N)	-		(-0.46,-0.76)		(0,-0.76)		(0.46,-0.76)		-	
−2.5°	-	-	-1.08	-40 dB	-	-	-1.09	-40 dB	-	-
0.0°	-	-	-	-	-1.00	0 dB	-	-	-	-
2.5°	-	-	-1.10	-41 dB	-	-	-1.08	-41 dB	-	-
sum	-	-	-1.09	-34 dB	-1.00	0 dB	-1.09	-34 dB	-	-
(O)	(-1.07,-0.76)		(-0.46,-0.76)		(0,-0.76)		(0.46,-0.76)		(1.07,-0.76)	
−2.5°	-1.26	-41 dB	-	-	-	-	-	-	-1.22	-41 dB
0.0°	-	-	-1.03	0 dB	-0.99	0 dB	-1.03	0 dB	-	-
2.5°	-1.21	-42 dB	-	-	-	-	-	-	-1.24	-42 dB
sum	-1.23	-35 dB	-1.03	0 dB	-0.99	0 dB	-1.03	0 dB	-1.23	-35 dB

(I), (L), and (O), in every case. For the incorrect classifications, the experiment illustrates how model accuracy decreases gradually as Θ or L decreases. These results indicate that the multi-peak model can be used to classify distributed scatterers by comparing the peak intensities of subimages produced by phase history decomposition. However, the aperture should be large ($\Theta \gtrsim 10°$), particularly for distributed scatterers of shorter physical length.

Table 12. Peak Intensity Classification Results, $\Theta = 2.5°$.

Index	(x, y)		(x, y)		(x, y)		(x, y)		(x, y)	
θ_c	α'	σ	α'	σ	α'	σ	α'	σ	α'	σ
(G)	-		(-0.46,0)		(0,0)		(0.46,0)		-	
−3.8°	-	-	-	-	0.02	-67 dB	-	-	-	-
−2.5°	-	-	-0.44	-52 dB	-	-	-0.41	-52 dB	-	-
−1.3°	-	-	-	-	0.02	-13 dB	-	-	-	-
0.0°	-	-	-	-	1.78	-5 dB	-	-	-	-
1.3°	-	-	-	-	-0.02	-14 dB	-	-	-	-
2.5°	-	-	-0.71	-51 dB	-	-	-0.72	-51 dB	-	-
3.8°	-	-	-	-	0.37	-67 dB	-	-	-	-
sum	-	-	-0.58	-46 dB	1.05	0 dB	-0.57	-46 dB	-	-
(H)	-		(-0.46,0)		(0,0)		(0.46,0)		-	
−3.8°	-	-	-0.36	-80 dB	-	-	-	-	-	-
−2.5°	-	-	-0.22	-51 dB	-	-	-0.22	-51 dB	-	-
−1.3°	-	-	-0.04	-25 dB	-	-	-0.03	-25 dB	-	-
0.0°	-	-	-	-	1.20	0 dB	-	-	-	-
1.3°	-	-	-0.05	-26 dB	-	-	-0.05	-26 dB	-	-
2.5°	-	-	-0.24	-51 dB	-	-	-0.24	-51 dB	-	-
3.8°	-	-	-0.39	-80 dB	-	-	-0.39	-80 dB	-	-
sum	-	-	-0.05	-19 dB	1.20	0 dB	-0.05	-19 dB	-	-
(I)	(-1.07,0)		(-0.92,0)		(0,0)		(0.92,0)		(1.07,0)	
−3.8°	-	-	-	-	-	-	-	-	-0.14	-84 dB
−2.5°	-0.01	-55 dB	-	-	-	-	-	-	-0.01	-55 dB
−1.3°	-	-	-0.09	-30 dB	-2.54	-72 dB	-0.09	-30 dB	-	-
0.0°	-	-	-	-	-0.01	0 dB	-	-	-	-
1.3°	-0.10	-31 dB	-	-	-	-	-	-	-0.10	-31 dB
2.5°	-0.08	-55 dB	-	-	-	-	-	-	-0.08	-55 dB
3.8°	-0.12	-84 dB	-	-	-	-	-	-	-	-
sum	-0.10	-30 dB	-0.09	-30 dB	-0.01	0 dB	-0.09	-30 dB	-0.10	-30 dB
(J)	-		(-0.46,0)		(0,0)		(0.46,0)		-	
−3.8°	-	-	-	-	0.03	-67 dB	-	-	-	-
−2.5°	-	-	-0.43	-52 dB	-	-	-0.40	-52 dB	-	-
−1.3°	-	-	-	-	0.02	-13 dB	-	-	-	-
0.0°	-	-	-	-	1.78	-5 dB	-	-	-	-
1.3°	-	-	-	-	-0.02	-14 dB	-	-	-	-
2.5°	-	-	-0.70	-51 dB	-	-	-0.72	-51 dB	-	-
3.8°	-	-	-	-	0.37	-67 dB	-	-	-	-
sum	-	-	-0.57	-46 dB	1.05	0 dB	-0.56	-46 dB	-	-
(K)	-		(-0.46,0)		(0,0)		(0.46,0)		-	
−3.8°	-	-	-0.31	-80 dB	-	-	-	-	-	-
−2.5°	-	-	-0.22	-51 dB	-	-	-0.21	-51 dB	-	-
−1.3°	-	-	-0.04	-25 dB	-	-	-0.03	-25 dB	-	-
0.0°	-	-	-	-	1.20	0 dB	-	-	-	-
1.3°	-	-	-0.05	-26 dB	-	-	-0.05	-26 dB	-	-
2.5°	-	-	-0.23	-51 dB	-	-	-0.23	-51 dB	-	-
3.8°	-	-	-0.34	-80 dB	-	-	-0.35	-80 dB	-	-
sum	-	-	-0.05	-19 dB	1.20	0 dB	-0.05	-19 dB	-	-
(L)	(-1.07,0)		(-0.92,0)		(0,0)		(0.92,0)		(1.07,0)	
−3.8°	-	-	-	-	-	-	-	-	-0.11	-84 dB
−2.5°	-0.01	-55 dB	-	-	-	-	-	-	-0.01	-55 dB
−1.3°	-	-	-0.09	-30 dB	-2.54	-72 dB	-0.09	-30 dB	-	-
0.0°	-	-	-	-	-0.01	0 dB	-	-	-	-
1.3°	-0.10	-31 dB	-	-	-	-	-	-	-0.10	-31 dB
2.5°	-0.07	-55 dB	-	-	-	-	-	-	-0.07	-55 dB
3.8°	-0.08	-84 dB	-	-	-	-	-	-	-	-
sum	-0.10	-30 dB	-0.09	-30 dB	-0.01	0 dB	-0.09	-30 dB	-0.10	-30 dB
(M)	-		(-0.46,-0.76)		(0,-0.76)		(0.46,-0.76)		-	
−3.8°	-	-	-	-	-0.91	-67 dB	-	-	-	-
−2.5°	-	-	-1.35	-52 dB	-	-	-1.47	-52 dB	-	-
−1.3°	-	-	-	-	-0.97	-14 dB	-	-	-	-
0.0°	-	-	-	-	0.79	-4 dB	-	-	-	-
1.3°	-	-	-	-	-1.01	-15 dB	-	-	-	-
2.5°	-	-	-1.75	-52 dB	-	-	-1.66	-52 dB	-	-
3.8°	-	-	-	-	-0.58	-67 dB	-	-	-	-
sum	-	-	-1.55	-46 dB	0.10	0 dB	-1.57	-46 dB	-	-
(N)	-		(-0.46,-0.76)		(0,-0.76)		(0.46,-0.76)		-	
−3.8°	-	-	-	-	-	-	-1.37	-81 dB	-	-
−2.5°	-	-	-1.16	-52 dB	-	-	-1.21	-52 dB	-	-
−1.3°	-	-	-0.99	-26 dB	-	-	-1.02	-26 dB	-	-
0.0°	-	-	-	-	0.21	0 dB	-	-	-	-
1.3°	-	-	-1.04	-27 dB	-	-	-1.01	-27 dB	-	-
2.5°	-	-	-1.23	-51 dB	-	-	-1.18	-51 dB	-	-
3.8°	-	-	-1.41	-81 dB	-	-	-	-	-	-
sum	-	-	-1.03	-20 dB	0.21	0 dB	-1.02	-20 dB	-	-
(O)	(-1.07,-0.76)		(-0.92,-0.76)		(0,-0.76)		(0.92,-0.76)		(1.07,-0.76)	
−3.8°	-1.12	-84 dB	-	-	-	-	-1.17	-84 dB	-	-
−2.5°	-1.05	-55 dB	-	-	-	-	-	-	-0.01	-55 dB
−1.3°	-	-	-1.07	-30 dB	-3.47	-72 dB	-1.07	-30 dB	-	-
0.0°	-	-	-	-	-1.00	0 dB	-	-	-	-
1.3°	-	-	-1.08	-31 dB	-	-	-	-	-1.06	-31 dB
2.5°	-	-	-	-	-	-	-	-	-1.02	-55 dB
3.8°	-	-	-1.17	-84 dB	-	-	-	-	-1.09	-84 dB
sum	-1.05	-55 dB	-1.08	-24 dB	-1.00	0 dB	-1.07	-30 dB	-1.05	-31 dB

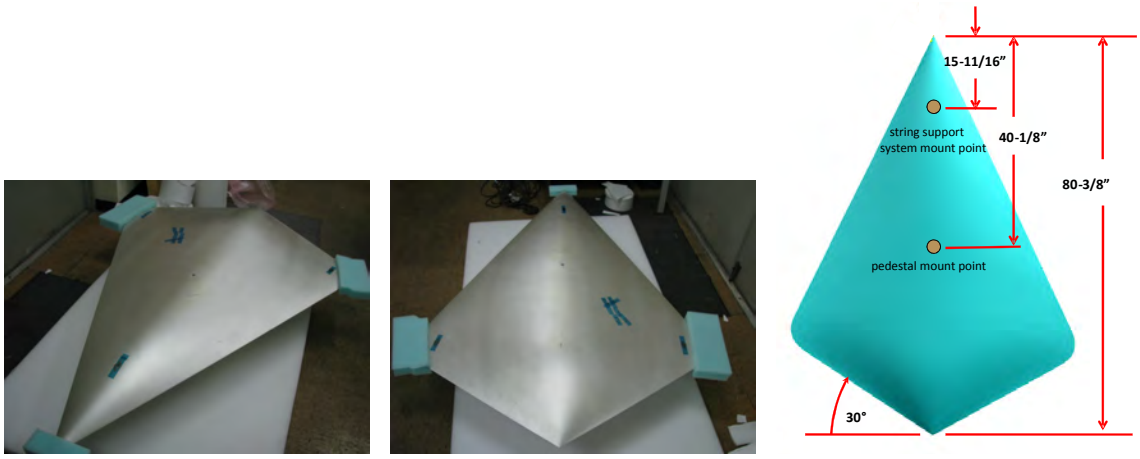

(a) Frontal aspect. (b) Rear aspect. (c) Dimensions.

Figure 30. D2 airframe [4].

5.4.2 D2 Measurements.

This section presents experimental results obtained from measurements of a smooth metallic body called D2. The measured data was obtained from the AFIT indoor RCS measurement range described in Appendix A. Photographs and dimensions of the D2 are provided in Figure 30, and a photo of the measurement configuration is provided in Figure 31. Additional information regarding D2 and its measured data can be found in Reference [4].

The parameters for an ISAR measurement are given in Table 13, and a 2D image overlaid with classification results combined from both HH and VV channels is shown in Figure 32. Note how the straight edges of the D2 are correctly classified as horizontal edges and how the D2-pedestal-D2 interactions are consistently classified as trihedrals (or horizontal dihedrals). These correct classifications occur in spite of the fact that these measurements are in the near field, which violates one of the assumptions of the multi-peak model.

The near field distortion creates an artificial curvature that may explain the 'cylinder' classifications along the back edge near ($x = 0.9$, $y = 0.1$) m in Figure 32. Like-

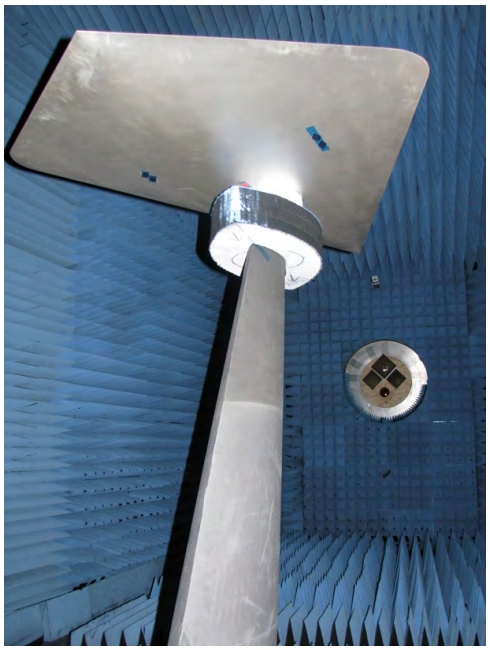

Figure 31. Photo of D2 airframe from a rear aspect [4]. The D2 is on the target pedestal at the AFIT Indoor RCS measurement range with the radar antennas shown in the background.

Table 13. Experimental Parameters for ISAR Measurements of D2.

Parameter	Value
Polarizations	VV and HH
LFM Frequencies (GHz)	$6.528 : 0.023 : 18.005$
Fractional bandwidth	$\beta = 0.936$
Elevation	$0°$
Azimuth	$0.2° : 0.2° : 360.0°$
Azimuth subwindow	$10°$ Hanning
Frequency subwindow	halfband Hanning
Number of subbands	$I = 5$
Intensity threshhold	top 25 db
Subaperture summation	coherent
Oversampling	none

wise, the curved edges near $(0.5, \pm 0.75)$ m are likely classified as cylinders for similar reasons. As described in Section 2.2.1, it has been shown that curved edges create point scatterers having a frequency response parameterized by $\alpha = -1$ [62, 84, 121]. The curved edge canonical scatterer is not included in the SPLIT algorithm because

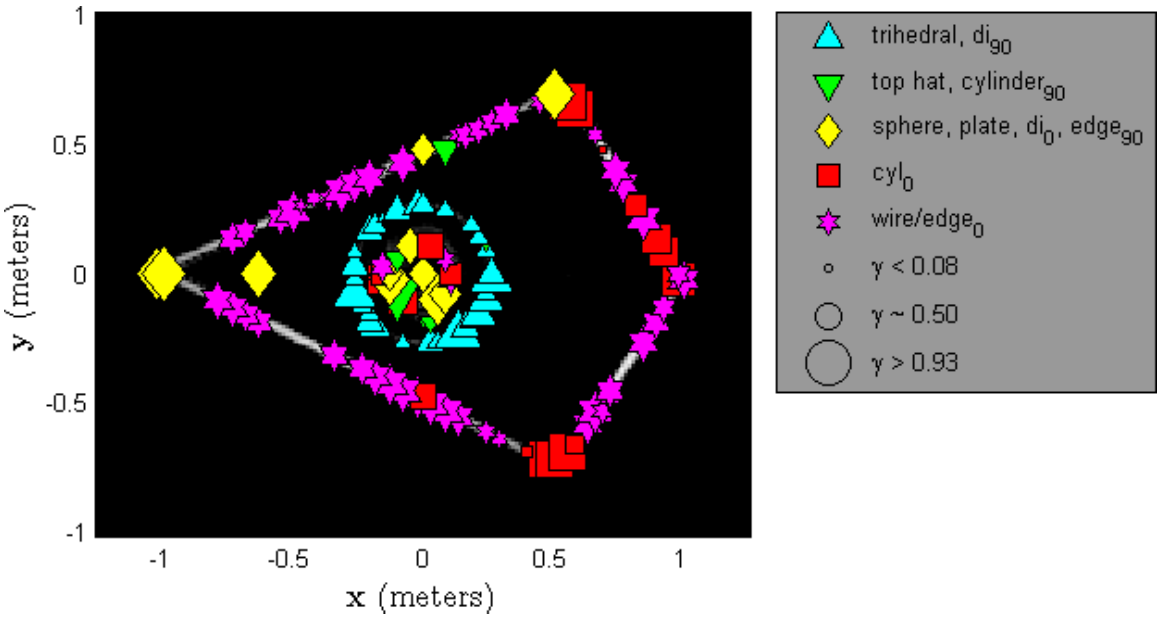

Figure 32. 2D ISAR measurement with superimposed HH and VV images and classification data.

its low RCS makes it likely to be unresolved in most SAR applications. However, for low RCS airframes where smaller RCS mechanisms are prevalent, the ideal feature vector $[\alpha', \kappa_o, \kappa_e] = [-1, 0.5, 0.5]$ could easily be included to account for curved edges.

Unfortunately, it is not entirely clear why the front tip at $(-1, 0)$ m is classified as a sphere or other scatterer with $\alpha' = 0$. It may be due to a traveling wave down the long edge [83]. Note also, that interference from neighboring scatterers in the center of the pedestal seems to have caused some confusion in the classifier. This interference is evident by the random classification results within a circle of radius 0.1 m in the center of the image. Interference from the pedestal is also likely to have impacted the classification results near $(0.1, 0.5)$ m. Overall, the classification results in Figure 32 could prove useful to an analyst, particularly the trihedral and edge classifications which appear symmetric. It is also likely that an experienced analyst will be able to disregard classification results in areas deemed likely to produce high levels of interference based on knowledge of the image context.

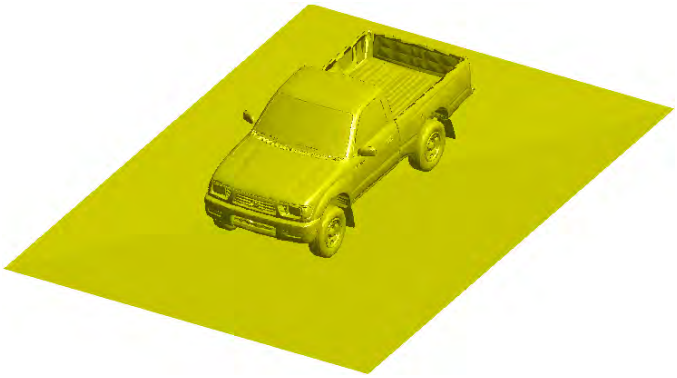

Figure 33. Facet model of Toyota Tacoma 2-door from 120-degrees azimuth and 30-degrees elevation.

Table 14. Experimental Parameters for Toyota Tacoma Data Dome.

Parameter	Value
Polarizations	VV, HH, and HV
Bandwidth (GHz)	6.9226 : 0.01046 : 12.2774
Fractional bandwidth	$\beta = 0.558$
Elevation	45°
Azimuth	0.0625° : 0.0625° : 360.0°
Azimuth subwindow	10° Hanning
Frequency subwindow	halfband Hanning
Number of subbands	$I = 5$
Intensity threshhold	top 40 db
Subaperture summation	multilook
Oversampling	none

5.4.3 Civilian Vehicle Data Domes.

The SPLIT classification algorithm was also run for a simulated data set of civilian vehicles, which are structurally more complex than D2. A facet model of the Toyota Tacoma vehicle from the Air Force Research Laboratory civilian vehicle (CV) data domes [124] is shown in Figure 33 and the classification results are given in Figure 34. The associated data parameters are listed in Table 14. The truck bed, in particular, provides a scatterer rich environment, creating interference to stress the classification algorithm. In addition, an the elevation angle of 45° combined

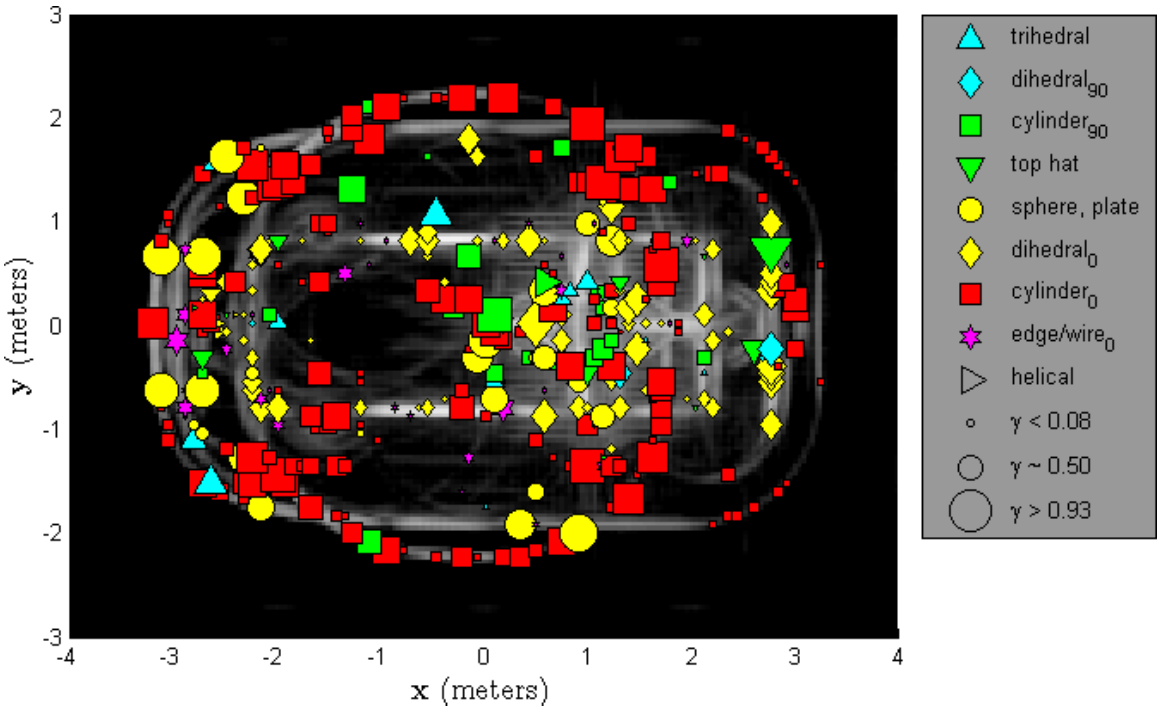

Figure 34. Annotated SAR image of a simulated Toyota Tacoma pointed in the $-x$ direction.

with ground plane imaging was chosen so that layover would separate some of the prime scattering mechanisms from potential sources of interference. Generally, the primary scattering mechanisms on civilian vehicles are cylindrical returns from the top edges of the vehicle and dihedral returns from the sides of the vehicle and the ground, as depicted in Figure 35 [44, 49]. Figure 36 shows the cylinder$_0$ and dihedral$_0$ classifications separately in Figures 36(a) and 36(b), respectively, to highlight these primary scattering mechanisms.

Despite the complexity of the target and the simplicity of the scatterer classifier, three dominant scattering mechanisms are identifiable as well classified. First, the cylindrical edges of the cab roof produce a large circular footprint with a radius of about 2.3 m centered at point $(-0.3, 0)$ m. The large circle appears in the image due to layover effect [76]. Most of the image peaks associated with this mechanism are correctly classified as a cylinder with a tilt angle of zero degrees. Second, the

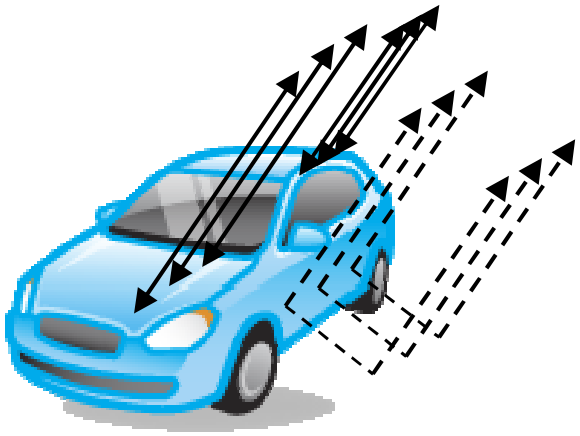

Figure 35. The dominant backscatter mechanisms for passenger vehicles are a single bounce from the top edge (solid lines) and double bounce from the dihedral formed with the ground plane (dotted lines).

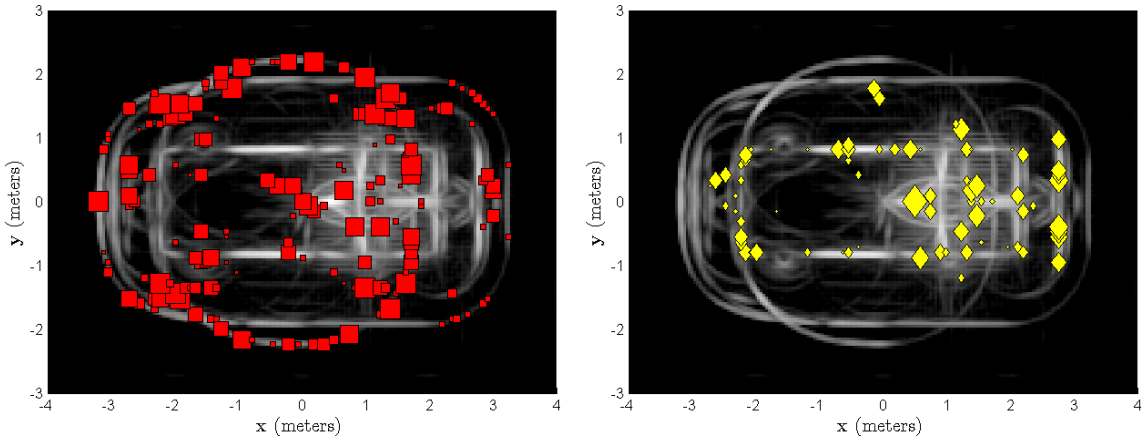

(a) Horizontal cylinders only

(b) Horizontal dihedrals only

Figure 36. Classification results for the Toyota Tacoma for specific scatterers.

right angle formed between the rear bumper and tailgate produces a vertical line about 1.5 m long centered at point $(2.9, 0)$. The displacement from the tailgate located at $x \approx 2.2$ m is due to layover effect. Most of the image peaks associated with this mechanism are correctly classified as a dihedral with a tilt angle of zero degrees. Third, the right angles formed between the truck body and the ground plane produce a rectangular footprint about 1.5 m along the **y**-axis and 4.5 m along the

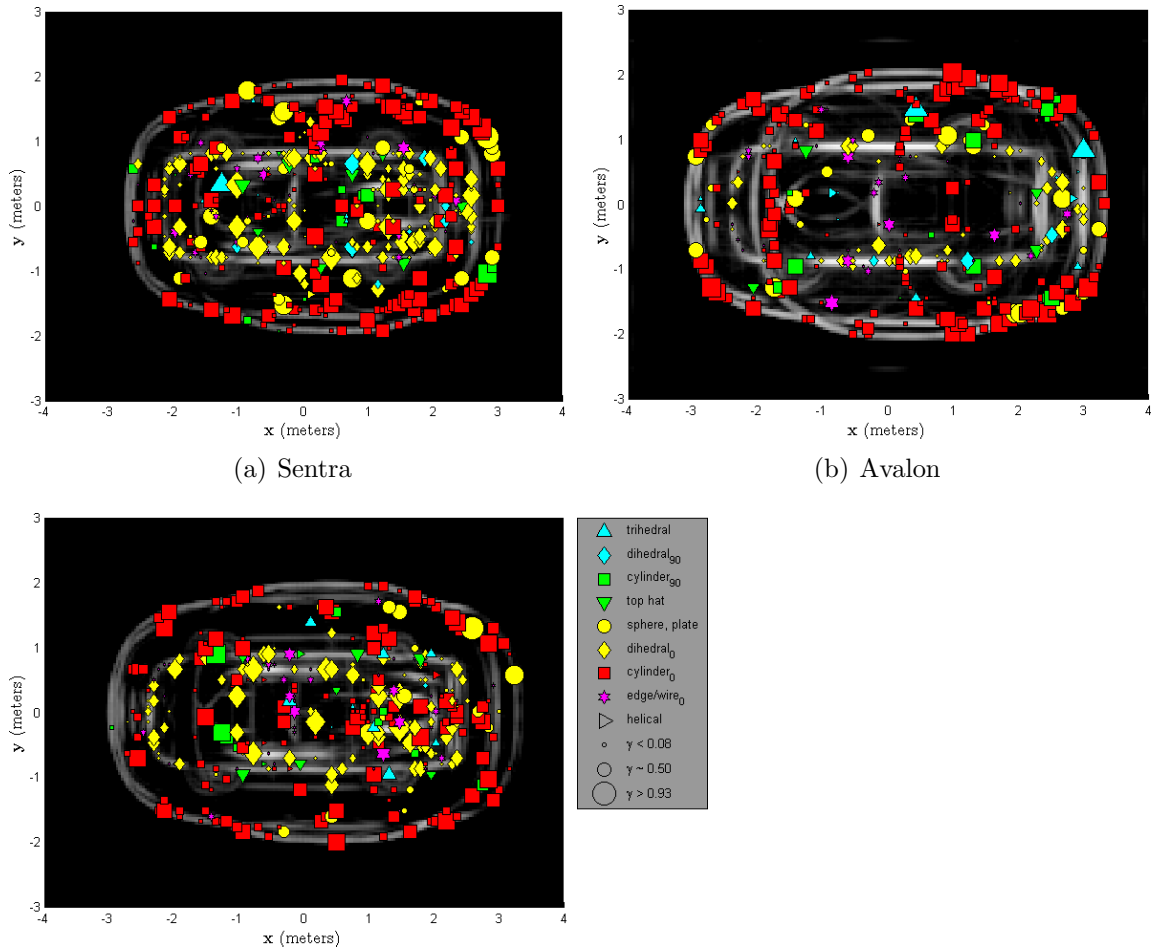

(a) Sentra

(b) Avalon

(c) Maxima

Figure 37. Annotated SAR images of three automobiles, each pointed in the $-x$ direction.

(x)-axis centered at $(0, 0)$. Many of the image peaks associated with this mechanism are correctly classified as a dihedral with a tilt angle of zero degrees; however, a preponderance of clutter, particularly from the wheels and wheel wells compromise the classification results. All three mechanisms are examples of distributed canonical scatterers found in the geometry of the target which are well classified using the multi-peak model. These scattering mechanisms are also identifiable for the sedans featured in Figure 37, where an inner rectangle of horizontal dihedrals is ringed by horizontal cylinders.

Table 15. Experimental Parameters for Gotcha Data Set.

Parameter	Value
Polarizations	HH, VV, HV, and VH
LFM Frequencies (GHz)	$9.2881 : 0.0014 : 9.9105$
Fractional bandwidth	$\beta = 0.0648$
Mean Elevation	43°
Ground Range Resolution	0.17 meters
Azimuth	$-179.9934^\circ : 0.0084^\circ : 179.9982^\circ$
Azimuth subwindow	10° Hanning
Frequency subwindow	halfband Hanning
Number of subbands	$I = 3$
Intensity threshhold	top 45 db
Subaperture summation	coherent
Oversampling	2x
Autofocus	yes, given in data set

5.4.4 Gotcha Public Release Data.

In 2007, the Air Force Research Laboratory publicly released a challenge data set featuring several circular SAR measurements of a parking lot scene [25]. One of these measurements, called pass number six, appeared to have superior stability in the circular aperture as evidenced by images with better focus. The radar data from pass number six is used exclusively in the following analysis, and its parameters are listed in Table 15. Note that the LFM Frequency and Azimuth values are listed as `start:increment:end` values from the Gotcha data.

Ideally, the SAR system collects data at regular intervals along the circular flight path so that the spectral domain is uniformly sampled in azimuth. However, this is generally not the case. Flight dynamics and variable winds cause the ground speed and altitude of the airborne radar to vary throughout the flight path. These conditions are controlled to the best extent possible, resulting in azimuth sampling that is pseudo-uniform and an elevation angle which varies slightly around the mean. Such variances are typical in circular SAR data and are not expected to adversely

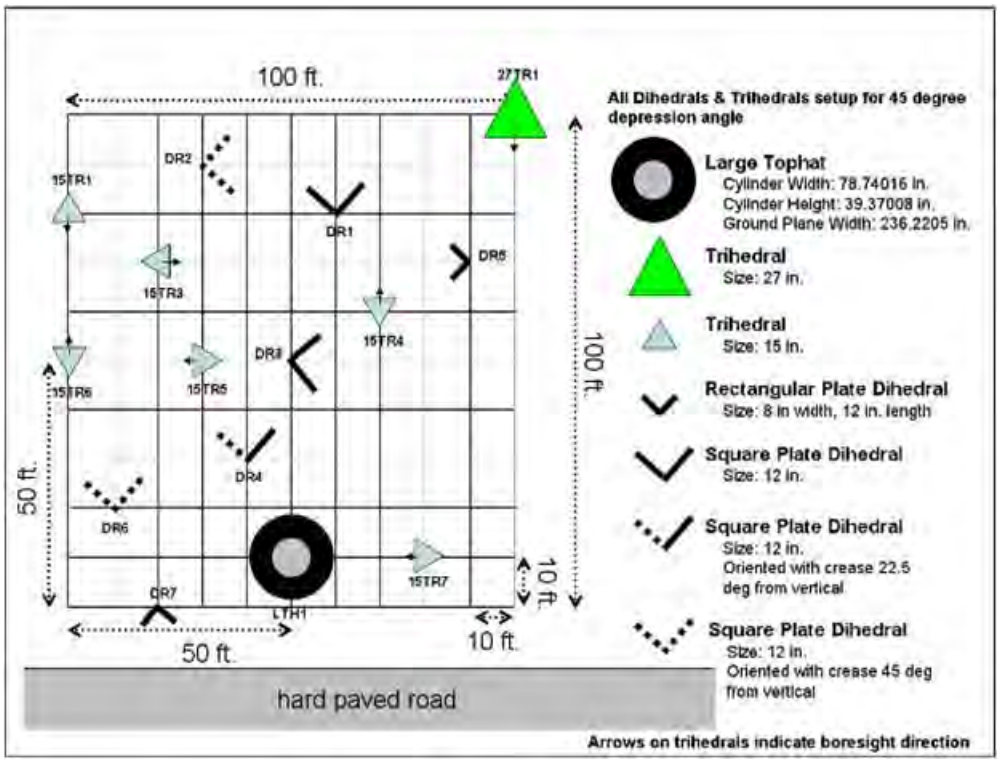

Figure 38. Gotcha calibration target types and locations taken from Gotcha data set documentation [25].

affect the suitability of the data for use in the following empirical studies, as long as the distance from the antenna phase center to the scene center is known for every sample in azimuth.

One notable benefit of the parking lot scene featured in this data set is that it includes fifteen calibration targets, as depicted in Figure 38 and listed in Table 16. There is one large top hat, shown in Figure 39, as well as seven trihedrals and seven dihedrals of varying sizes and orientations. The calibration targets were placed in a field near the parking lot as shown in Figure 40. These calibration targets are useful for evaluating the classification accuracy of the SPLIT algorithm.

Figure 41 presents scatterer classification results for the fifteen calibration targets of the Gotcha data set. The only scatterers that appear to be well classified are 27TR1 near $(-7, 52)$ m, DR3 near $(-18, 33)$ m, DR5 near $(-13, 32)$ m, and DR7

Table 16. Calibration Targets for Gotcha Data Set [25].

Calibration Target	ID#	x (m)	y (m)	z (m)
15 in Trihderal	15TR-01	-32.14	42.54	-0.53
15 in Trihderal	15TR-03	-28.09	38.67	-0.42
15 in Trihderal	15TR-04	-13.86	37.70	-0.05
15 in Trihderal	15TR-05	-24.39	32.96	-0.33
15 in Trihderal	15TR-06	-32.50	33.41	-0.57
15 in Trihderal	15TR-07	-5.12	22.98	-0.05
27 in Trihderal	27TR-01	-7.51	51.47	-0.09
12 in 12 in Dihedral	DR-01	-15.55	42.96	-0.13
12 in 12 in Dihedral	DR-02	-26.16	45.64	-0.43
12 in 12 in Dihedral	DR-03	-18.58	33.53	-0.18
12 in 12 in Dihedral	DR-04	-20.88	27.10	-0.23
12 in 8 in Dihedral	DR-05	-13.24	32.09	-0.09
12 in 12 in Dihedral	DR-06	-29.27	24.48	-0.48
12 in 8 in Dihedral	DR-07	-26.15	17.50	-0.44

Figure 39. Photo of top hat calibration target from Gotcha data set. [25].

near $(-26, 17)$ m, where trihedral and dihedral classifications dominate. Overall, the classifier showed little confusion in determining the polarimetric response of scatterers, but it showed some confusion in determining the frequency response of scatterers. For instance, none of the trihedrals is classified as even-bounce, and none of the dihedrals or top hat is classified as odd-bounce.

For this data set, the confusion in determining frequency response is most likely due to a combination of poor coherency, stray clutter energy, unknown system biases, and small fractional bandwidth. Errors in measuring the distance between the scene center and the antenna phase center disrupts coherency of the SAR signal and vio-

Figure 40. Photo of Gotcha scene [25]. The calibration targets were placed inside the area marked with a black square.

lates the assumptions of the imaging operator. This, in turn, violates assumptions of the multi-peak model and SPLIT algorithm. While pass number six showed superior coherency when compared to the other passes, there still appeared to be significant errors affecting coherency, even after using the autofocus corrections made available in the data set. Furthermore, the parking lot scene was extracted using digital spotlighting [135] from a 5 km spotlight SAR collection, and it appeared that significant energy from moving vehicles and other clutter far removed from the parking lot had leaked into the data. Also, it is unclear how best to normalize the data for possible system induced biases in the data, such as power differences due to the antenna gain pattern. Finally, fractional bandwidth of 6.5-percent will likely lead to good classification results for simple calibration targets under ideal conditions. However, this fractional bandwidth was far too narrow to overcome the significant deficiencies of poor coherency, stray clutter energy, and unknown biases.

These non-ideal conditions provided an opportunity to stress the scatterer classifier in way that the previous two data sets did not. The classification results for the

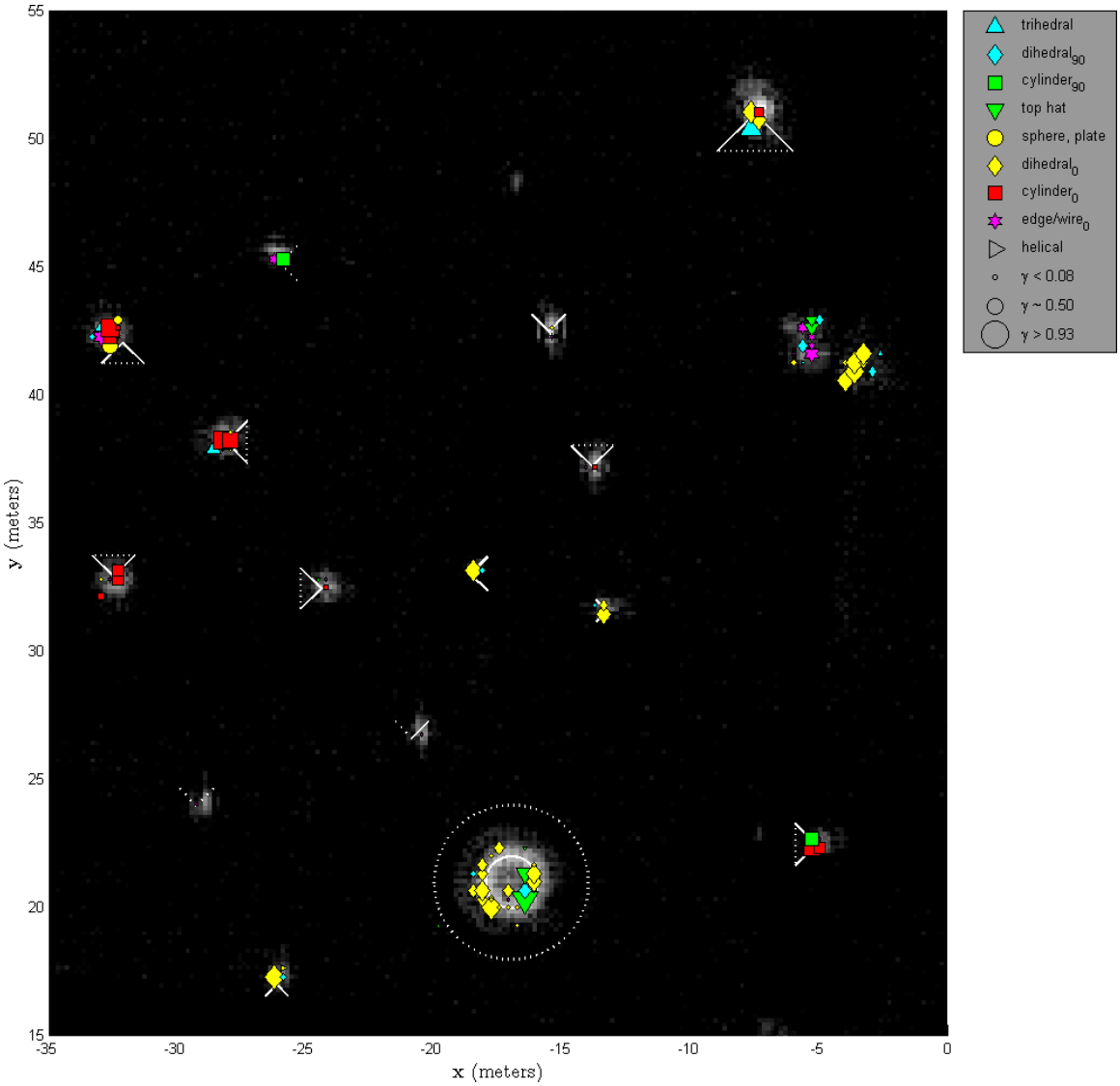

Figure 41. Scatterer classification results for the Gotcha calibration targets. Targets are drawn onto the image using white lines, where the trihedrals and dihedrals are at three times normal scale for visibility. The top 40 dB of pixel intensities are shown in the image.

Gotcha data set demonstrate some of the limitations of the SPLIT algorithm as well as the concept of scatterer classification by phase history decomposition, in general. Note that these non-ideal conditions greatly affect classification accuracy using image segmentation methods, and no satisfying scatterer classification results using image segmentation methods have been published for the Gotcha Public Release Data Set.

In order to understand how bandwidth, clutter, and interference affect classification accuracy, the following section presents some additional analyses and experiments.

5.5 Sensitivity to Bandwidth, Clutter, and Interference

To further illustrate some of the limitations of scatterer classification by phase history decomposition, the section concludes with experiments examining the effects of bandwidth, clutter, and interference on frequency parameter estimation. Classification accuracies for ideal scatterers are derived from Monte Carlo simulations based on a signal model that accounts for statistical interference from neighboring canonical scatterers, clutter, and noise. The fractional bandwidth is shown to be a primary contributor to classification accuracy, and for typical SAR applications, fractional bandwidths of 10-percent or more are recommended as a rule-of-thumb. The following studies focus on the frequency parameter α' because it is more sensitive to bandwidth than the polarimetric parameters. The assumption is that signal conditions which favor a good α' estimate also produce excellent polarimetric parameter estimates.

5.5.1 Signal Model.

SAR imaging is a coherent process that can be interpreted as matched filtering the received signal to the expected signal due an ideal point scatterer centered at each pixel location [76, 93]. Therefore, by replacing the integrals in Equation (37) of Section 4.4 with summations and normalizing the integrand by $\frac{1}{H_B(f-f_c)H_\Theta(\theta-\theta_c)}$, the subimage peak intensity due to a single canonical point scatterer is approximated by

$$P_{\text{signal}} = |\tilde{s}_q(x_q, y_q)|^2 \approx \left(N_s |A'(jf_c)^{\alpha'/2}||f_c|\right)^2, \tag{92}$$

where the narrow-band approximation, $f = f_c$, is used, and N_s is the number of frequency and azimuth samples. For wide-angle and wide-band systems, the number of samples is expected to be quite large. For instance, in the case of 128 frequency samples and 128 azimuth samples the total number of samples is $N_s = 16384$. Note that Equation (92) assumes a sampling loss of zero, whereby the location of the scatterer is exactly in the center of a pixel [133]. The zero sampling loss assumption corresponds with use of the SPLIT algorithm, whereby canonical scatterers located at or near the center of a pixel have a greater chance of passing the stable peak criterion.

In practice, the subimage peak intensity also includes contributions due to interference from neighboring scatterers, clutter, and noise. Therefore, the subimage peak signal model is given as

$$y = N_s \left[A'(jf_c)^{\alpha'/2} + s_{\text{interference}} + s_{\text{clutter}} + s_{\text{noise}} \right] |f_c|, \tag{93}$$

where the interference, clutter, and noise are modeled as random variables (RVs). These are discussed next, starting with the noise term.

5.5.1.1 Noise Model.

It is common to model SAR system noise as additive white Gaussian noise (AWGN) [133, 93]. The noise has a circular symmetric complex normal distribution expressed as [133, 116]

$$s_{\text{noise}} = W, \quad W \sim \mathcal{CN}(0, \sigma_W^2), \text{iid}, \tag{94}$$

where samples of the AWGN are independent and identically distributed (iid). The magnitude is Rayleigh distributed with variance, $\text{VAR}(W) = \frac{4-\pi}{2}\sigma_W^2$, so that the

subimage peak intensity due to noise alone is

$$P_{\text{noise}} = N_s E\left[|W|^2\right] |f_c|^2 = N_s \left[\frac{4-\pi}{2}\sigma_W^2\right] f_c^2, \tag{95}$$

where $E[\cdot]$ is the expected value of the RV.

As a result, the signal-to-noise ratio (SNR) is

$$\text{SNR} = \frac{P_{\text{signal}}}{P_{\text{noise}}} \approx N_s \frac{2|A'|^2 f_c^{\alpha'}}{(4-\pi)\sigma_W^2}. \tag{96}$$

It can be seen that coherent integration serves to greatly increase the SNR. For instance, in the case of large N_s, even scattering centers with very weak amplitudes can obtain a high SNR.

5.5.1.2 Clutter Model.

Clutter is caused by backscatter from the natural environment [133]. Examples include surface clutter from the ground and volume clutter from rain [133]. The definition of clutter depends upon the unwanted signal, as determined by the specific application. For the purposes of these experiments, the clutter is modeled as surface clutter from a large region of unresolved scatterers, where none of the individual scatterers is significantly stronger than the others [133].

Under these assumptions, the clutter has a circular symmetric complex normal distribution expressed as [133, 116]

$$s_{\text{clutter}} = |X|e^{j\phi_X}, \quad |X| \sim \text{Rayleigh}(\sigma_X), \quad \phi_X \sim \mathcal{U}[-\pi, \pi], \quad X \perp\!\!\!\perp \phi_X, \tag{97}$$

where the magnitude has a Rayleigh distribution and the phase difference between the signal and clutter, ϕ_X, is iid and has a uniform distribution. Here, the magnitude and

phase are independent RVs. Samples of clutter are identically distributed, but unlike noise, they are correlated. Therefore, the subimage peak intensity due to clutter alone is greater than that for uncorrelated samples

$$P_{\text{clutter}} > N_s E\left[\text{abs}\left(|X|e^{j\phi_X}\right)^2\right]|f_c|^2 = N_s\left[\frac{4-\pi}{2\sqrt{2}}\sigma_X^2\right]f_c^2 \tag{98}$$

and less than that for perfect correlation

$$P_{\text{clutter}} < N_s^2 E\left[\text{abs}\left(|X|e^{j\phi_X}\right)^2\right]|f_c|^2 = N_s^2\left[\frac{4-\pi}{2\sqrt{2}}\sigma_X^2\right]f_c^2. \tag{99}$$

Here the factor $\frac{1}{\sqrt{2}}$ produces an RMS value due to the random phase.

Because of this wide range of possible values, the clutter power is parameterized, with the parameter being measured or approximated for a given type of surface. Following Reference [133], the parameterized clutter model assumes perfect correlation, and then simply scales the power using an effective clutter RCS, σ_c, for the clutter occupying the area, A_c, illuminated by a single range cell of the radar. These are combined to provide a normalized clutter RCS, $\sigma^0 = \frac{\sigma_c}{A_c}$, with values generally ranging from -10 dB for mountains and urban terrain to -40 dB for grassland, depending upon depression angle and operating frequency [133]. The signal-to-clutter ratio (SCR) is [133].

$$\text{SCR} = \frac{P_{\text{signal}}}{P_{\text{clutter}}} \approx \frac{N_s^2|A'|^2 f_c^{\alpha'} f_c^2}{\sigma_c}, \tag{100}$$

where using Equation (99), the relation to the clutter RV is

$$\sigma_c = A_c\sigma^0 = N_s^2\left[\frac{4-\pi}{2\sqrt{2}}\sigma_X^2\right]f_c^2. \tag{101}$$

5.5.1.3 Interference Model.

For these experiments, interference is caused by the sidelobes of the PSFs of strong neighboring scatterers in the scene. These sidelobes are coherently summed to produce the interference term for a given sample. The difference between interference and clutter is that the clutter model assumes none of the individual scatterers are significantly stronger than the others, while the interference model does not assume uniformity among scatterers [133, 116].

Under these assumptions, the interference is modeled as having a magnitude with a gamma distribution and a phase, ϕ_Z, with a uniform distribution. The interference is modeled as

$$s_{\text{interference}} = |Z|e^{j\phi_Z}, \quad |Z| \sim \Gamma(N_i, \sigma_Z), \quad \phi_Z \sim \mathcal{U}[-\pi, \pi], \quad Z \perp\!\!\!\perp \phi_Z. \tag{102}$$

According to Reference [116], the gamma distribution parameters can be interpreted as N_i being equal to the number of dominant interfering scatterers with mean RCS equal to σ_Z. The samples of interference are identically distributed and, for simplicity, assumed to be perfectly correlated in magnitude and iid in phase. Therefore, the subimage peak intensity due to interference alone is

$$P_{\text{interference}} < N_s^2 E\left[\text{abs}\left(|Z|e^{j\phi_Z}\right)^2\right]|f_c|^2 = N_s^2\left[\frac{N_i\sigma_Z^2}{\sqrt{2}}\right]f_c^2, \tag{103}$$

where the factor $\frac{1}{\sqrt{2}}$ produces an RMS value due to the random phase.

Thus, the corresponding signal-to-interference ratio (SIR) is

$$\text{SIR} = \frac{P_{\text{interference}}}{\text{P}_{\text{noise}}} \approx \frac{\sqrt{2}|A'|^2 f_c^{\alpha'}}{N_i\sigma_Z^2}. \tag{104}$$

5.5.2 Scatterer Classification Accuracy Experiments.

The curve fitting algorithm described in Section 5.1.3.1 allows the frequency parameter to assume a value in the continuous interval $\alpha' \in [-4, 4]$. This was done to facilitate weighted averaging of α' from multiple subapertures and co-polarization channels. In contrast, the experiments presented in this section are restricted to a single aperture, where the correlation is unspecified between subapertures and co-polarization channels for the signal model in Equation (93). In this case, it is simpler to allow the frequency parameter to assume a discrete value, $\alpha'_p = p$, in the set $p \in \{-5, -3, -2, -1, 0, 1, 2, 3, 5\}$. In this way, the classification decision is made according to the minimum total least squares metric between the simulated observation vector and the seven ideal curves given by $\mathbf{f}(p)$ from Equation (62) of Section 5.1.3.1, for a given fractional bandwidth, $\beta = \frac{B}{f_c}$. In this case, a classification decision at the extremes of $p \in \{-5, 5\}$ causes the SPLIT algorithm to erroneously reject the canonical scatterer as non-canonical, that is $\alpha' \notin [-4, 4]$. Such an event can be interpreted as a missed detection due to a high level of interference, clutter, noise, or a combination of these in the simulated observation vector.

Referring to Equation (63) of Section 5.1.3.1 and to Equation (93), the mth simulated observation vector for a given α', SIR, SCR, and SNR is given by

$$\begin{aligned} \boldsymbol{\sigma}_m &= \left[|y|^2_{1m}, |y|^2_{2m}, \ldots, |y|^2_{3m}\right]^T \\ &= \begin{bmatrix} \left(|A'| f_{c1}^{1+\alpha'/2} + Z_m e^{j\phi_{Z_1}} f_{c1} + X_m e^{j\phi_{X_1}} f_{c1} + W^{real}_{1m} f_{c1}\right)^2 \\ \left(|A'| f_{c2}^{1+\alpha'/2} + Z_m e^{j\phi_{Z_2}} f_{c2} + X_m e^{j\phi_{X_2}} f_{c2} + W^{real}_{2m} f_{c2}\right)^2 \\ \vdots \\ \left(|A'| f_{cI}^{1+\alpha'/2} + Z_m e^{j\phi_{Z_I}} f_{cI} + X_m e^{j\phi_{X_I}} f_{cI} + W^{real}_{Im} f_{cI}\right)^2 \end{bmatrix}, \end{aligned} \tag{105}$$

where Z_m and X_m are the values of the RVs Z and X, respectively, for the mth

observation. Likewise, ϕ_{Z_i} and ϕ_{X_i} are the values of the RVs ϕ_Z and ϕ_X for the ith subband. Finally, the real component of the noise is taken to be in-phase with the signal, without loss of generality, so that W_{im}^{real} is the value of the in-phase component of the RV W for the ith subband and mth observation. Note that the normalization factor, ν_m, includes the factors $N_s^2 f_c^2$, which assumes that the number of phase history samples is identically equal to N_s for each subdomain.

The experiments in this section normalize $|A'|$ and f_c to unity, without loss of generality. Also, to normalize the signal power, the frequency parameter is set to $\alpha' = 0$, which represents an average value assuming equal prior probabilities for each class of scatterer. As a result, the variances are normalized to

$$\bar{\sigma}_Z^2 = \frac{\sqrt{2}}{N_i(\text{SIR})}, \qquad \bar{\sigma}_X^2 = \frac{2\sqrt{2}}{(4-\pi)(\text{SCR})}, \qquad \bar{\sigma}_W^2 = \frac{2N_s}{(4-\pi)(\text{SNR})}. \tag{106}$$

Because AWGN is uncorrelated, the SNR is usually much larger than SIR or SCR. Therefore, it is ignored in these experiments by setting SNR $= \infty$. This allows the primary effects of bandwidth, SCR, and SIR to be examined in more detail. The classification accuracy for varying fractional bandwidths, SIR, and SCR_0 are shown in Figure 42. These were produced from Monte Carlo simulations of ten thousand observation vectors for each combination of fractional bandwidth, SIR, and SCR_0. The use of SCR_0 accounts for the fact that SCR is actually dependent upon subimage pixel area, A_c, which in turn is dependent upon bandwidth. In order normalize the SCR for each fractional bandwidth, SCR_0 was chosen according to the Gotcha data set, where $A_c = 0.45$ m^2 and $\beta_0 = 0.065$. Hence, in order to account for changing subimage pixel area, the SCR for each fractional bandwidth varied as

$$\text{SCR}(\beta) = \text{SCR}_0(\beta_0^2/\beta^2). \tag{107}$$

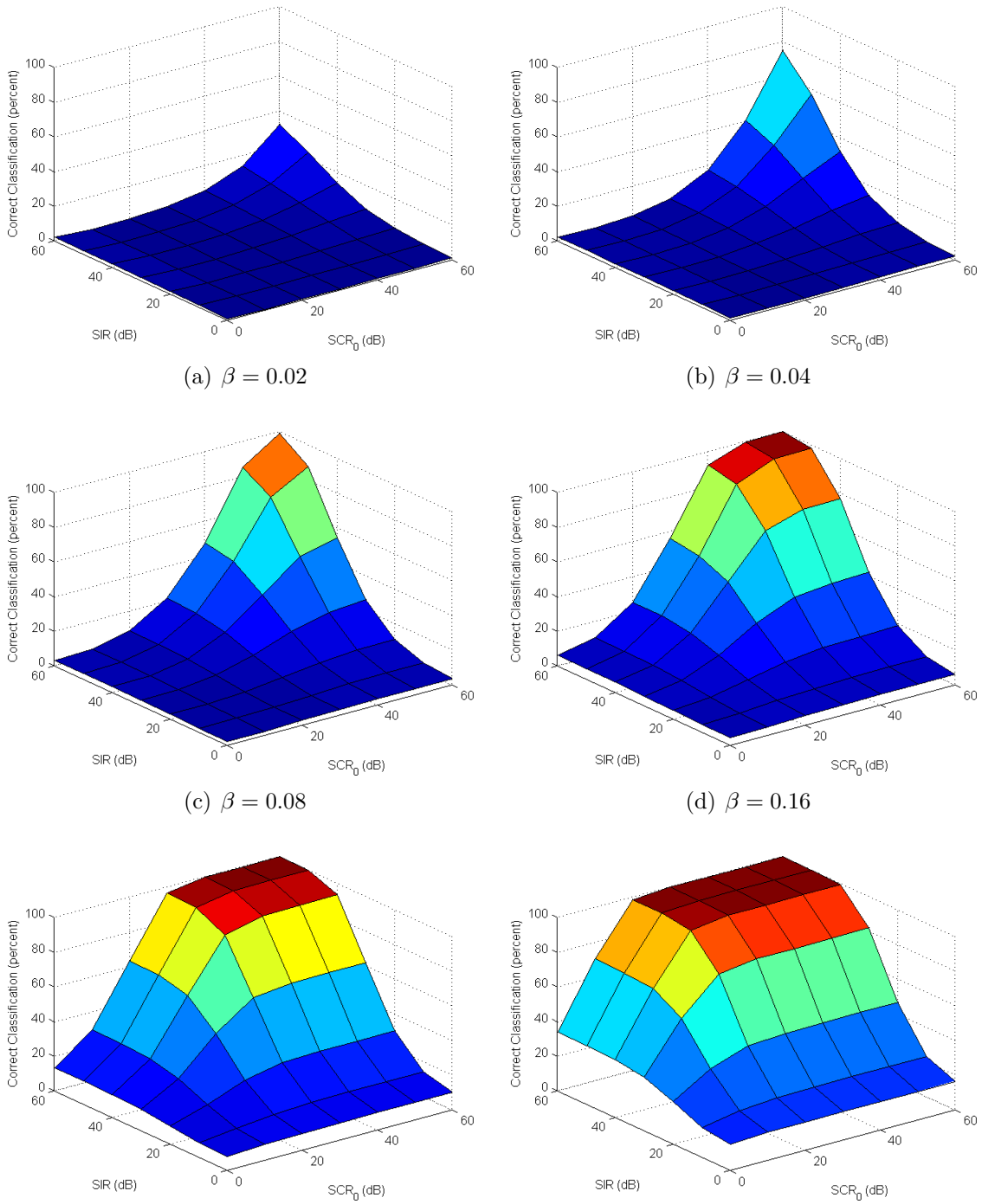

(a) $\beta = 0.02$ (b) $\beta = 0.04$

(c) $\beta = 0.08$ (d) $\beta = 0.16$

(e) $\beta = 0.32$ (f) $\beta = 0.64$

Figure 42. Classification accuracies for the case of $I = 3$ subbands, $\beta_0 = 0.065$, $N_i = 2$ interferers, and SNR $= \infty$ for varying fractional bandwidth, β, SIR, and SCR$_0$.

In addition, the number of subbands was set to $I = 3$, and the number of neighboring scatterers was set to $N_i = 2$ for these experiments.

Correct classifications occurred when the declared α' was equal to the true α', that is when $\alpha' = p$. Alternately, note that the canonical range, $\alpha' \in [-4, 4]$, means that a declared value of $\alpha' = -3$ for true $\alpha' = -2$ and a declared value of $\alpha' = 3$ for true $\alpha' = 2$ could both be recategorized as correct classifications, if desired. In these cases, the extracted feature vector contributes to the average feature vector so as to produce a correct classification, but with slightly lower measure of fitness. In this alternate case, the classification accuracies in Figure 42 would increase.

Figure 42 reveals that classification accuracy is greatly impacted by fractional bandwidth, regardless of SIR or SCR. For instance, Figure 42(a) reveals that for very low fractional bandwidth, $\beta = 0.02$, SIR and SCR_0 must both be at 60 dB or greater before the classification results are even above 25-percent. Any point where classification accuracy is above 20-percent can be loosely interpreted as a case where the least squares classifier produces better results than a random classifier resembling to a 'coin toss.' However, the inclusion of $p \in \{-5, -3, 3, 5\}$ complicates the interpretation.

Note, that the Euclidean norm varies slightly between the adjacent pairs of ideal curves, $||\mathbf{f}(p) - \mathbf{f}(p+1)||_2$. For example, in the case of $I = 3$ and $\beta = 0.5$,

$$\begin{aligned} ||\mathbf{f}(-2) - \mathbf{f}(-1)||_2 &= 0.1768, \\ ||\mathbf{f}(-1) - \mathbf{f}(0)||_2 &= 0.1782, \\ ||\mathbf{f}(0) - \mathbf{f}(1)||_2 &= 0.1849, \\ ||\mathbf{f}(1) - \mathbf{f}(2)||_2 &= 0.1967. \end{aligned} \tag{108}$$

This is one factor that will cause classification accuracy to vary slightly for different values of α'. These can be adjusted to become more equal by adjusting the normal-

ization factor, f_c, used in $(f) = p$. With a small adjustment, it is possible that overall classification accuracy can be slightly improved for these experiments. However, the signal model includes assumptions, such as non-dispersive clutter and interference, which reduce the value of such fine precision adjustments, in practice. Furthermore, the optimal normalization frequency is expected to be closer to f_c, in general, for rectangularly shaped phase histories where the Jacobian, $|f_c|$, is removed from the imaging operator, as discussed in Section 5.1.3.

The confusion matrices in Table 17 are provided to illustrate how classification accuracy varies between different values of α' for the cases of interference only (top) and clutter only (bottom). The values in red italics indicate the number of correctly classified scatterers out of one-hundred thousand trials for each value of α'. There seems to be competing trends in the data. While in some cases classification accuracy tends to improve as α' increases, in other cases, accuracy improves as α' decreases. The inflexion points for these trends depend upon the amount of clutter or interference present. In theory, these trends can be modified by adjusting the normalization factor in $(f) = p$, but since the SCR and SIR are not usually known *a priori*, this is not very practical.

The confusion matrix in the bottom left-hand corner of Table 17 for SCR = 30 dB seems to mimic the marginal classification accuracy for the Gotcha data experiment of Figure 41 of Section 5.4.4. However, the SCR for the top hat and six smaller trihedrals can be readily calculated as

$$\text{SCR} = \frac{\sigma_{tophat}}{\sigma^0 A_c} \approx \frac{800 \text{ m}^2}{(-10 \text{ dB})(0.455 \text{ m}^2)} = 42 \text{ dB}, \tag{109}$$

where $\sigma_{tophat} \approx 800 \text{ m}^2$ is approximated using the equation for cylinder RCS given in Figure 8 of Section 2.2.1 and $\sigma^0 \approx -10$ dB is taken from table 7.11 of Reference [133]. The difference between an SCR of 42 dB and a classification performance that

Table 17. Simulated Confusion Matrices for the Case of $\beta_0 = 0.065$, $I = 3$ subbands, $N_i = 2$ interferers, and SNR $= \infty$.

		True α' value									
		SIR $= 30$ dB, SCR $= \infty$					SIR $= 50$ dB, SCR $= \infty$				
		-2	**-1**	**0**	**1**	**2**	**-2**	**-1**	**0**	**1**	**2**
Declared α' value	**-5**	21883	15463	11130	7906	5863	64	4	-	1	-
	-3	16654	10607	7210	5202	3706	8067	334	18	-	-
	-2	*22886*	12389	7808	5374	3612	*83929*	7904	328	20	1
	-1	12470	*22764*	12540	7832	5325	7579	*83722*	7728	372	26
	0	7632	12467	*22771*	12500	7845	343	7701	*83729*	7792	327
	1	5301	7804	12333	*22517*	12593	18	322	7857	*83604*	7723
	2	3707	5341	7775	12545	*22682*	-	12	323	7859	*83713*
	3	3606	5127	7259	10754	16847	-	1	17	350	8132
	5	5861	8038	11174	15370	21527	-	-	-	2	78
		Classification Accuracy $= 22.7240\%$					Classification Accuracy $= 83.7394\%$				

		True α' value									
		SIR $= \infty$, SCR $= 30$ dB					SIR $= \infty$, SCR $= 50$ dB				
		-2	**-1**	**0**	**1**	**2**	**-2**	**-1**	**0**	**1**	**2**
Declared α' value	**-5**	28514	22183	17310	13022	10194	59	1	-	-	-
	-3	13599	10041	7797	6455	5059	13213	499	2	-	-
	-2	*15940*	10052	7190	5630	4454	*73425*	12723	529	6	-
	-1	9965	*15796*	9997	7162	5624	12789	*73500*	12915	525	6
	0	7151	9875	*15787*	10195	7073	512	12769	*73144*	12824	496
	1	5492	7049	9891	*15766*	10320	2	502	12899	*73233*	12774
	2	4323	5570	7237	9991	*15566*	-	6	508	12863	*73262*
	3	5049	6344	7785	10072	13762	-	-	3	549	13404
	5	9967	13090	17006	21707	27948	-	-	-	-	58
		Classification Accuracy $= 15.771\%$					Classification Accuracy $= 73.3128\%$				

mimics an SCR of 30 dB indicates that there is approximately a 12 dB loss factor in the Gotcha data due to poor coherency and stray clutter, as discussed earlier in Section 5.4.4.

5.5.3 Coupling Between Bandwidth and Interference.

As a simplification, the signal model and experiments treat bandwidth and interference as independent factors affecting classification accuracy. However, in reality, these are actually interdependent factors. The amount of sidelobe interference affecting the subimage pixel peak intensity is dependent upon the size of the pixel.

This coupling of interference power and bandwidth was not explicitly accounted for earlier, but can have a significant impact on classification accuracy, as illustrated in the following experiments.

Figure 43 illustrates the impact of bandwidth-interference coupling on classification accuracy for D2. All data parameters from Table 13, including center frequency, are held constant except for fractional bandwidth. The main source of interference is due to target-pedestal interactions in the center of the image. As the fractional bandwidth decreases, the SIR decreases for pixels at and near the center of the image. As a result, the classification accuracy for these pixels suffers. A most obvious example appears in Figure 43(d), where the ring of tri/dihedral classifications from Figure 43(e) disappears. Because this object is so simple and the edge scatterers are relatively isolated from neighboring scatterers, the edge classifications remain accurate even for smaller fractional bandwidths.

Figure 44 illustrates the impact of bandwidth-interference coupling for the Toyota Tacoma. The Toyota Tacoma is a more complex target than D2, causing a lower SIR for many of the scatterers. As a result, the major features described in Section 5.4.3 are evident in Figure 44(c), but dissipate at smaller fractional bandwidths.

Note that the SCR and SNR are approximately infinite in Figures 43 and 44, so that the impact of interference could be examined in isolation. Based on these and previous examples, it is recommended that the SPLIT algorithm be used only for fractional bandwidths of 10-percent or more for typical SAR applications, where targets are comprised of multiple canonical scatterers in close proximity.

5.5.4 Multiple Observations and Oversampling.

Classification accuracy is expected to improve as multiple observations of the scatterer are available. Recall that multiple observations are combined through a weighted

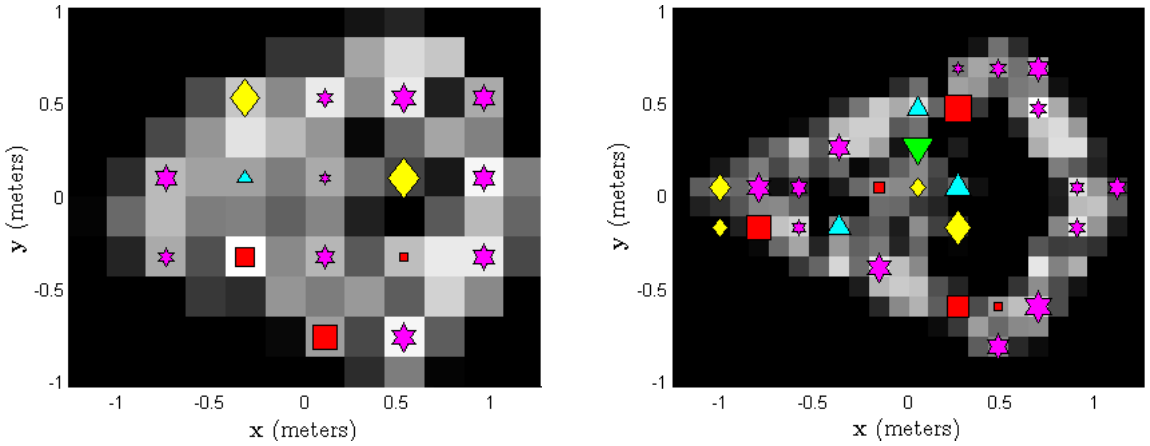

(a) $\beta \approx 0.06$ (b) $\beta \approx 0.12$

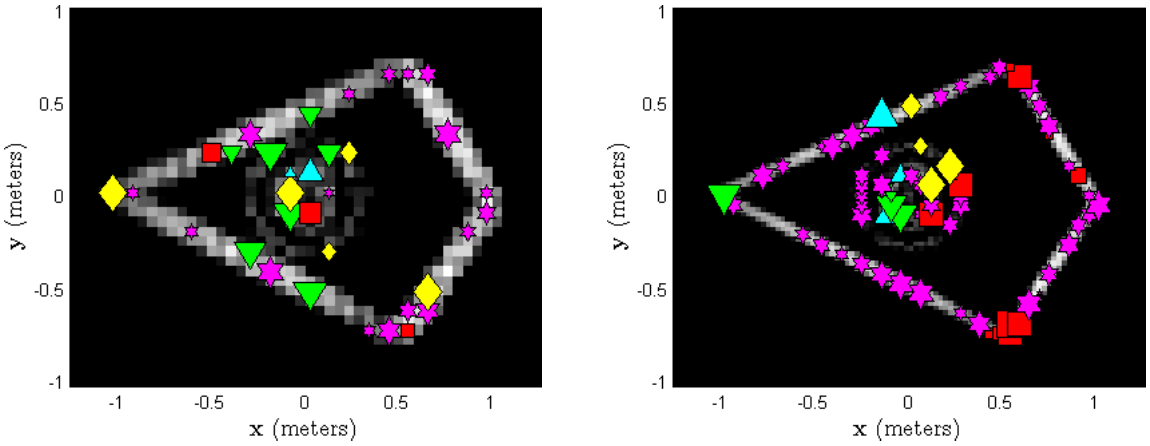

(c) $\beta \approx 0.23$ (d) $\beta \approx 0.47$

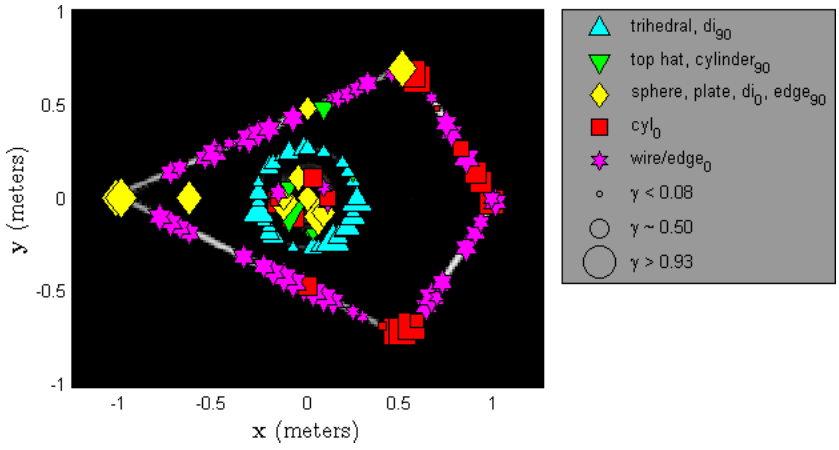

(e) $\beta \approx 0.94$

Figure 43. Classification results for D2 with changing fractional bandwidth.

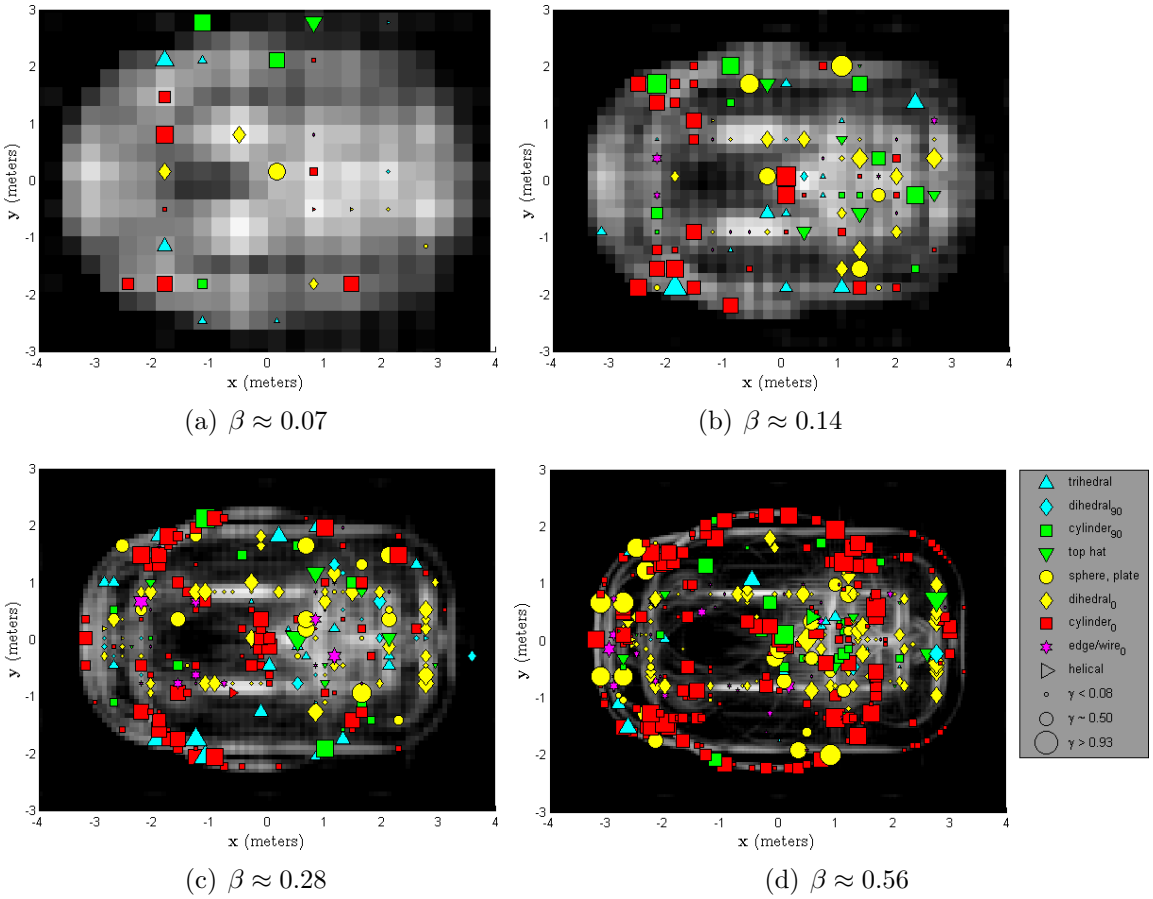

(a) $\beta \approx 0.07$ (b) $\beta \approx 0.14$

(c) $\beta \approx 0.28$ (d) $\beta \approx 0.56$

Figure 44. Classification results for the Toyota Tacoma with changing fractional bandwidth.

average of feature vectors, as described in Section 5.2. For the frequency parameter, multiple observations are potentially available through the two co-polarization channels, HH and VV, and through multiple subapertures. For co-polarization channels, the observations are considered completely independent, while for multiple subapertures, the observations are correlated because the clutter and interference contributions are correlated. For two independent observation vectors of equal weight, the benefit to classification accuracy can be equated to a doubling of the SIR and SCR for the single observation case. Although multiple observations are common in practice, these usually do not produce independent observation vectors of equal weight. Therefore, improvements to classification accuracy can be expected when multiple

observations are available, but usually less than that for the ideal scenario of doubling of the effective SIR and effective SCR as the number of observations doubles. The confusion matrices in Section 5.5.2 considered only a single observation, while the annotated images in Section 5.5.3 include all available opportunities for multiple observations.

Another way to increase the number of observations is by decomposing the phase history into an increasing number of subbands. In this case, the clutter and interference is expected to be highly correlated among the subimages, but the effective SIR and effective SCR are expected to improve slightly none the less. For example, Figure 45 shows the classification accuracy for the case of $I = 5$ and reveals that classification accuracy only slightly improves compared to the case of $I = 3$ in Figure 42. The model used in this experiment does not include the expected increase in correlation between interference and clutter samples when $I = 5$; so any improvements in classification accuracy represent a best case scenario.

The last consideration for classification accuracy is the effect of pixel oversampling. Pixel oversampling is defined as increasing the number of pixels in each resolution cell, and can be interpreted as an interpolation of the image samples. Because the SPLIT algorithm extracts feature vectors on a pixel-by-pixel basis, the size and number of the pixels could potentially have an impact on classification accuracy. The following is only a cursory discussion on classification accuracy trends due to oversampling because it is difficult to express the impact of oversampling analytically. Furthermore, the use of oversampling is often limited in practice because it results in an exponential increase in processing costs.

Oversampling limits the amount of interference energy in a given pixel and is therefore expected to increase the effective SIR. However, with oversampling there are more pixel boundaries and greater opportunity for a scatterer to be located very

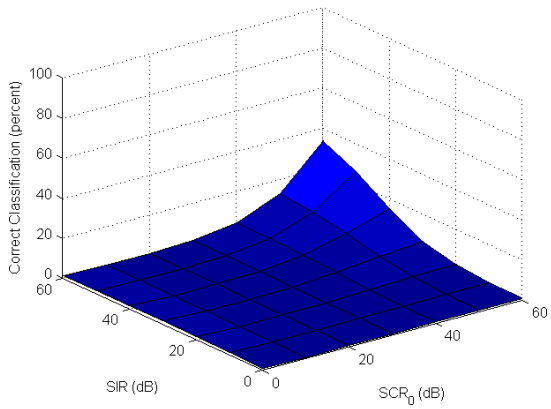

(a) $\beta = 0.02$

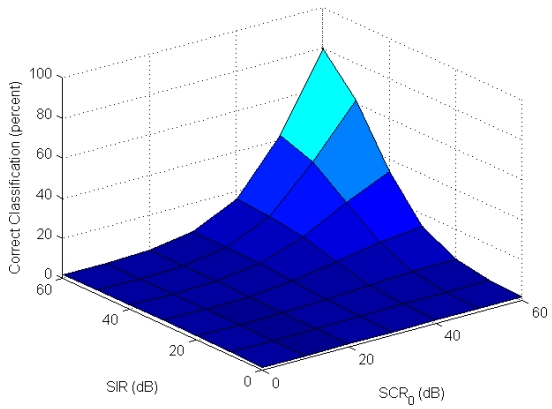

(b) $\beta = 0.04$

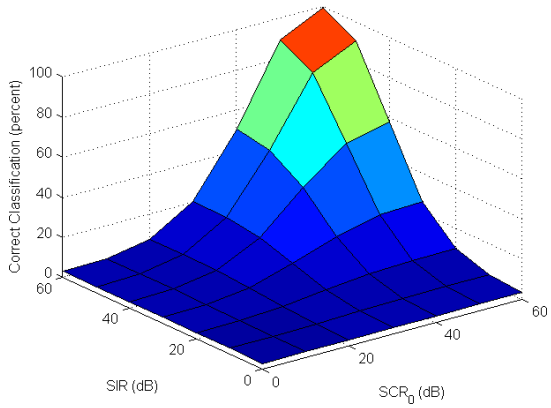

(c) $\beta = 0.08$

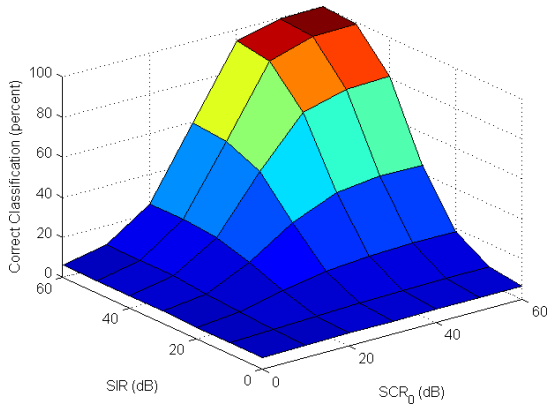

(d) $\beta = 0.16$

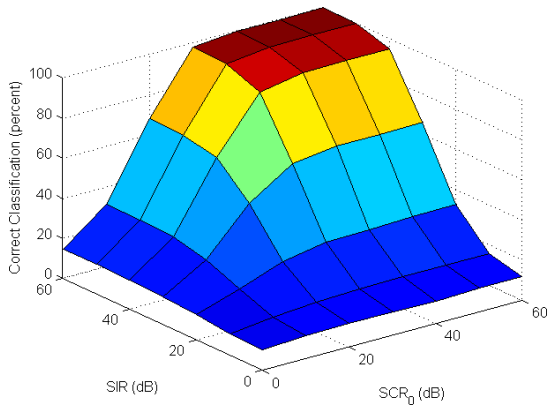

(e) $\beta = 0.32$

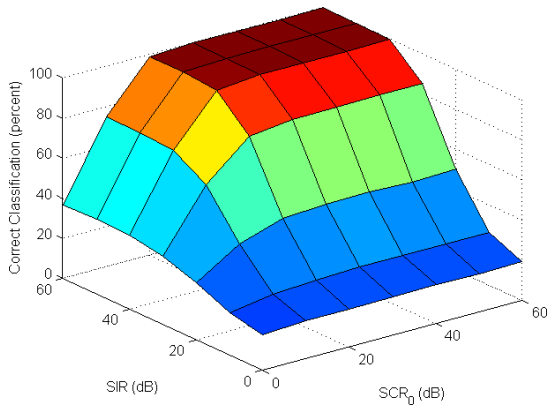

(f) $\beta = 0.64$

Figure 45. Classification accuracies for the case of $I = 5$ subbands, $\beta_0 = 0.065$, $N_i = 2$ interferers, and SNR $= \infty$ for varying fractional bandwidth, β, SIR, and SCR$_0$.

near a pixel boundary. When a scatterer is located very near a pixel boundary, there is a chance that noise and clutter interference may cause the subimage peak to migrate into a neighboring pixel, thereby causing the scatterer to fail the stable peak criterion of the SPLIT algorithm, as discussed in Section 5.1.1. Therefore, oversampling increases the probability of missed detections, which in turn, decreases the number of observations. Alternately, for scatterers near a boundary, the sampling loss may vary for each subband, thereby skewing the estimation of the frequency and polarimetric parameters during feature vector extraction. As a result, experience shows that classification accuracy may show only a slight overall improvement with increased oversampling, but usually not enough to warrant the increased processing cost.

As an example, classification results for 2× oversampling are given in Figure 46 for D2. When these classification results are compared to those in Figure 43, there does not seem to be a significant increase in classification accuracy due to oversampling. Furthermore, missed detections due to oversampling are evident, particularly in comparing Figure 46(e) to Figure 43(e).

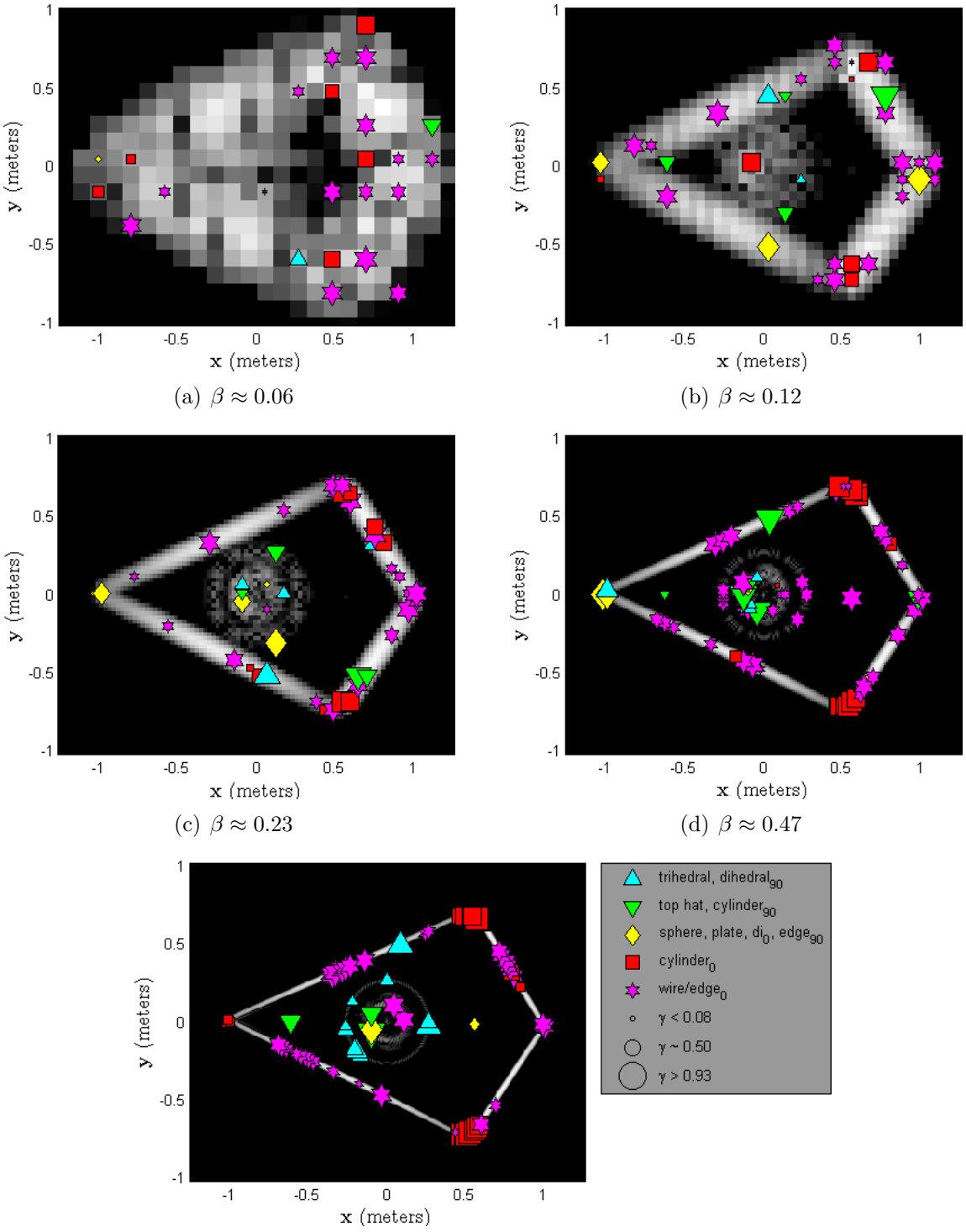

(a) $\beta \approx 0.06$ (b) $\beta \approx 0.12$

(c) $\beta \approx 0.23$ (d) $\beta \approx 0.47$

(e) $\beta \approx 0.94$

Figure 46. Classification results for D2 with 2× oversampling and changing fractional bandwidth.

VI. Integrated Domain Decomposition and Scatterer Classification Algorithm

This chapter explains how the subimages used for scatterer classification can be efficiently combined to approximate a conventional SAR image reconstructed from the original phase history. Alternately, it is always possible to perform SPLIT-based scatterer classification separate from conventional SAR imaging, but this is less efficient. Therefore, it is of interest to reconstruct the SAR image directly from the subimages, using domain decomposition imaging techniques. This integrated approach increases the overall computational efficiency and usefulness of SPLIT-based scatterer classification. Although domain decomposition imaging introduces some imaging error due to interpolation and subwindow summation, the error is controllable.

The discussion and evaluation of the integrated algorithm is organized as follows. Section 6.1 explains how the coarse resolution subimages are be interpolated and combined to approximate a conventional, fine resolution image. The imaging error due to interpolation is shown to be controllable, and example SAR images illustrate how the order of the imaging operator is expected to affect imaging accuracy. Section 6.2 presents subwindow design principles for approximating full band and full aperture windows used in conventional imaging. Additional analysis reveals that the imaging error due to the approximation is especially well-controlled for full 360° apertures, and $I \geq 5$ subbands. However, for other cases, some imaging artifacts may be visible. Section 6.3 introduces SAR surveillance applications and the idea of coverage area as a performance metric. It presents analysis of the computational cost of the integrated algorithm and concludes with an efficiency study using the Gotcha data set. As a result, surveillance SAR applications are given specific consideration throughout this chapter.

Figure 47 provides an overview of the integrated algorithm. Starting in the upper left-hand corner, the subaperture windows divide the phase history into J uniformly-spaced, overlapping subapertures. Next, in the upper right-hand corner, the halfband windows divide each subaperture into $I = 3$ uniformly-spaced, overlapping subbands. In the largest, dotted-line box three coarse-resolution subimages are reconstructed from the subdomains in each subaperture. Two processing paths proceed downward from the subimages. To the extreme left, the SPLIT algorithm consists of feature vector array extraction, summation, and classification, as described in Chapter V. In the center, domain decomposition imaging consists of an interpolation and weighted sum of the subimages to form a subaperture image. Then, the subaperture images are summed to form the final image. Finally, in the bottom left-hand corner, the image is annotated with scatterer classification results. The steps in the domain decomposition imaging path are discussed in more detail below.

6.1 Subimage Interpolation

This section presents a detailed interpolation operator for the integrated algorithm. The interpolation operator assumes overlapping subimages in accordance with a SPLIT-based decomposition of the phase history, as described in Chapter V. Referring to Equation 3 of Section 2.1.2.2, a discrete version of the interpolation operator is given as

$$\widehat{\tilde{g}}(\mathbf{x},\mathbf{y}) = \sum_j c_j \sum_i c_i \mathcal{I}\left\{\tilde{g}_{ij}(\mathbf{x}',\mathbf{y}';\mathbf{x},\mathbf{y})\right\}, \tag{110}$$

where $\mathcal{I}\{\cdot\}$ is the interpolation operator and the $\widehat{\ }$ symbol indicates that the result is an approximation to the fine resolution image reconstructed conventionally from the full domain of the phase history. Here, the subimage pixel coordinates are $(\mathbf{x}',\mathbf{y}')$ and the conventional image pixel coordinates are $(\mathbf{x},\mathbf{y})$. Note that in this section, images are no longer expressed as continous functions.

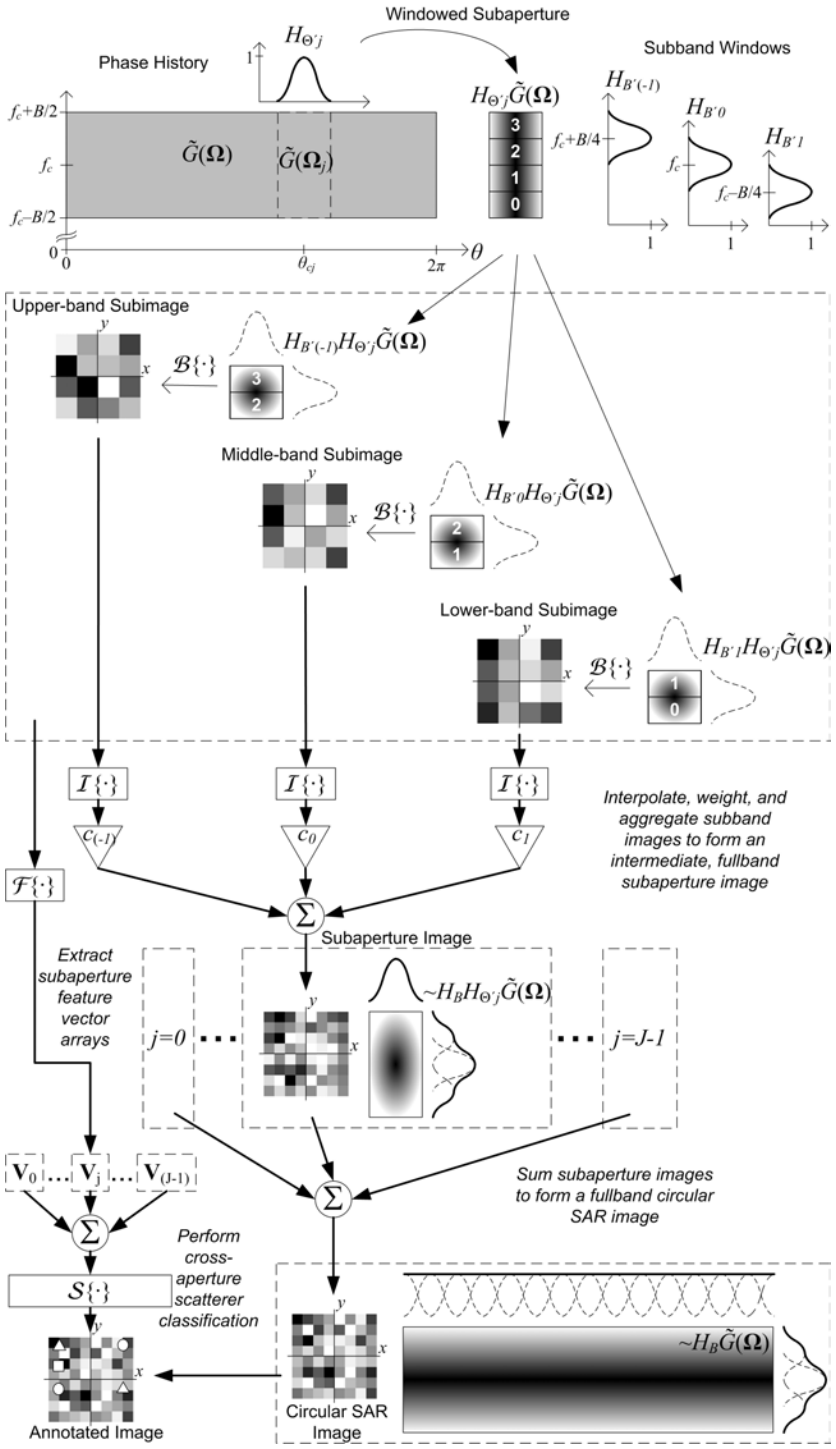

Figure 47. A detailed diagram of the integrated scatterer classification and imaging algorithm. The diagram allows visualization of the effects of subdomain windowing for a full 360° aperture and $I = 3$ subbands.

One complication of SAR image interpolation is that SAR images exhibit rapid phase variations between pixels due to the fact that SAR imagery is recovered from band limited, frequency offset data [113]. Hence, the interpolation operator must remove the rapid phase variations between subimage pixels in order to promote accurate interpolation [12]. Recall that the radar system collects samples of the scattered electric field at different aspect angles and frequencies as it moves along its flight path. For any single point scatterer in the surveillance area, the returned phase history is $\exp(-j2kd(\theta))$, where $k = 2\pi f/c$ is the wavenumber, c is the speed of light, and $d(\theta)$ is the distance to the airborne radar for a given aspect angle, θ [76]. Considering that each image pixel corresponds to a point in the surveillance area, the grid of pixel locations produces an array of distances, $\mathbf{d_{xy}}$. Thus, for a given subdomain, an array of central phase factors is given by $\mathbf{A}_{ij} = \exp(-j2k_{ci}\mathbf{d}_{\mathbf{x'y'}}(\theta_{cj}))$, where $k_{ci} = 2\pi f_{ci}/c$ is the central wavenumber of the ith subband and $\mathbf{d}_{\mathbf{x'y'}}(\theta_{cj})$ is an array of distances between the airborne radar and the pixels located at positions $(\mathbf{x'}, \mathbf{y'})$, as measured at the central angle, θ_{cj}, of the jth subaperture.

Following [12], the interpolation operator multiplies each subimage pixel array by its corresponding array of central phase factors to smooth-out the phase variations between pixels before 2D interpolation. After 2D interpolation is complete, the rapid phase variations are reestablished by multiplying by the conjugate of the array of central phase factors, $\mathbf{A^*}_{ij} = \exp(j2k_{ci}\mathbf{d_{xy}}(\theta_{cj}))$, where $(\mathbf{x}, \mathbf{y})$ are the positions of the interpolated pixels. Thus, the resultant produced by the interpolation operator, $\mathcal{I}\{\cdot\}$, is succinctly expressed as

$$\widehat{\tilde{g}}_{ij}(\mathbf{x}, \mathbf{y}) = \mathcal{I}\{\tilde{g}_{ij}(\mathbf{x'}, \mathbf{y'}); \mathbf{x}, \mathbf{y}\} = \mathbf{A^*}_{ij}\mathbf{I}\mathbf{A}_{ij}\tilde{g}_{ij}(\mathbf{x'}, \mathbf{y'}), \tag{111}$$

where $\mathbf{I}$ performs a 2D interpolation which effectively increases the sampling rate in both coordinates of the spatial domain. For example, recalling that the SPLIT

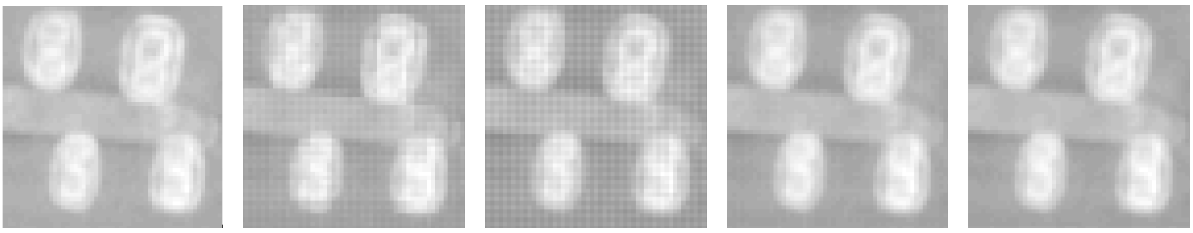

(a) Conventional Image. (b) Nearest Neighbor Interp. (c) Linear Interp. (d) Cubic Interp. (e) Ideal Interp.

Figure 48. SAR imagery for multilook conventional CBP imaging (left) and domain decomposition CBP imaging with a subaperture width $\Theta = 2°$. The order of the interpolation increases to the right. It appears that cubic interpolation is required to reduce image artifacts to an indiscernable level compared to the conventional image.

algorithm uses halfband subwindows in frequency and assuming that the full aperture is at least twice the size of the subapertures; the interpolation operator effectively doubles the sampling rate in each dimension so that the resultant has four times more pixels than the subimages. The $\widehat{\ }$ symbol in Equation (111) indicates that the interpolation operator introduces a controllable error [12].

6.1.1 Imaging Error Due to Interpolation.

The imaging error due to interpolation is controllable by increasing the amount of oversampling, increasing of the order of the interpolator, or both [12, 7]. Experience shows that for very narrow subapertures, linear interpolation is both efficient and sufficient to control interpolation error in the integrated algorithm [12]. However, for larger subapertures, higher order interpolators may be required. For example, Figure 48 shows the results of multilook images for conventional imaging and domain decomposition imaging with varying orders of interpolation. By comparing the domain decomposition images to the conventional image on the left, it is possible to visualize image artifacts. The results show that for a 2° subaperture, cubic interpolation is required to reduce image artifacts to a visually indiscernible level. In addition, Figure

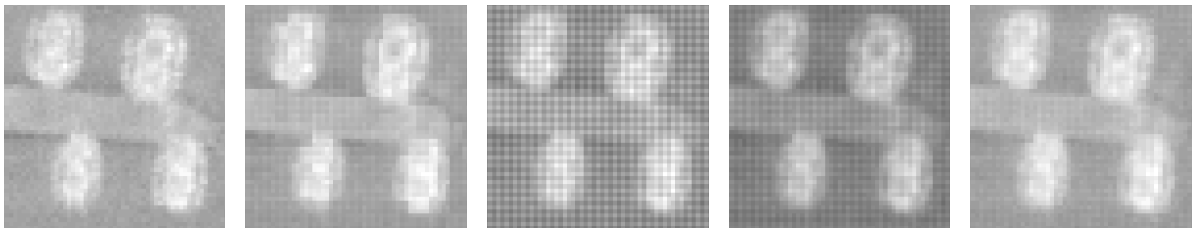

(a) Conventional Image. (b) Nearest Neighbor Interp. (c) Linear Interp. (d) Cubic Interp. (e) Ideal Interp.

Figure 49. SAR imagery for multilook conventional CBP imaging (left) and domain decomposition CBP imaging with a subaperture width $\Theta = 10°$. It appears that ideal interpolation is required to reduce image artifacts to an indiscernable level.

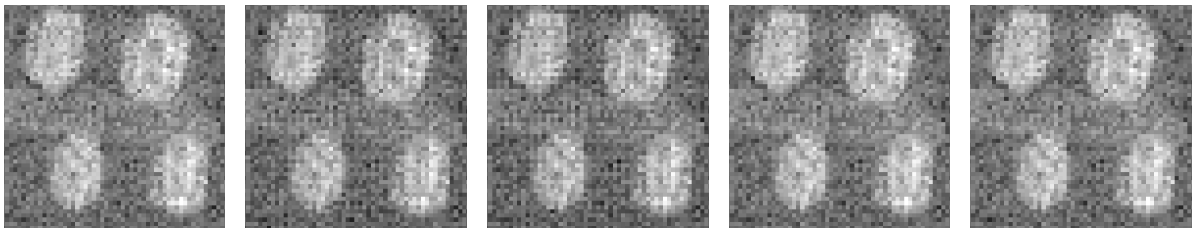

(a) Conventional Image. (b) Nearest Neighbor Interp. (c) Linear Interp. (d) Cubic Interp. (e) Ideal Interp.

Figure 50. SAR imagery for conventional CBP imaging (left) and domain decomposition CBP imaging with a subaperture width $\Theta = 2°$. It appears that even nearest neighbor interpolation may be sufficient for some applications.

49 reveals that for a 10° subaperture, ideal interpolation is required. In this case, ideal interpolation for band limited signals is performed by taking the IFFT of the zero-padded resultant of an FFT.

It turns out that coherent summation imaging, as expressed in Equation (4) of Section 2.1.2.4, may be more tolerant to interpolation error than multilook imaging, as expressed in Equation (5) of Section 2.1.2.4. For example, Figures 50 and 51 reveal that even nearest neighbor interpolation may be sufficient for some applications. Note that all domain decomposition images in this section used $I = 5$ subbands.

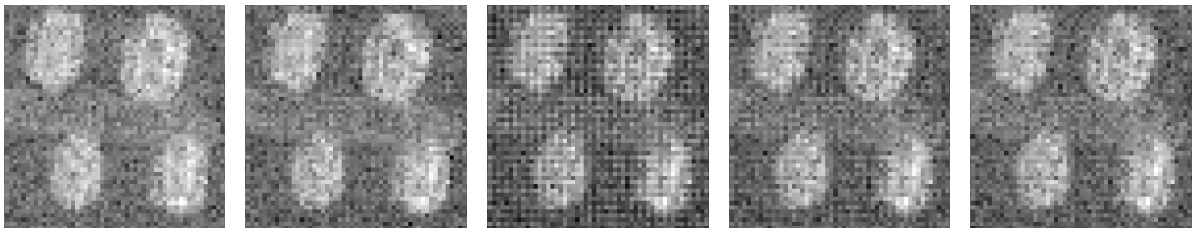

(a) Conventional Image. (b) Nearest Neighbor Interp. (c) Linear Interp. (d) Cubic Interp. (e) Ideal Interp.

Figure 51. SAR imagery for conventional CBP imaging (left) and domain decomposition CBP imaging with a subaperture width $\Theta = 10°$. It appears that even nearest neighbor interpolation may be sufficient for some applications.

6.2 Subwindow Design and Weighting

In addition, tapered subwindows in azimuth improve the sidelobe conditioning of subaperture images used in video SAR, while tapered subwindows in both azimuth and frequency provide sidelobe conditioning to improve SIR for scatterer classification. However, for the integrated algorithm, these subwindows cause artifacts in the final image when their summations do not well-approximate the desired full domain windows. The effects of data windowing can be visualized in the detailed diagram of the integrated algorithm provided in Figure 47. Fortunately, the error due to subdomain windowing is controllable through careful design and use of Hanning subwindows.

The following discussion addresses the controllable error in each spectral dimension, separately. The approximation is expressed as a summation of subwindows

$$H_{\Phi}(\xi - \xi_c) \approx \sum_{m=1}^{M} c_m H_{\Phi'}(\mu\xi + \xi_{cm}), \tag{112}$$

where $H_{\Phi}(\xi - \xi_c)$ is either the full aperture window in azimuth or the fullband window in frequency with region of support Φ. In this case, $M \in \mathbb{N}$ is the number of subwindows with region of support, $\Phi' \subset \Phi$, in that dimension. The subwindows are weighted, scaled, and shifted by $c_m \in \mathbb{R}$, $\mu \in \mathbb{R}, \mu > 1$, and $\xi_{cm} \in \mathbb{R}$, respectively.

The window error for Equation (112) is defined using the Euclidean norm,

$$\epsilon = ||H_{\Phi}(\xi - \xi_c) - \sum_{m=1}^{M} c_m H_{\Phi' m}||_2, \tag{113}$$

and is a function of the type, number, spacing, and weighting of the subwindows. For simplicity of notation, the mth shifted window is $H_{\Phi' m} = H(\mu\xi + \xi_{cm})$ from Equation (112). Because the spectral and spatial domains form a Hilbert space, a solution which minimizes the window error in the spectral domain will likewise minimize artifacts in the image [15]. Raised cosine family of window functions, such as Hanning, Hamming, and Taylor, are often used in SAR imaging [76], but other symmetric, tapered windows, such as those described in the seminal paper by Harris [67], could also be used. Because of the summation in Equation (113), the window error is best controlled when the subwindows are free of discontinuities. As an example, the Hanning window produces a low window error compared to Hamming and Taylor windows, which have a discontinuity at the boundaries of the region of support. The continuous Hanning window is a raised cosine

$$\bar{H}(\zeta) = \begin{cases} (\cos\zeta + 1)/2, & \zeta \in [-\pi, \pi], \\ 0, & \text{otherwise}, \end{cases} \tag{114}$$

where ζ is the region of support. The next two sub-subsections analyze the window error caused by using the sum of scaled, shifted, and weighted Hanning subwindows to approximate a fullband window in frequency and a full aperture window in azimuth.

6.2.1 Frequency Subwindows.

In frequency, the design goal is to approximate a fullband Hanning window of width, B, centered at f_c. Thus, the fullband Hanning window is succinctly expressed

as $H_B = \bar{H}\left(\frac{B}{2\pi}\zeta - f_c\right)$. Due to symmetry, an odd number of subwindows produces a smaller window error than does an even number of subwindows. As such, the number of subwindows, I, is equal to $2L+1, L \in \mathbb{N}$. Under these conditions, the error due to the frequency window approximation is

$$\epsilon_B = ||\bar{H}\left(\frac{B}{2\pi}\zeta - f_c\right) - \sum_{l=-L}^{L} c_l H_{B'l}||_2, \tag{115}$$

where $H_{B'l}$ are the frequency subwindows with weights, c_l. Here, the region of support for each Hanning subwindow represents a subband of the radar data. In order to obtain processing efficiency in the integrated algorithm, the subwindows in frequency are scaled to exactly half of the width of the fullband Hanning window. This choice agrees with the fast CBP algorithm presented in [12]. Although additional processing efficiency is gained by narrowing these subwindows even further, this causes a significant decrease in both classification and imaging accuracy due to the reciprocal relationship between bandwidth and resolution. As the subbands narrow, subimage resolution becomes coarser, causing decreased localization in the scattering center classifier and increased errors during subimage interpolation.

Therefore, the weighted, halfband Hanning subwindows in frequency are expressed as

$$c_l H_{B'l} = c_l \bar{H}\left(\frac{B}{4\pi}\zeta + \frac{lB}{4L} - f_c\right), \tag{116}$$

where the weights, c_l are given by the solution to the system of equations

$$\begin{bmatrix} \langle H_{B'(-L)}, H_{B'(-L)}\rangle & \cdots & \langle H_{B'(-L)}, H_{B'L}\rangle \\ \vdots & \ddots & \vdots \\ \langle H_{B'L}, H_{B'(-L)}\rangle & \cdots & \langle H_{B'L}, H_{B'L}\rangle \end{bmatrix} \begin{bmatrix} c_{-L} \\ \vdots \\ c_L \end{bmatrix} = \begin{bmatrix} \langle H_B, H_{B'(-L)}\rangle \\ \vdots \\ \langle H_B, H_{B'L}\rangle \end{bmatrix}, \tag{117}$$

where $\langle \cdot, \cdot \rangle$ denotes the inner product [120]. In summary, when designing subwindows

in frequency for circular SAR, the number is odd, the spacing is given by Equation (116), and the weights are given by Equation (117).

6.2.2 Azimuth Subwindows.

In azimuth, the error due to the azimuth window approximation is

$$\epsilon_\Theta = ||H_\Theta(\theta - \theta_c) - \sum_{j=1}^{J} c_j H_{\Theta' j}||_2. \tag{118}$$

This error is best controlled, in general, for an odd number, J, of halfway overlapping, uniformly spaced, Hanning subwindows, so that

$$J \leq \frac{2\Theta}{\Theta'} - 1. \tag{119}$$

This condition determines the scaling of the subaperture windows so that

$$c_j H_{\Theta' j} = c_j \bar{H}\left(\frac{\Theta'}{2\pi}\zeta + \theta_j\right), \tag{120}$$

where $H_{\Theta' j}$ are the frequency subwindows with weights, c_j. The weights and shifts that reduce the error due to the azimuth window approximation will depend upon the type of aperture window to be approximated.

For surveillance SAR applications or ISAR radar range measurements, 360° apertures are common. In this case, the full aperture window is flat, as shown in the bottom right-hand corner of Figure 47 of the intro to Chapter VI. Fortunately, the use of Hanning subwindows produces low window approximation error in azimuth because two equally weighted Hanning windows, shifted by a difference of π, sum to unity in the region of mutual support. This useful property is a consequence of the trigonometric relationship $(\cos\zeta + 1)/2 + (\cos(\zeta - \pi) + 1)/2 = 1$, as illustrated in

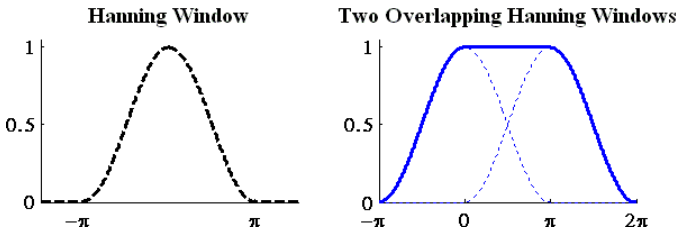

Figure 52. A Hanning window (left) has the property that the sum of equally weighted, halfway overlapping Hanning windows (right) is unity over the region of mutual support.

Figure 52. By this property, a set of properly shifted and scaled Hanning subwindows of equal weighting will sum to a flat window in azimuth. Therefore, for a flat window, $H_\Theta = 1$, $c_j = 1, \forall j$, and $\theta_j = \frac{j2\pi}{J}$ in Equations (118) and (120).

For apertures less than 360°, the full aperture window is $H_\Theta = \bar{H}\left(\frac{\Theta}{2\pi}\zeta - \theta_c\right)$. In this case, the window approximation error is best controlled when the windows are uniformly spaced by $\theta_j = \frac{j2\pi}{J+1} - \pi - \theta_c$ and when the weights follow the envelope of a Hanning window in order to mimic the envelope of the full aperture window with $c_j = \bar{H}\left(\frac{j2\pi}{J+1} - \pi\right)$. Alternately, the weights can be determined by adapting the procedure used for subwindows in frequency expressed in Equation (117).

Finally, note that for stripmap Mode SAR, the available aperture is limited by the antenna beamwidth, as described in Section 4.5. In fact, the available aperture is often so limited that only one subaperture can be used per image. In this degenerate case, $J = 1$, and no efficiency can be obtained by decomposition in the azimuth direction. However, subband windowing in frequency is still viable, and the subimages can still be weighted and summed to produce a domain decomposition image.

6.2.3 Imaging Accuracy.

In general, the imaging accuracy improves as the number of subwindows increases. For instance, frequency subwindows for the cases of $I = 3$ and $I = 5$ are depicted in Figure 53, where the window error is visually indiscernible for the case of $I = 5$. In

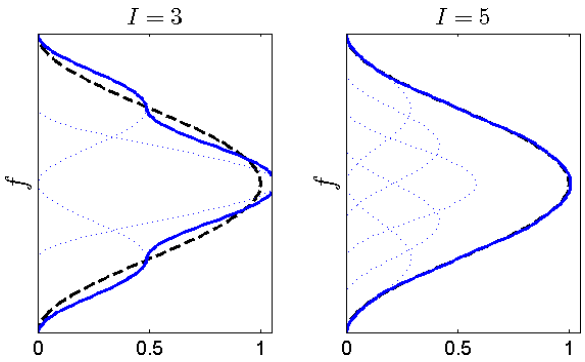

Figure 53. In frequency, a fullband Hanning window (thick, dashed line) is approximated by the sum (thick, solid line) of an odd number of weighted, shifted, halfband Hanning windows (thin, dotted lines). The weights for the narrow Hanning windows were determined using Eq. (117) for $I = 3$ (left) and $I = 5$ (right).

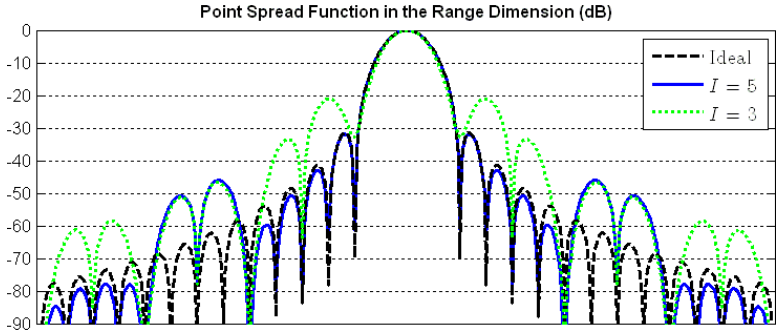

Figure 54. Point spread functions in the range dimension are oversampled to show sidelobe structure. The PSF for the case of $I = 5$ is visually similar to that of the ideal Hanning function down to approximately -40 dB. In contrast, the PSF for the case of $I = 3$ is only visually similar down to approximately -20 dB.

order to determine how the window approximation error will affect the image, it is helpful to calculate the point spread function (PSF). The PSF predicts the response of a single, isotropic, non-distributed, non-dispersive scatterer located at the zero-phase reference. In other words, it illustrates how an ideal point scatterer located in the center of the image will appear. The PSF in the range dimension is simply the absolute value of the inverse discrete Fourier transform of $H_B(f)$ [76]. Figure 54 compares the ideal PSF for a Hanning window to the PSFs for the approximated Hanning windows when $I = 5$ and $I = 3$. For the case of $I = 5$, the PSF is visually

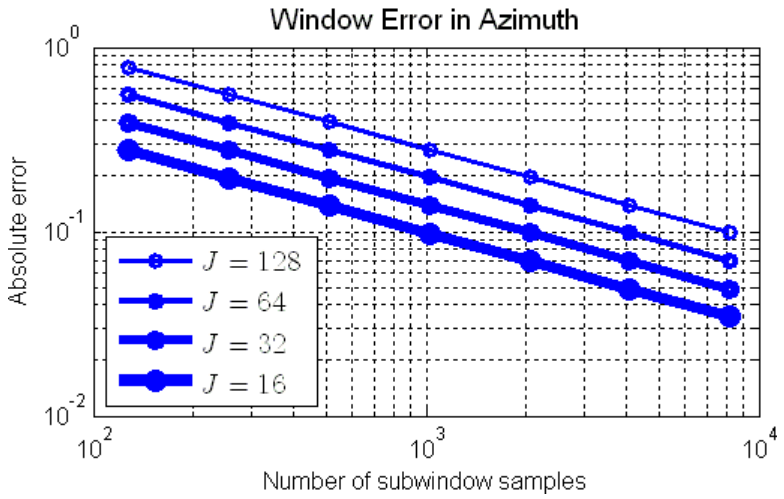

Figure 55. The window approximation error in azimuth using discrete Hanning subwindows. For a given aperture, fewer subwindows results in more digital samples per subwindow.

similar down to approximately -40 dB, but for the case of $I = 3$, this is only true down to approximately -20 dB. As a result, the circular SAR image artifacts due to window error in frequency for the integrated algorithm are likely to be visually indiscernible for the case of $I = 5$, but may be noticeable for the case of $I = 3$. Section 6.2.3.1 presents empirical evidence to support these predictions.

For the case of approximating a flat window in azimuth, the window error in azimuth is zero for continuous Hanning subwindows, that is $\epsilon_\Theta = 0$. Consequently, for the case of discrete Hanning subwindows, the window error approaches zero as the number of samples for each subwindow approaches infinity. Figure 55 illustrates this with results produced using the `hanning` function in Matlab®. For a given aperture, fewer subwindows results in more digital samples per subwindow. Note also how the absolute window error decreases as the number of samples for each of the Hanning subwindows increases. A typical implementation of the integrated algorithm features dozens of subapertures, each with hundreds of samples. In this case, the per sample window error in azimuth is very low, and the resulting image artifacts are likely to

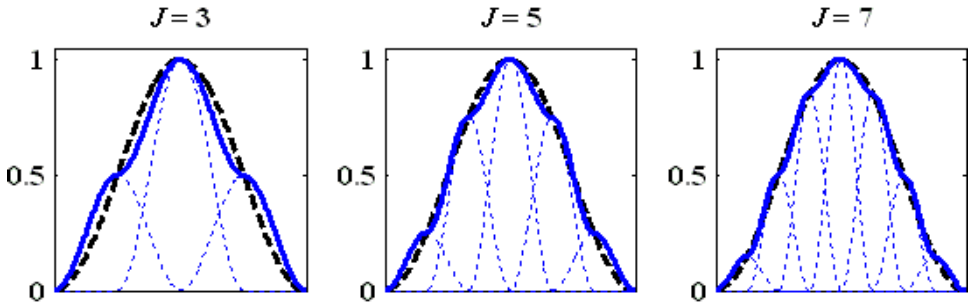

Figure 56. In azimuth, a wide Hanning window (thick, dashed line) can be approximated by the sum (thick, solid line) of an odd number of weighted, shifted narrow Hanning windows (thin, dotted lines). The approximation error is reduced as the number of narrow windows, J, increases.

be visually indiscernible. Section 6.2.3.1 presents empirical evidence to support this prediction.

In contrast, for the case of approximating a Hanning window in azimuth, the imaging accuracy will improve as the number of subwindows increases, as indicated in Figure 56. The PSFs for this case are shown in Figure 57. Note, that there must be at least $J = 7$ subwindows in order to keep the sidelobes in azimuth below -30 dB. Recall that the wide-angle approximation in the multi-peak model requires $\Theta' \gtrsim 10°$. Also note that according to Equation (119), a full aperture of 40° is required in order to create $J = 7$ subapertures of width $\Theta' = 10°$ each. This suggests that the integrated algorithm requires a very wide aperture, $\Theta \gtrsim 40°$, in order to reduce image artifacts to a visually indiscernible level.

Last, note that the subwindow design principles presented earlier are not unique to Hanning windows and are easily adapted for use with other types of windows. However, it's worth restating that windows with no discontinuities, such as the Hanning window, produce a lower window error than other popular windows which feature discontinuities, such as Hamming and Taylor windows.

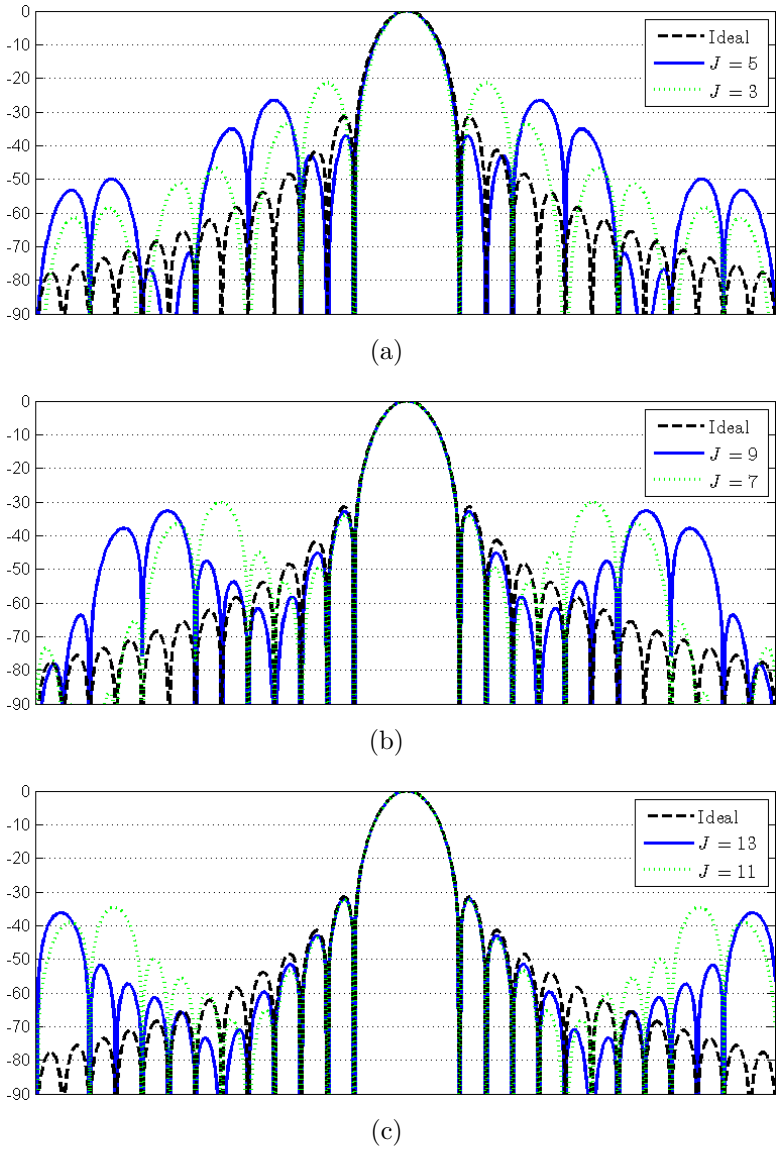

Figure 57. The PSFs in the cross-range dimension are oversampled to show sidelobe structure. The sidelobe levels in cross-range are reduced as the number of subaperture windows, J, increases.

6.2.3.1 Empirical Studies of Imaging Accuracy.

This section compares the imaging accuracy of the integrated algorithm to that of conventional CBP for a surveillance SAR application. As previously discussed, an image produced by the integrated algorithm contains image artifacts due to errors in interpolation and window approximation. Additional analysis revealed that the errors

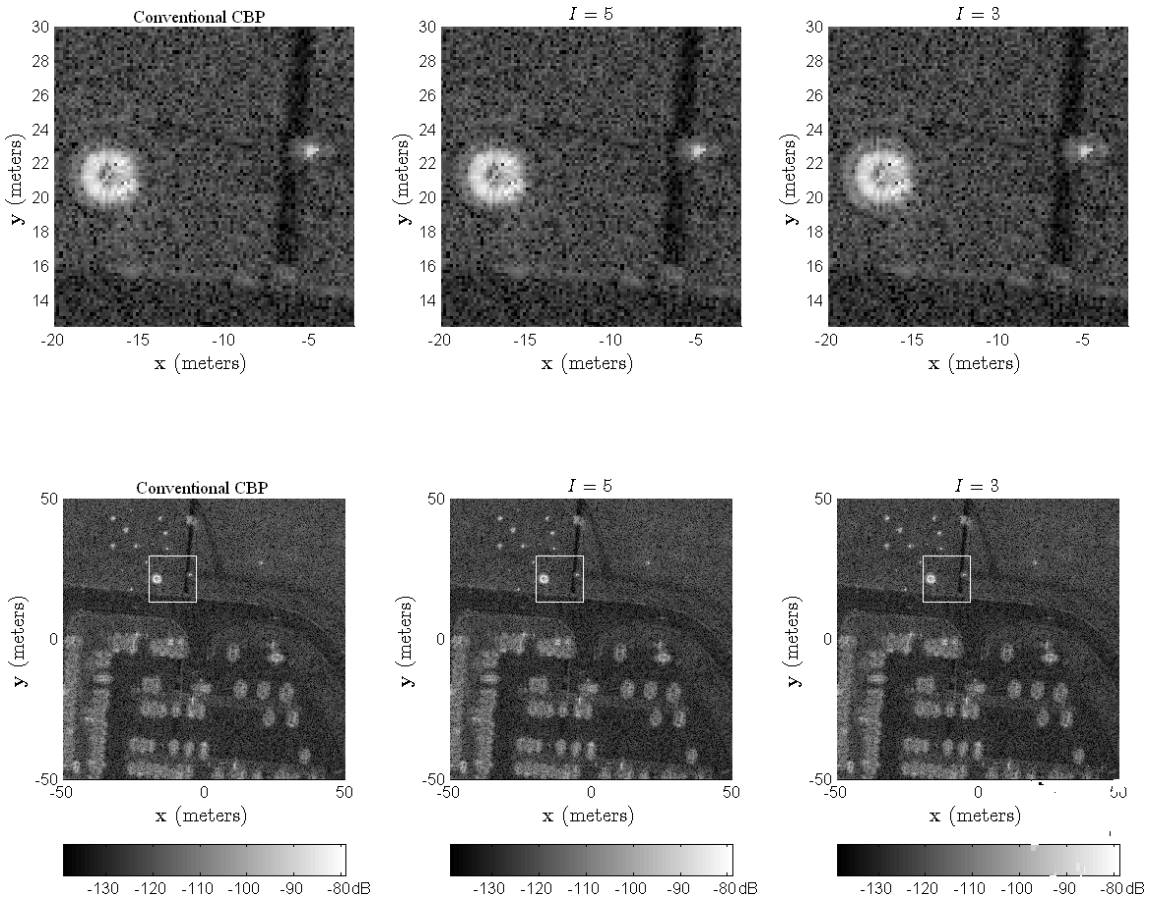

Figure 58. SAR images of a parking lot scene (bottom row) with call-out boxes featuring top-hat and dihedral calibration targets (top row). The images produced by conventional CBP (left column) serve as a baseline for evaluating the imaging accuracy of the integrated algorithm. The errors introduced by the integrated algorithm for the case of $I = 5$ (middle column) are imperceptible. However, the errors introduced for the case of $I = 3$ (right column) cause a visible increase in sidelobe energy, which causes the appearance of a slightly stronger and broader halo around objects with high scattering intensity.

were quite small and likely to be visually indiscernible for the case of a flat window in azimuth and $I = 5$ subbands. However, for the case of $I = 3$, the error due to window approximation in frequency is appreciable and is likely to be noticeable due to increased PSF sidelobes. The following examples verify these conclusions empirically.

Figure 58 shows SAR images of the Gotcha data described in Table 15 of Section 5.4.4. Note that the aperture is 360° so that a flat aperture window is approximated in azimuth. For brevity, only the data from the horizontal transmit, horizontal receive

(HH) channel is shown. Also, in order to emphasize differences between imaging methods, a coherent subaperture sum with 2× oversampling is used. The SAR images are reconstructed using conventional CBP, the integrated algorithm with $I = 5$, and the integrated algorithm with $I = 3$. The call-out boxes in the top row reveal additional detail for the top hat and one trihedral taken from the full-scene images in the bottom row. By using the conventional CBP images (left column) as a baseline, one can visually confirm the impact of the image artifacts introduced by the integrated algorithm. For the case of $I = 5$ (middle column), the artifacts are imperceptible, and the images in the left and middle columns are virtually identical. In contrast, for the case of $I = 3$ (right column), some image artifacts are noticeable. The increase in PSF sidelobe energy causes a slightly stronger and broader halo to appear around objects with high scattering intensity. As a result, some of the pixel values are visibly different when compared to conventional CBP, especially those in the center and along the edge of the top hat and those surrounding the trihedral. Similar results (not shown) were obtained for varying amounts of oversampling in the integrated algorithm.

Results in Figure 58 are valuable for analyzing the usefulness of the integrated algorithm and for gaining practical insight into the engineering trade space between imaging accuracy and processing efficiency. For the case of $I = 5$, the imaging accuracy is very good and any processing gain makes it a superior choice to conventional CBP. However, for the case of $I = 3$, the SAR system engineer must evaluate the noticeable loss in imaging accuracy against the benefits of associated processing gain. The cases for $I > 5$ are not presented because the processing cost increases linearly with no appreciable improvement in imaging accuracy. The next section analyzes the processing cost of the integrated algorithm and demonstrates its potential efficiency.

6.3 Efficiency Study

Scattering center classification by phase history decomposition is operationally efficient when compared to existing image segmentation methods. This is because image segmentation requires human supervision, as discussed in Sections 1.2 and 3.1. Although the expected gains in operational efficiency are likely to be substantial, these are difficult to analyze mathematically. In contrast, the computational efficiency gains afforded by the integrated algorithm are more readily analyzed.

The integrated algorithm allows gains in computational efficiency with a controllable reduction in imaging accuracy. Use of this trade-space is desirable for highly resource constrained scenarios, such as SAR surveillance applications. Imaging accuracy was discussed in the preceding sections, while computational efficiency is discussed in this section. The section begins by introducing the concept of SAR surveillance and the processing constraints that limit maximum coverage area. Then, it presents analytical analysis of the expected efficiency of the integrated algorithm assuming a convolution backprojection imaging algorithm. Finally, it uses coverage area as a metric, to present empirical studies of computational efficiency for the integrated algorithm.

6.3.1 SAR Surveillance.

SAR systems are useful for wide-area surveillance, provided that these systems can produce images in near real-time [118, 18, 99, 25]. Example applications include all-weather, day and night monitoring of borders, roads, or cities to protect populations from illicit activities. As a result of the growing demand for SAR surveillance imagery, developers of airborne SAR systems have begun to incorporate a extensive circular SAR modes into their designs [23, 22, 35, 151, 89]. Surveillance via circular SAR imaging is depicted in Figure 2 of Section 2.1.1. The operating parameters

and capabilities of specific surveillance SAR systems vary, but typical performance parameters include a resolution of 0.15-m to 0.5-m and a coverage area of 0.5-km^2 to 1-km^2. Current efforts seek to increase the available coverage area for a given resolution under time and resource constraints. The maximum coverage area depends on the complexity of the imaging algorithm, the speed of the image processor, and the computational burden for optional post-processing of the SAR data, and serves as the performance metric for the efficiency studies in Section 6.3.3.

First, coverage area depends upon the complexity of the imaging algorithm. The imaging algorithms suitable for circular SAR are CBP and PFA [76]. In theory, both algorithms produce equivalent images with controllable error [82]. Furthermore, for an image consisting of $N \times N$ pixels, each has a computational complexity of $O(N^2 \log N)$ when fast Fourier transforms and fast CBP techniques are considered [103, 12]. Last, both algorithms are scalable to allow accelerated processing through distributed and parallel architectures [82, 68]. However, despite these and other general similarities, CBP has one significant advantage over PFA: it allows for greater flexibility in selecting the image pixel locations and spacing, which can be used to focus the image to a previously-obtained digital elevation map [76, 40]. For this reason, the CBP algorithm is generally preferred in surveillance SAR applications, where the desired imaging plane often varies significantly with changes in aspect angle. The computational complexity varies from $O(N^3)$ for conventional CBP to $O(N^2 \log N)$ for fast CBP techniques, depending upon the implementation. As imaging algorithms are mature, significant increases in real-time (or near real-time) coverage area will be achieved by increased processing capability and efficiency.

Second, coverage area depends upon the speed of the image processor. Advances in parallel processors have lowered cost and increased performance of near real-time SAR imaging systems [65, 68, 41]. However, the coverage area of current systems is still

quite limited. For example, Gorham *et al.* reported on the processing time required to produce circular SAR images using a specialized processor suitable for surveillance aircraft [65]. The processor produces a 2048 × 2048-pixel circular SAR image for one polarization channel in approximately 23 seconds. This provides a 0.25-km^2 coverage area for a single polarization channel at 0.25-m resolution. Assuming systematic scaling, the processor produces a fully-polarized circular SAR image with similar resolution over a 4-km^2 coverage area in approximately 45 minutes. For comparison, a separate implementation using four graphics processing units produces the same result in approximately 90 minutes [68]. Because a typical airborne radar system circumnavigates its entire flight path in under 45 minutes, a 4-km^2 coverage area exceeds what these solutions can provide in real-time. As processing advances are incremental, even with fast imaging algorithms, increases in real-time coverage area are expected to remain incremental.

Third, the information within the coverage area depends upon the computational burden for optional post-processing of the SAR data. Upon receipt of a SAR image, an analyst must subsequently scrutinize the image, but often requires automatic analysis tools to meet time constraints. The time required for image analysis is difficult to parameterize. However, it is generally accepted that people can better prioritize surveillance resources and improve image analysis with the aid of additional SAR data processing [116]. Proposed methods range from simple scatterer filters or classifiers, which help identify regions containing objects of interest, to automatic target classifiers, which provide specific target information [116]. While the advantages and limitations of such classifiers vary, almost all of them execute significant amounts of signal processing *after* a SAR image is formed [116]. For instance, some advanced methods employ iterative model-matching techniques, which require repetitive imaging of the scene [101, 122]. In addition, many signal estimation methods require

evaluation of a full-rank correlation matrix, which drives computational complexity as high as $O(N^6)$ [39]. Unfortunately, a dramatic increase in processing costs occurs when such classifiers are appended to a SAR imaging process. While researchers often propose efficient implementations for classifiers with high orders of computational complexity, these are tailored to the particular classifier, and research to survey the processing costs of all such classifiers is nascent. As a result, current evaluations of the near-real time capability of circular SAR systems do not usually consider optional post-processing of the SAR data as part of the equation. Therefore, advances in optional post-processing of the SAR data alone have not translated into increased coverage area for circular SAR systems, to date. However, the integrated algorithm has the potential to reduce or even eliminate the post-processing costs of some classifiers and produce a significant increase in coverage area for circular SAR systems, as discussed in Sections 1.2 and 3.1.

6.3.2 Analysis of Computational Cost.

Because domain decomposition imaging has a lower order of computational complexity than conventional CBP imaging, the integrated algorithm has the potential to produce a SAR image annotated with scatterer classification in less time than it takes to produce the same image by conventional CBP, without scatterer classification. This section analyzes the computational costs of both the integrated algorithm and conventional CBP to determine under what conditions this efficiency is achieved.

A first-order analysis of computational cost scales linearly with an increase in the number of available polarization channels. Therefore, the following analysis is restricted to a single polarization channel. Also, to facilitate discussion, primed mathematical constants refer to the integrated algorithm, while unprimed constants refer to conventional CBP. Note that the equation for conventional CBP imaging using

overlapping subapertures is given by Equation (4) of Section 2.1.2.4, whereas the integrated algorithm uses phase history decomposition as expressed in Equation (3) of Section 2.1.2.2. For both, the imaging operator has a computational complexity of $O(N^3)$ for an $N \times N$ image, while other processes have a computational complexity of $O(N^2)$ [76].

The computational cost for CSAR image formation by conventional CBP is

$$\text{Cost} = J(bN^3 + sN^2), \tag{121}$$

where b is an unspecified coefficient for the imaging operator and s is an unspecified coefficient for other processes. These $O(N^2)$ processes include subaperture image summation and various data conditioning operations. Examples of data conditioning operations are two-dimensional (2D) windowing of the subaperture data and computation of pixel intensities for use in displaying an image.

In contrast, the integrated algorithm creates potential savings by producing subimages that are $\frac{N}{2} \times \frac{N}{2}$ in size while adding an additional 2D interpolation process and a feature extraction process both of which are $O(N^2)$. The number of subimages is $I \times J$, and the computational cost to produce an annotated CSAR image using the integrated algorithm is

$$\text{Cost}' = IJ' \left(b' \left(\tfrac{N}{2}\right)^3 + s' \left(\tfrac{N}{2}\right)^2 + a' \left(\tfrac{N}{2}\right)^2 \right), \tag{122}$$

where a' is an unspecified coefficient which accounts for the additional 2D interpolation and feature extraction processes, and where b' and s' are the fast CBP counterparts to b and s.

Assuming overlapping subapertures and subimage dimensions with equal resolution, the widths of the subapertures for conventional CBP are twice the width of

the subapertures for the integrated algorithm. This occurs because the integrated algorithm recovers subimages from halfband data, where $B' = \frac{B}{2}$. As a result, the integrated algorithm requires twice as many subaperture images as does conventional CBP, and $J' = 2J$. It can be shown under the preceding assumptions, that the relationship

$$N > \frac{2I(s' + a') - 4s}{4b - Ib'} \quad \Longrightarrow \quad \text{Cost}' \lessapprox \text{Cost} \tag{123}$$

holds. When $I \geq 3$, the numerator is likely to be positive. Therefore, as long as $4b > Ib'$, there exists some threshold, $N > N_{thresh}$, at which the cost of integrated algorithm is less than conventional CBP. The conditions which cause the denominator of (123) is positive, warrant further scrutiny. Intuitively, it seems safe to assume that $b \geq b'$ because the subimages are of a coarser resolution for the integrated algorithm. Based on this assumption, N_{thresh}, exists for the case of $I = 3$. However, it is unclear whether or not N_{thresh} exists for the case of $I \geq 5$. In general, N_{thresh} must be determined empirically because a', b, and b' are unspecified. For instance, b is affected by the computational complexity of the interpolation in the imaging operator, $\mathcal{B}\{\cdot\}$, while a' is affected by the computational complexity of the 2D interpolation in the interpolation operator, $\mathcal{I}\{\cdot\}$.

In summary, first-order comparison of the computational cost of the integrated algorithm to that of conventional CBP showed that for large, high-resolution images with large N, the integrated algorithm has a lower processing cost than conventional CBP for the case of $I = 3$, but not necessarily for the case of $I \geq 5$. In addition, the integrated algorithm produces scatterer classification information, whereas conventional CBP does not. The next section presents empirical studies of the net computational savings and imaging accuracy of the integrated algorithm.

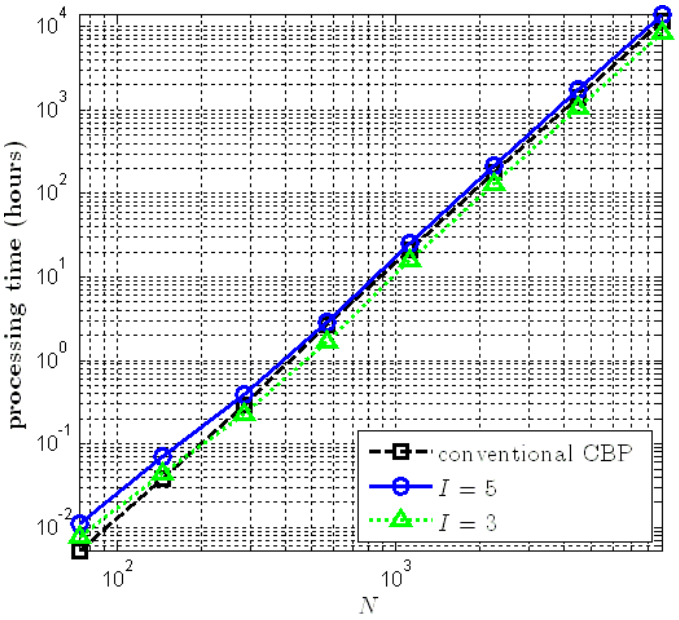

Figure 59. Processing times required to produce a circular SAR image. For large N, conventional CBP has a higher processing cost than the integrated algorithm for the case of $I = 3$.

6.3.3 Empirical Studies of Processing Efficiency.

This section evaluates the processing efficiency of the integrated algorithm, as compared to conventional CBP. The discussion in Section 6.3.2 revealed that there is a theoretical image size, $N > N_{thresh}$, above which the integrated algorithm has a lower processing cost than conventional CBP. Additional analysis revealed that this threshold exists for the case when $I = 3$, but it is unclear if it exists for the case when $I = 5$. The following examples verify these conclusions empirically.

For near real-time surveillance, the time required to produce an $N \times N$ image is of interest. The following empirical studies use the Gotcha data set described in Table 15 of Section 5.4.4 to simulate a SAR surveillance scene. To simulate different values of N, the number of samples in the Gotcha data set is adjusted by an appropriate amount of decimation or interpolation. Based on this procedure, Figure 59 reports the processing times for a series of simulations of varying image sizes. The longer

run-times were approximated by processing only a portion of the data set. For the case of $I = 3$, the integrated algorithm has a lower processing time than conventional CBP for $N \gtrsim 200$. In contrast, for $I = 5$, the integrated algorithm always has a higher processing time than conventional CBP. For large N, all three curves display a computational complexity of $O(N^3)$, as expected. These simulations were conducted using a 64-bit version of Matlab® on a quad-core Intel® Xeon® 5160, 3-GHz processor.

A useful metric for evaluating the integrated algorithm in a time constrained scenario is the amount of coverage area either gained or lost, as compared to conventional CBP. Figure 60 presents this comparison for the three cases shown in Figure 59. To construct Figure 60, it is noted that the curves in Figure 59 were interpolated by a piecewise cubic hermite interpolating polynomial provided in the `pchip` function of Matlab®. Based on this procedure, Figure 60 shows the estimated coverage area for the integrated algorithm as a percent of the coverage area for conventional CBP. The coverage area for the integrated algorithm is approximately 20-percent greater than conventional CBP for the case of $I = 3$ and about 10-percent less than conventional CBP for the case of $I = 5$.

The best results for the integrated algorithm occur for $N \approx 565$, and so the performance of the algorithm near this operating point deserves additional evaluation. Of particular interest from Equation (122) is the condition under which $4b > 5b'$, where the processing cost of conventional CBP is greater than the processing cost of the integrated algorithm (shown for the case of $I = 5$). The relationship between b and b' is primarily affected by the processing cost of the one-dimensional (1D) interpolation in the imaging operator. For each backprojection, the image pixels accumulate interpolated samples of the 1D range-compressed, filtered radar data [76]. In order to obtain acceptable imaging accuracy and efficiency, the imaging operator

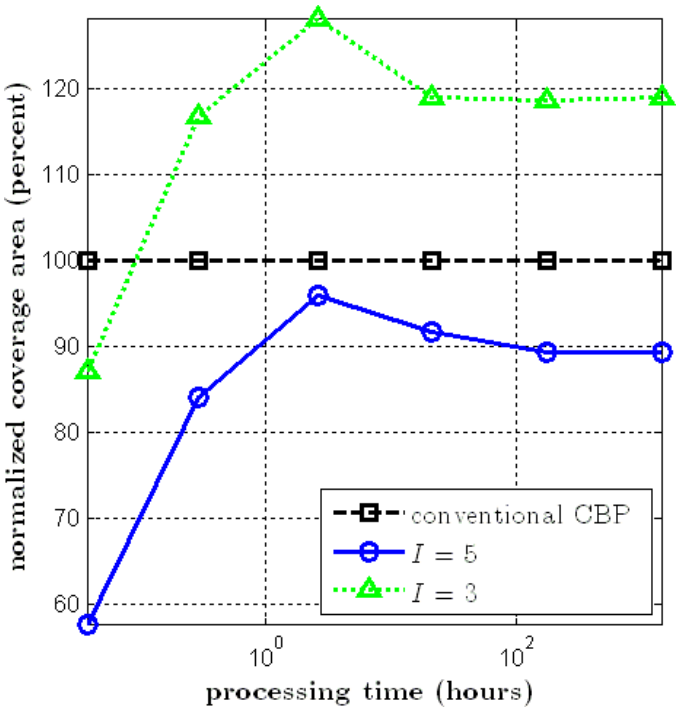

Figure 60. Estimated circular SAR coverage areas for the integrated algorithm as a percent of the coverage area for conventional CBP. For large N, where processing times are large, the integrated algorithm provides approximately 20-percent more coverage than conventional CBP when $I = 3$, and it provides approximately 10-percent less coverage when $I = 5$.

usually performs 1D interpolation by a two-step process of ideal sinc interpolation followed by a much less computationally complex linear interpolation [64]. In practice, ideal sinc interpolation is accomplished by zero-padding the radar data in the spectral domain before performing an IFFT to obtain an oversampled signal in the spatial domain. Typically, the amount of oversampling is on the order of 10×, or more [64, 135]. For instance, approximately 9× oversampling was used in these studies.

Additional experiments revealed that simply reducing oversampling in both conventional CBP and the integrated algorithm to 4× caused the computational cost of traditional CBP to become nearly equivalent to the processing cost of the integrated algorithm for the case of $I = 5$ and $N = 565$. However, reducing oversampling to such a low amount produced image artifacts that are usually undesirable. Therefore,

these studies suggest that for typical SAR surveillance implementations, the processing cost for conventional CBP will be less than the processing cost for the integrated algorithm for the case of $I = 5$.

Finally, note that these efficiency studies assumed that the integrated algorithm required twice as many subaperture images as conventional CBP, where $J' = 2J$ in Equation (123). If this requirement is relaxed, so that the subaperture width for the integrated algorithm is equal to that for conventional CBP, then computational efficiency will improve. However, the efficiency is not likely to double when $J' = J$ because larger subapertures may demand a higher order interpolator, as discussed previously in Section 6.1.1. However, when $J' = J$, it is likely that there exists a threshold, N_{thresh}, whereby the coverage area is larger for both cases of $I = 3$ and $I = 5$ when compared to the coverage area for conventional CBP.

VII. Conclusion

In conclusion, this dissertation presented a new theory for SAR scatterer classification by phase history decomposition. More specifically, the hypotheses presented in Section 3.2 have been proven. First, canonical scatterers can be located and classified in subimages. This is accomplished using the multi-peak model and SPLIT algorithm. Second, the process is efficient. Operational efficiency is improved by eliminating the need for human supervision associated with existing scatterer classification methods based on image segmentation. Furthermore, computational efficiency is improved through use of the integrated algorithm.

The benefits of the new theory are significant. First, it provides a solid theoretical basis by which to predict imaging and classification performance. Second, it is flexible, with a controllable efficiency *versus* accuracy trade-space that can be used to optimize desired performance for resource constrained scenarios. Third, the new theory provides a general tool for queuing analysts or precision algorithms for high precision, post-processing of SAR images. Finally, note that this research has resulted in the publication of three conference papers, the submission of two journal articles, and the production of computer programs for use with real SAR data.

7.1 Notable Limitations

While there are many significant benefits of the new theory for SAR scatterer classification by phase history decomposition, there are some notable limitations to keep in mind as well. The notable limitations of the multi-peak model are listed in decreasing order of importance. First, model accuracy is limited by a wide-angle approximation that restricts apertures or subapertures to be greater than or equal to 10°. Fortunately, wide-angle SAR imaging systems do exist and their continued

development makes wide-angle SAR applications likely to be common in the future. Second, for stripmap SAR applications, the multi-peak model is restricted for use with the Omega-K algorithm. Fortunately, the Omega-K algorithm is mature and even commonly used for P-band stripmap SAR systems. Third, also for stripmap SAR, the multi-peak model is accurate for scatterers with effective lengths greater than or equal to 1.6 times the physical length of the antenna. Fourth, a small-angle approximation restricts the multi-peak model to apertures or subapertures less than 20° for rectangularly formatted phase histories. Although rectangularly formatted phase histories are very common for spotlight mode SAR, this restriction is already often observed, in practice. Fifth, the multi-peak model is limited by a high-frequency approximation for perfect electrical conductors in the far field. In particular, this requires that the effective length of scatterer to be ten wavelengths long or longer. Fortunately, these conditions are met for many objects of interest in typical SAR applications. Furthermore, these restrictions are common among existing scatterer models and classification methods, and therefore, are not unique to the multi-peak model. Sixth, the multi-peak model requires the use of a tapered window in azimuth. Fortunately, windowing of the phase history is already a common practice in SAR imaging.

The notable limitations of the SPLIT algorithm are listed in decreasing order of importance. First, classification accuracy is limited by subimage resolution, which is half of the system resolution. The SPLIT algorithm obtains the required spectral information by reducing spatial resolution. As expected, such trade-offs are unavoidable in SAR image processing due to the principle of time-frequency reciprocity. Second, the SPLIT algorithm is generally inaccurate for fractional bandwidths below 10-percent. The SIR due to neighboring scatterers must be well-controlled to ensure good classification accuracy. Experimental results indicate that a fractional

bandwidth of at least 10-percent is needed to reduce the SIR for typical man-made structures. Third, the least squares classifier is not optimized for clutter or interference limited scenarios. It is well-suited for classifying canonical scatterers on simple targets in free-space, but when interference from neighboring strong scatterers or clutter are a concern, the performance of the least squares classifier is expected to be suboptimal. Fourth, the SPLIT algorithm requires a normalized phase history. Fortunately, the necessary normalization factors are typically available for most SAR systems. Fifth, the SPLIT algorithm assumes a stationary scattering center. As expected, some objects, such as resonant cavities, and moving vehicles or windmill blades appear unfocused in the SAR image. Fortunately, these objects are typically rejected by SPLIT algorithm using the stable peak criterion and are not expected to cause undue confusion in the classifier.

There are three notable limitations of the integrated algorithm. Fortunately, if these limitations prove unacceptable in practice, then scatterer classification can be accomplished separately and results can be overlaid on a SAR image reconstructed using a conventional imaging process. First, rapid phase variations in the subimages require either a high order interpolator or restricted subdomain in order to reduce image artifacts to imperceptible levels. Second, the integrated algorithm is limited to the use of Hanning windows to limit discontinuities which increase window approximation error. Third, the window approximation error can introduce noticeable image artifacts for apertures under 40° and a number of subbands less than five.

7.2 Future Work

This dissertation creates a solid foundation for future research in the following areas. First, recent trends in legal restrictions on use of the electromagnetic spectrum have spurred interest in SAR collections over discontinuous frequencies. Fortunately,

the new theory in this dissertation can be extended for use with discontinuous phase histories, as needed. Second, classification accuracy can be improved beyond that of a least squares classifier by use of standard signal detection and estimation techniques. For example, the use of generalized likelihood ratio tests for specific scenarios could be of interest. Alternately, adaptive filters for clutter cancellation can be incorporated into the algorithm. Third, the theory can be extended beyond monostatic, 2D SAR to include 3D SAR and bi-static SAR. Fourth, domain decimation imaging featuring a mosaic of subimages can provide computational efficiency equivalent to domain decomposition imaging. These techniques can be blended rather easily, but the effect on classification accuracy is uncertain and would need to be researched. Finally, there are potentially additional uses for related versions of the multi-peak model and SPLIT algorithm in other topics and areas of research, such as the CLEAN algorithm modified by the stable peak criterion [53, 100, 141].

Appendix A. AFIT Indoor RCS Measurement Range

The AFIT indoor RCS measurement range consists of a large anechoic chamber, target support system, and a radar system featuring a Lintek gating box. Specific information regarding these systems can be found in the course notes for EENG 627 - RCS Analysis, Measurement, and Reduction [34]. Diagrams of the range are provided in Figure 61.

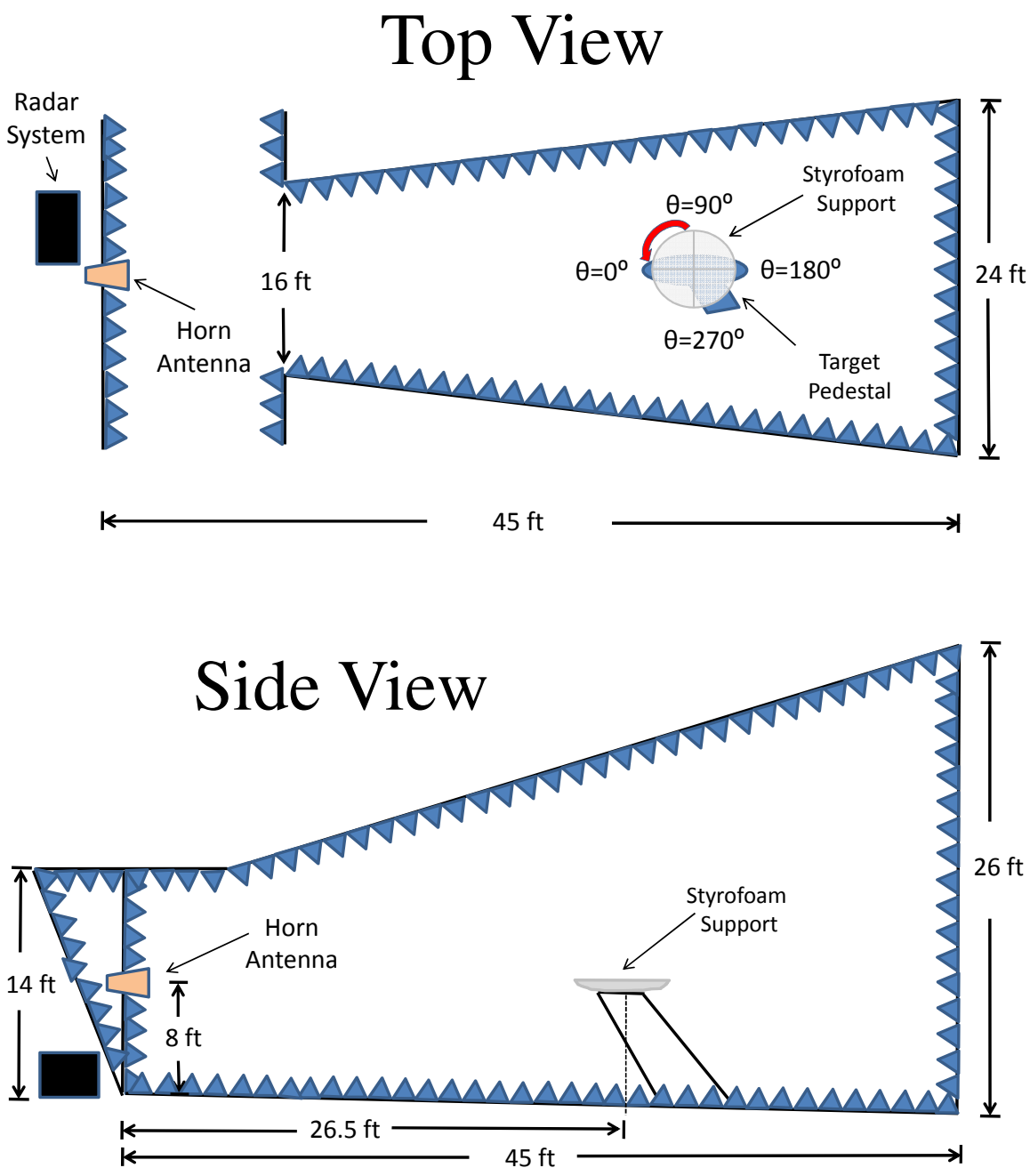

Figure 61. AFIT indoor RCS measurement range [104].

Bibliography

[1] Ainsworth, T.L. and J.S. Lee. "Polarimetric SAR image classification employing subaperture polarimetric analysis". *Proc. IEEE Geosci Remote Sens. Symposium*, volume 1. July 2005.

[2] Ainsworth, T.L., D.L. Schuler, and J.S. Lee. "Polarimetric SAR characterization of man-made structures in urban areas using normalized circular-pol correlation coefficients". *Remote Sens. Environ.*, 112(6):2876–2885, 2008.

[3] Akyildiz, Y. *Feature Extraction from Synthetic Aperture Radar Imagery*. Master's thesis, The Ohio State University, Columbus, OH, 2000.

[4] Antkoviak, J.L. *Uncertainty Estimate for a Near Field to Far Field Transform Algorithm*. Master's thesis, Air Force Institute of Technology, Wright-Patterson AFB, OH, 2009.

[5] Bajcsy, P. and A.R. Chaudhuri. "Benefits of high resolution SAR for ATR of targets in proximity". *Proc. IEEE Radar Conf.*, 29–34. Long Beach, CA, Aug 2002.

[6] Balanis, C.A. *Advanced Engineering Electromagnetics*. John Wiley and Sons, New York, NY, 1989.

[7] Basu, S. and Y. Bresler. "Error analysis and performance optimization of fast hierarchical backprojection algorithms". *IEEE Trans. Image Process.*, 10(7):1103–1117, 2002.

[8] Baum, C.E. *Detection and Identification of Visually Obscured Targets*. Taylor and Francis, Philadelphia, PA, 1998.

[9] Baum, C.E., E.J. Rothwell, K. Chen, and D.P. Nyquist. "The singularity expansion method and its application to target identification". *Proc. IEEE*, 79:1481–1492, 1991.

[10] Björck, Å. *Numerical Methods for Least Squares Problems*. Society for Industrial Mathematics, Philadelphia, PA, 1996.

[11] Blumer, A., A. Ehrenfeucht, D. Haussler, and M.K. Warmuth. "Occam's razor". *Inf. Process. Lett.*, 24:377–380, 1987.

[12] Boag, A. "A fast multilevel domain decomposition algorithm for radar imaging". *IEEE Trans. Antennas and Prop.*, 49(4):666–671, 2001.

[13] Board, Naval Studies. *Technology for the United States Navy and Marine Corps, 2000-2035. Volume 2: Technology*. Technical report, National Academy Press, Washington, DC, 1997.

[14] Borden, B. "Problems in airborne radar target recognition". *Inverse Prob.*, 10:1009–1022, 1994.

[15] Borden, B. *Radar Imaging of Airborne Targets: a Primer for Applied Mathematicians and Physicists*. Taylor & Francis Group, New York, NY, 1999.

[16] Brigui, F., L. Thirion-Lefevre, G. Ginolhac, and P. Forster. "New polarimetric signal subspace detectors for SAR processors". *Comptes Rendus Physique*, 11(1):104–113, 2010.

[17] Brisco, B., R. Touzi, J.J. van der Sanden, F. Charbonneau, T.J. Pultz, and M. DIorio. "Water resource applications with RADARSAT-2–a preview". *Int. J. Digital Earth*, 1(1):130–147, 2008.

[18] Bryant, M.L. "Multisensor staring exploitation". *Proc. SPIE Defense Transformation and Net-Centric Syst.*, volume 6981. Orlando, FL, Apr 2008.

[19] Bryant, M.L., P. Johnson, B.M. Kent, M. Nowak, and S. Rogers. *Layered sensing: Its definition, attributes, and guiding principles for AFRL strategic technology development*. Technical report, Air Force Research Laboratory, Wright-Patterson AFB, OH, 2008.

[20] Cameron, W.L. and L.K. Leung. "Feature motivated polarization scattering matrix decomposition". *Proc. IEEE Radar Conf.*, 549–557, 1990.

[21] Cameron, W.L. and H. Rais. "Polarization symmetric scatterer metric space". *IEEE Trans. Geosci. Remote Sens.*, 47(4):1097, 2009.

[22] Cantalloube, H. and E.K. Colin. "POLINSAR for FOPEN using flashlight mode images along circular trajectories". *Proc. IEEE Geosci. Remote Sens. Symposium*, 1139–1142. Barcelona, Spain, July 2007.

[23] Cantalloube, H.M.J., E. Colin-Koeniguer, and H. Oriot. "High resolution SAR imaging along circular trajectories". *Proc. IEEE Geosci. Remote Sens. Symposium*, 850–853. Barcelona, Spain, July 2007.

[24] Carrara, W.G., R.S. Goodman, and R.M. Majewski. *Spotlight Synthetic Aperture Radar: Signal Processing Algorithms*. Artech House, Inc., Norwood, MA, 1995.

[25] Casteel Jr, C.H., L.R.A. Gorham, M.J. Minardi, S.M. Scarborough, K.D. Naidu, and U.K. Majumder. "A challenge problem for 2D/3D imaging of targets from a volumetric data set in an urban environment". *Proc. SPIE Algorithms for Synthetic Aperture Radar Imagery XIV*, volume 6568. Orlando, FL, May 2007.

[26] Chaney, R.D., A.S. Willsky, and L.M. Novak. "Coherent aspect-dependent SAR image formation". *Proc. SPIE Algorithms for Synthetic Aperture Radar Imagery XIV*, volume 2230, 256–274. Apr 1994.

[27] Chauveau, J., N. de Beaucoudrey, and J. Saillard. "Selection of contributing natural poles for the characterization of perfectly conducting targets in resonance region". *IEEE Trans. Antennas and Prop.*, 55(9):2610–2617, 2007.

[28] Chen, V.C. and H. Ling. *Time-frequency transforms for radar imaging and signal analysis*. Artech House, Inc., Norwood, MA, 2002.

[29] Cheney, M. and B. Borden. "Problems in synthetic-aperture radar imaging". *Inverse Prob.*, 25:123005, 2009.

[30] Chiang, H.-C., R.L. Moses, and L.C. Potter. "Model-based classification of radar images". *IEEE Trans. Inf. Theory*, 46(5):1842–1854, Aug 2000.

[31] Chiang, H.C., R.L. Moses, and L.C. Potter. "Model-based Bayesian feature matching with application to synthetic aperture radar target recognition". *Pattern Recognit.*, 34(8):1539–1553, 2001.

[32] Clapper, J.R., Jr. Young J.J., J.E. Cartwright, J.G. Grimes, S.C. Payton, S.J. Stackley, and D. Popps. *Unmanned Systems Integrated Roadmap, 2009-2034*. Technical report, United States Department of Defense, Washington, DC, 2009.

[33] Cloude, S.R. and E. Pottier. "A review of target decomposition theorems in radar polarimetry". *IEEE Trans. Geosci. Remote Sens.*, 34(2):498–518, 1996.

[34] Collins, P.J. "RCS analysis, measurement, and reduction". EENG 627 Course Notes, Air Force Institute of Technology, Wright-Patterson AFB, OH, 2009.

[35] Crisp, D.J., N.J.S. Stacy, D.A. Hudson, P.B. Pincus, and A.S. Goh. "Polarimetric analysis of maritime SAR data collected with the DSTO Ingara X-Band radar". *IEEE Geosci. Remote Sens. Symposium*, 3870–3873. Barcelona, Spain, July 2007.

[36] Cumming, I.G. and F.H. Wong. *Digital Processing of Synthetic Aperture Radar Data: Algorithms and Implementation*. Artech House, Inc., Norwood, MA, 2005.

[37] Curlander, J.C. and R.N. McDonough. *Synthetic Aperture Radar: Systems and Signal Processing*. John Wiley & Sons, Inc., New York, NY, 1991.

[38] Defense Advanced Reseach Projects Agency and Air Force Research Laboratory. "MSTAR public clutter". Sensor Data Management System, `https://www.sdms.afrl.af.mil/index.php?collection=mstar\&page=clutter`, 1995.

[39] DeGraaf, S.R. "SAR imaging via modern 2-D spectral estimation methods". *IEEE Trans. Image Process.*, 7(5):729 –761, May 1998.

[40] Desai, M.D. and W.K. Jenkins. "Convolution backprojection image reconstruction for spotlight mode synthetic aperture radar". *IEEE Trans. Image Processing*, 1(4):505–517, Oct 1992.

[41] Di Bisceglie, M., M. Di Santo, C. Galdi, R. Lanari, and N. Ranaldo. "Synthetic Aperture Radar Processing with GPGPU". *IEEE Signal Processing Mag.*, 27(2):69–78, 2010.

[42] Duan, G. Q., D. W. Wang, X. Y. Ma, and Y. Su. "Three-dimensional imaging via wideband MIMO radar system". *IEEE Geosci. Remote Sens. Letters*, 7(3):445–449, July 2010.

[43] Dudgeon, D.E., R.T. Lacoss, C.H. Lazott, and J.G. Verly. "Use of persistent scatterers for model-based recognition". *Proc. SPIE*, 2230:356, 1994.

[44] Dungan, K.E. and L.C. Potter. "Classifying civilian vehicles using a wide-field circular SAR". *Proc. SPIE Algorithms for Synthetic Aperture Radar Imagery XVI*, volume 7337, 73370R. Orlando, FL, Apr 2009.

[45] Dungan, K.E. and L.C. Potter. "Classifying transformation-variant attributed point patterns". *Pattern Recognit.*, 43(11):3805–3816, Nov 2010.

[46] Duquenoy, M., J.P. Ovarlez, L. Ferro-Famil, and E. Pottier. "Hyperimage concept: multidimensional time-frequency analysis applied to SAR imaging". *Proc. IEEE Geosci. Remote Sens. Symposium*, volume 4, IV–414 – IV–417. Cape Town, South Africa, July 2009.

[47] Duquenoy, M., J.P. Ovarlez, L. Ferro-Famil, E. Pottier, and L. Vignaud. "Characterization of scatterers by their anisotropic and dispersive behavior". *Proc. IEEE Geosci. Remote Sens. Symposium*, 5186–5189, July 2007.

[48] Duquenoy, M., J.P. Ovarlez, L. Vignaud, L. Ferro-Famil, and E. Pottier. "Classification based on the polarimetric dispersive and anisotropic behavior of scatterers". *Proc. Workshop on Science and Applications of SAR Polarimetry and Polarimetric Interferometry*, 22–26. Frascati, Italy, January 2007.

[49] E., Emre, Christian D. A., Samir S., Randolph L. M., and Lee C. P. "GOTCHA experience report: three-dimensional SAR imaging with complete circular apertures". *Proc. SPIE Algorithms for Synthetic Aperture Radar Imagery XIV*, volume 6568. Orlando, FL, May 2007.

[50] Ertin, E. and L.C. Potter. "Polarimetric classification of scattering centers using M-ary Bayesian decision rules". *IEEE Trans. Aerosp. Electron. Syst.*, 36(3 Part 1):738–749, 2000.

[51] Ferro-Famil, L., A. Reigber, E. Pottier, and W.M. Boerner. "Scene characterization using subaperture polarimetric SAR data". *IEEE Trans. Geosci. Remote Sens.*, 41(10):2264–2276, 2003.

[52] Franceschetti, G. and R. Lanari. *Synthetic Aperture Radar Processing*. CRC Press, Boca Raton, FL, 1999.

[53] Freedman, A., R. Bose, and B.D. Steinberg. "Techniques to improve the CLEAN deconvolution algorithm". *J. Franklin Inst.*, 332(5):535–553, 1995.

[54] Fuller, D.F. *How to develop a robust automatic target recognition capability by the year 2030*. Technical report, Air University, Maxwell AFB, AL, 2008.

[55] Fuller, D.F. and M.A. Saville. "Rapid extraction of doubly-curved scattering centers for automobile detection in the presence of clutter". *Proc. IEEE Radar Conference*, 2009.

[56] Fuller, D.F. and M.A. Saville. "The spectrum parted linked image test (SPLIT) algorithm for estimating the frequency dependence of scattering center amplitudes". *Proc. SPIE Algorithms for Synthetic Aperture Radar Imagery XVI*, volume 7337. Orlando, FL, Apr 2009.

[57] Fuller, D.F. and M.A. Saville. "Classification of canonical scattering through sub-band analysis". *Proc. SPIE Algorithms for Synthetic Aperture Radar Imagery XVII*, volume 7699. Orlando, FL, Apr 2010.

[58] Fuller, D.F. and M.A. Saville. "A High-frequency Multi-peak Model for Wide Wide-Angle SAR Imagery". *IEEE Trans. Geosci. Remote Sens.*, 2011 submitted.

[59] Fuller, D.F. and M.A. Saville. "Efficient Integration of Imaging and Classification Algorithms for Circular SAR". *IEEE Trans. Aerosp. Electron. Syst.*, 2011 submitted.

[60] Gabor, D. "Theory of communication. Part 1: The analysis of information". *J. Inst. Elect. Eng.*, 93(26):429–441, Nov 1946.

[61] Garzón-Guerrero, J.A., D. Salas-González, D.P. Ruiz, and M.C. Carrión. "Neural networks and principal component analysis applied to automatic radar target recognition based on naturel resonances". *Int. J. Comput. Sci. Appl.*, 5(3a):49–56, 2008.

[62] Gerry, M.J., L.C. Potter, I.J. Gupta, and A. Van Der Merwe. "A parametric model for synthetic aperture radar measurements". *IEEE Trans. Antennas and Prop.*, 47(7):1179–1188, July 1999.

[63] Gini, F. and M. Rangaswamy. *Knowledge Based Radar Detection, Tracking and Classification*. Wiley-Interscience, New York, NY, 2008.

[64] Gorham, L.A. and L.J. Moore. "SAR image formation toolbox for MATLAB". *Proc. SPIE Algorithms for Synthetic Aperture Radar Imagery XVII*, volume 7699. Orlando, FL, 2010.

[65] Gorham, L.A., Majumder U.K., P. Buxa, Backues M.J., and Lindgren A.C. "Implementation and analysis of a fast backprojection algorithm". *Proc. SPIE Algorithms for Synthetic Aperture Radar Imagery XIII*, volume 6237. Orlando, FL, Apr 2006.

[66] Hack, D.E. and M.A. Saville. "Verification of target motion effects on SAR imagery using the Gotcha GMTI challenge dataset". *Proc. IEEE Algorithms for Synthetic Aperture Radar Imagery XVII*, volume 7699. Apr 2010.

[67] Harris, F.J. "On the use of windows for harmonic analysis with the discrete Fourier transform". *Proc. IEEE*, 66(1):51–83, 1978.

[68] Hartley, T.D.R., A.R. Fasih, C.A. Berdanier, F. Ozguner, and U.V. Catalyurek. "Investigating the use of GPU-accelerated nodes for SAR image formation". *Proc. IEEE Cluster Computing Conf.*, 1–8. New Orleans, LA, September 2009.

[69] Hellsten, H., Ulander L.M., , Gustavsson A., and Bjoern L. "Development of VHF CARABAS II SAR". *Proc. SPIE Radar Sensor Technology*, volume 2747, 48–60. Orlando, FL, Apr. 1996.

[70] Hinz, S., D. Weihing, S. Suchandt, and R. Bamler. "Detection and velocity estimation of moving vehicles in high-resolution spaceborne synthetic aperture radar data". *IEEE Computer Vision and Pattern Recog. Workshop*, 1–6. June 2008.

[71] Huynen, J.R. *Phenomenological theory of radar targets*. Ph.D. thesis, Drukkerij Bronder-Offset NV, Rotterdam, 1970.

[72] Ince, T. "Unsupervised classification of polarimetric SAR image with dynamic clustering: An image processing approach". *Adv. Eng. Software*, 41(4):636–646, 2010.

[73] Jackson, J.A. *Three-Dimensional Feature Models for Synthetic Aperture Radar and Experiments in Feature Extraction*. Ph.D. thesis, The Ohio State University, Columbus, OH, 2009.

[74] Jackson, J.A. and R.L. Moses. "Identifiability of 3D attributed scattering features from sparse nonlinear apertures". *Proc. SPIE*, 6568:24, 2007.

[75] Jackson, J.A., B.D. Rigling, and R.L. Moses. "Canonical scattering feature models for 3D and bistatic SAR". *IEEE Trans. Aerosp. Electron. Syst.*, 46(2):525–541, Apr 2010.

[76] Jakowatz Jr., C.V., D.E. Wahl, P.H. Eichel, D.C. Ghiglia, and P.A. Thompson. *Spotlight-mode Synthetic Aperture Radar: a Signal Processing Approach*. Kluwer Academic Pub., Boston, MA, 1996.

[77] Jouny, I. "Compressed Sensing for UWB Radar Target Signature Reconstruction". *IEEE 13th Digital Signal Process. Workshop*, 714–719. Jan 2009.

[78] Keller, J.B. "Geometrical Theory of Diffraction". *J. Opt. Soc. Am*, 52:116–130, 1962.

[79] Kennaugh, E. M. and D. L. Moffatt. "Transient and impulse response approximations". *Proc. IEEE*, 53(8):893–901, 1965.

[80] Keydel, E.R., S.W. Lee, and J.T. Moore. "MSTAR extended operating conditions: a tutorial". *Proc. SPIE Algorithms for Synthetic Aperture Radar Imagery III*, 2757:228–242, 1996.

[81] Kim, A.J., J.W. Fisher, and A.S. Willsky. "Detection and analysis of anisotropic scattering in SAR data". *Multidimension. Syst. Signal Process.*, 14(1):49–82, 2003.

[82] Knittle, C.D., N.E. Doren, and C.V. Jakowatz. *A Comparison of Spotlight Synthetic Aperture Radar Image Formation Techniques.* Technical report, Sandia National Labs, Albuquerque, NM, 1996.

[83] Knott, E.F., J.F. Shaeffer, and M.T. Tuley. *Radar Cross Section.* Artech House, Inc., Norwood, MA, 1993.

[84] Kouyoumjian, R.G. and P.H. Pathak. "A uniform geometrical theory of diffraction for an edge in a perfectly conducting surface". *Proc. IEEE*, 62(11):1448–1461, Nov. 1974.

[85] Krishnapuram, B., J. Sichina, and L. Carin. "Physics-based detection of targets in SAR imagery using support vector machines". *IEEE Sensors Journal*, 3(2):147–157, 2003.

[86] Krogager, E. "New decomposition of the radar target scattering matrix". *Electronics Letters*, 26(18):1525, 1990.

[87] Krogager, E. "Decomposition of the radar target scattering matrix with application to high resolution target imaging". *Proc. IEEE*, 1:77–82, 1991.

[88] Krogager, E. "Advances of techniques for utilizing polarimetric features of radar targets". *NATO RTO SET Symposium on Target ID & Recog. Using RF Syst.*, volume 080-40, 1–8. Oct. 2004.

[89] Kushiyama, K. "High-tech radar cuts through the "foliage"". *Headline News, U.S. Army RDECOM*, 7 June 2010.

[90] Lee, J.S., W.M. Boerner, D.L. Shuler, T.L. Ainsworth, I. Hajnsek, K.P Papathoanossiou, and E. Lüneburg. "A review of polarimetric SAR algorithms and their applications". *ISPRS J. Photogramm. Remote Sens.*, 9(3):31–80, 2004.

[91] Lee, J.S., E. Krogager, D.L. Schuler, T.L. Ainsworth, and W.M. Boerner. "On the estimation of polarization orientation angles induced from azimuth slopes using polarimetric SAR data". *Proc. IEEE Geosci. Remote Sens. Symposium*, volume 3, 1310–1312. Aug. 2000.

[92] Lee, J.S. and E. Pottier. *Polarimetric Radar Imaging: from Basics to Applications*. CRC Press, Boca Raton, FL, 2009.

[93] Levanon, N. and E. Mozeson. *Radar Signals*. John Wiley & Sons, Inc., Hoboken, NJ, 2004.

[94] Liang, Jing and Qilian Liang. "Sense-through-foliage target detection using UWB radar sensor networks". *Pattern Recogn. Letters*, 31(11):1412 – 1421, 2010.

[95] Lighthill, M.J. *Introduction to Fourier Analysis and Generalized Functions*. Cambridge University Press, Cambridge, UK, 1958.

[96] Liu, Qi, Yun Lin, Weixian Tan, Yanping Wang, Wen Hong, and Yirong Wu. "Study on SAR image formation for aspect-dependent scatterers". *Asian Pacific Conf. on SAR*, 451–454. Oct 2009.

[97] Livingstone, C.E., A.L. Gray, R.K. Hawkins, and R.B. Olsen. "CCRS C/X-airborne synthetic aperture radar: An R&D tool for the ERS-1 time frame". *IEEE Aerosp. Electron. Syst. Mag.*, 3(10):11–20, Oct 1988.

[98] Lou, Y., Y. Kim, and J. Vanzyl. "The NASA/JPL airborne synthetic aperture radar system". *Sixth Annual JPL Airborne Earth Science Workshop*, 51–56. Mar. 1996.

[99] Majumder, U., M. Soumekh, M. Minardi, S. Scarborough, L. Gorham, C. Casteel, M. Judge, and J. Kirk. "Synthetic aperture radar moving target indication processing of along-track monopulse nonlinear Gotcha data". *Proc. IEEE Radar Conf.*, 1–6. Pasadena, CA, Apr 2009.

[100] Martorella, M., N. Acito, and F. Berizzi. "Statistical CLEAN technique for ISAR imaging". *IEEE Trans. Geosci. Remote Sens.*, 45(11 Part 1):3552–3560, 2007.

[101] Martorella, M., E. Giusti, A. Capria, F. Berizzi, and B. Bates. "Automatic target recognition by means of polarimetric ISAR images and neural networks". *IEEE Trans. Geosci. Remote Sens.*, 47(11):3786–3794, November 2009.

[102] McCall, G.H. and J.A. Corder. *New World Vistas: Air and Space Power for the 21st Century, Sensors Volume*. Technical report, United States Air Force Scientific Advisory Board, Washington, DC, 1996.

[103] McCorkle, J.W. and Rofheart M. "Order $N^2 \log(N)$ backprojector algorithm for focusing wide-angle wide-bandwidth arbitrary-motion synthetic aperture radar". *Proc. SPIE Radar Sensor Technology*, volume 2747, 25–36. Orlando, FL, Apr 1996.

[104] McShane, J. *Application of Time-frequency Representations to Non-stationary Radar Cross Section*. Master's thesis, Air Force Institute of Technology, Wright-Patterson AFB, OH, 2009.

[105] Menon, R.K., N. Balakrishnan, and K. Ramchand. "Discriminating complex bodies with minor variations using E-pulse". *IEEE Trans. Aerosp. Electron. Syst.*, 44(1):408–416, 2008.

[106] Miller, E.K. and T.K. Sarkar. "An introduction to the use of model-based parameter estimation in Electromagnetics". accessed online 1 Apr 2010, http://www.cis.syr.edu/~tksarkar/pdf/1999_Aug_2.pdf, 1999.

[107] Morrison, N. *Introduction to Fourier Analysis*. John Wiley and Sons, New York, NY, 1994.

[108] Moses, R.L. "Model-based imaging and feature extraction for synthetic aperture radar". Presentation at Univ. of Minnesota Inst. for Mathematica and Its Applications, 18 Oct 2005.

[109] Moses, R.L. and J.N. Ash. "Recursive SAR imaging". *Proc. SPIE Algorithms for Synthetic Aperture Radar Imagery XV*, volume 6970. Orlando, FL, Mar 2008.

[110] Moses, R.L., L.C. Potter, and M. Çetin. "Wide-angle SAR imaging". *Proc. SPIE Algorithms for Synthetic Aperture Radar Imagery XI*, volume 5427, 164–175. April 2004.

[111] Moses, R.L., L.C. Potter, and I.J. Gupta. *Feature Extraction Using Attributed Scattering Center Models for Model-Based Automatic Target Recognition (ATR)*. Technical report, The Ohio State University, Columbus, OH, 2005.

[112] Mott, H. *Remote Sensing with Polarimetric Radar*. IEEE Press; Wiley-Interscience, Los Alamitos, CA; Hoboken, NJ, 2007.

[113] Munson, Jr., D.C. and J.L.C. Sanz. "Image reconstruction from frequency-offset Fourier data". *Proc. IEEE*, 72(6):661–669, June 1984.

[114] Nichols, A.D., J.W. Wilhelm, T.W. Gaffield, D.R. Inkster, and S.K. Leung. "A SAR for Real-Time Ice Reconnaissance". *IEEE Trans. Geosci. Remote Sens.*, GE-24(3):383–389, May 1986.

[115] O'Hanlon, M.E. *Technological Change and the Future of Warfare*. Brookings Institution Press, Washington, DC, 2000.

[116] Oliver, C. and S. Quegan. *Understanding Synthetic Aperture Radar Images*. SciTech Publishing, Raleigh, NC, 2004.

[117] Perissin, D. and A. Ferretti. "Urban-Target Recognition by Means of Repeated Spaceborne SAR Images". *IEEE Trans. Geosci. Remote Sens.*, 45(12):4043 –4058, Dec. 2007.

[118] Perlovsky, L., R. Ilin, R. Deming, R. Linnehan, and F. Lin. "Moving target detection and characterization with circular SAR". *Proc. IEEE Radar Conf.*, 661–666. Washington, D.C., May 2010.

[119] Perlovsky, L.I. "Conundrum of combinatorial complexity". *IEEE Trans. Pattern Anal. Mach. Intell.*, 20(6):666–670, 1998.

[120] Plato, R. *Concise Numerical Mathematics*. American Mathematical Society, Providence, RI, 2003.

[121] Potter, L.C., D.M. Chiang, R. Carriere, and M.J. Gerry. "A GTD-based parametric model for radar scattering". *IEEE Trans. Antennas and Prop.*, 43(10):1058–1067, 1995.

[122] Potter, L.C., E. Ertin, J.T. Parker, and M. Çetin. "Sparsity and compressed sensing in radar imaging". *Proc. IEEE*, 98(6):1006–1020, June 2010.

[123] Potter, L.C. and R.L. Moses. "Attributed scattering centers for SAR ATR". *IEEE Trans. Image Process.*, 6(1):79–91, 1997.

[124] Potter, L.C., J.W. Nehrbass, and K.E. Dungan. *CVDomes: A Data Set of Simulated X-band Signatures of Civilian Vehicles*. Technical report, Air Force Research Laboratory, Wright-Patterson AFB, OH, 2009.

[125] Rau, R., JH McClellan, L. Technol, and G. Nuremberg. "Analytic models and postprocessing techniques for UWB SAR". *IEEE Trans. Aerosp. Electron. Syst.*, 36(4):1058–1074, 2000.

[126] Rigling, B.D. "Image-Quality Focusing of Rotating SAR Targets". *IEEE Geosci. Remote Sens. Letters*, 5(4):750–754, Oct. 2008.

[127] Rogers, S.K., C. Sadowski, K.W. Bauer, M.E. Oxley, M. Kabrisky, A. Rogers, and S.D. Mott. "The life and death of ATR/sensor fusion and the hope for resurrection". *Proc. SPIE Automatic Target Recognition XVIII*, 6967:696702, May 2008.

[128] Rosen, P.A., S. Hensley, K. Wheeler, G. Sadowy, T. Miller, S. Shaffer, R. Muellerschoen, C. Jones, H. Zebker, and S. Madsen. "UAVSAR: a new NASA airborne SAR system for science and technology research". *Radar, 2006 IEEE Conference on*, 22–29. Apr. 2006.

[129] Rosenqvist, A., M. Shimada, N. Ito, and M. Watanabe. "ALOS PALSAR: A pathfinder mission for global-scale monitoring of the environment". *IEEE Trans. Geosci. Remote Sens.*, 45(11):3307–3316, Nov. 2007.

[130] Runkle, P., LH Nguyen, JH McClellan, and L. Carin. "Multi-aspect target detection for SAR imagery using hidden Markov models". *IEEE Trans. Geosci. Remote Sens.*, 39(1):46–55, Jan. 2001.

[131] Schuler, K., D. Becker, and W. Wiesbeck. "Extraction of virtual scattering centers of vehicles by ray-tracing simulations". *IEEE Trans. Antennas and Prop.*, 56(11):3543–3551, Nov 2008.

[132] Sheen, D.R., S.J. Shackman, N.L. VandenBerg, D.L. Wiseman, L.P. Elenbogen, and R.F. Rawson. "The P-3 ultra-wideband SAR: description and examples". *Proc. IEEE Radar Conference*, 50–53. May 1996.

[133] Skolnik, M.I. *Introduction to Radar Systems, 3rd Ed.* McGraw-Hill, Inc., Boston, MA, 2001.

[134] Soumekh, M. "Reconnaissance with ultra wideband UHF synthetic aperture radar". *IEEE Signal Processing Magazine*, 12(4):21–40, 1995.

[135] Soumekh, M. *Synthetic Aperture Radar Signal Processing with MATLAB Algorithms*. Wiley-Interscience, Hoboken, NJ, 1999.

[136] Spigai, M., C. Tison, and J.C. Souyris. "Time-frequency analysis of point target behaviour in high resolution single polarization SAR images". *Proc. European Conf. on Synthetic Aperture Radar*. Friedrichshaffen, Germany, May 2008.

[137] Stojanovic, I., M. Çetin, and W.C. Karl. "Joint space aspect reconstruction of wide-angle SAR exploiting sparsity". *Proc. SPIE Algorithms for Synthetic Aperture Radar Imagery XV*, volume 6970, 697005. Mar 2008.

[138] Sullivan, R.J. *Radar foundations for imaging and advanced concepts*. Artech House, Boston, MA, 2004.

[139] Touzi, R. "Target scattering decomposition in terms of roll-invariant target parameters". *IEEE Trans. Geosci. Remote Sens.*, 45(1):73–84, 2007.

[140] Touzi, R., W.M. Boerner, J.S. Lee, and E. Lueneburg. "A review of polarimetry in the context of synthetic aperture radar: concepts and information extraction". *Can. J. Remote Sensing*, 30(3):380–407, 2004.

[141] Tsao, J. and B.D. Steinberg. "Reduction of sidelobe and speckle artifacts in microwave imaging: the CLEAN technique". *IEEE Trans. Antennas and Prop.*, 36(4):543–556, 1988.

[142] Tso, B. and P.M. Mather. *Classification Methods for Remotely Sensed Data*. CRC Press, Boca Raton, FL, 2001.

[143] Ulander, L.M.H., M. Blom, B. Flood, P. Follo, P.-O. Frolind, A. Gustavsson, T. Jonsson, B. Larsson, D. Murdin, M. Pettersson, U. Raaf, and G. Stenstrom. "Development of the ultra-wideband LORA SAR operating in the VHF/UHF-band". *GProc. IEEE Geosci. Remote Sens. Symposium*, volume 7, 4268–4270. July 2003.

[144] Varshney, K.R., M. Çetin, J.W. Fisher III, and A.S. Willsky. "Sparse representation in structured dictionaries with application to synthetic aperture radar". *IEEE Trans. on Signal Process.*, 56(8), 2008.

[145] Vu, Viet Thuy, T.K. Sjogren, M.I. Pettersson, A. Gustavsson, and L.M.H. Ulander. "Detection of moving targets by focusing in UWB SAR - theory and experimental results". *IEEE Trans. Geosci. Remote Sens.*, 48(10):3799–3815, Oct. 2010.

[146] Vu, V.T., T.K. Sjogren, M.I. Pettersson, and H. Hellsten. "An Impulse Response Function for Evaluation of UWB SAR Imaging". *IEEE Trans. Signal Process.*, 58(7):3927–3932, July 2010.

[147] Wang, B. and T.O. Binford. "Generic, model-based estimation and detection of peaks in image surfaces". *Proc. DARPA Image Understanding Workshop*, volume 2, 913–922. 1996.

[148] Werninghaus, R. and S. Buckreuss. "The TerraSAR-X mission and system design". *IEEE Trans. Geosci. Remote Sens.*, 48(2):606–614, Feb. 2010.

[149] Williams, W., E. Keydel, and S. McCarty. "Model-based multisource fusion for exploitation, classification, and recognition". *Proc. SPIE Signal Process., Sensor Fusion, and Target Recog. XV*, volume 6235, 62350. Orlando, FL, Apr. 2006.

[150] Xu, X., L. Zhai, and Y. Huang. "Subpixel processing for target scattering center extraction from SAR images". *IEEE Conf. Signal Proces.*, volume 4. Nov. 2006.

[151] Zaugg, E., M. Edwards, and A. Margulis. "Developing a small multi frequency synthetic aperture radar for UAS operation: the SlimSAR". *Proc. SPIE Radar Sensor Technology XIV*, volume 7669. Orlando, Florida, Apr 2010.

[152] Zhang, Lei, Mengdao Xing, Cheng-Wei Qiu, Jun Li, Jialian Sheng, Yachao Li, and Zheng Bao. "Resolution enhancement for inversed synthetic aperture

radar imaging under low SNR via improved compressive sensing". *IEEE Trans. Geosci. Remote Sens.*, 48(10):3824–3838, Oct 2010.

[153] Zhou, Jianxiong, Hongzhong Zhao, Zhiguang Shi, and Qiang Fu. "Global scattering center model extraction of radar targets based on wideband measurements". *IEEE Trans. Antennas and Prop.*, 56(7):2051–2060, July 2008.

[154] Zou, T., W. Yang, D. Dai, and H. Sun. "Polarimetric SAR image classification using multifeatures combination and extremely randomized clustering forests". *EURASIP J. Adv. Signal Process.*, 2010.

REPORT DOCUMENTATION PAGE

Form Approved
OMB No. 0704–0188

1. REPORT DATE *(DD–MM–YYYY)*	2. REPORT TYPE	3. DATES COVERED *(From — To)*
15–09–2011	Doctoral Dissertation	Sep 2008 — Sep 2011

4. TITLE AND SUBTITLE

Phase History Decomposition for Efficient Scatterer Classification in SAR Imagery

5a. CONTRACT NUMBER

5b. GRANT NUMBER

5c. PROGRAM ELEMENT NUMBER

6. AUTHOR(S)

Fuller, Dane F., LtCol, USAF

5d. PROJECT NUMBER

5e. TASK NUMBER

5f. WORK UNIT NUMBER

7. PERFORMING ORGANIZATION NAME(S) AND ADDRESS(ES)

Air Force Institute of Technology
Graduate School of Engineering and Management (AFIT/EN)
2950 Hobson Way
WPAFB OH 45433-7765

8. PERFORMING ORGANIZATION REPORT NUMBER

AFIT/DEE/ENG/11-09

9. SPONSORING / MONITORING AGENCY NAME(S) AND ADDRESS(ES)

Not Disclosed

10. SPONSOR/MONITOR'S ACRONYM(S)

11. SPONSOR/MONITOR'S REPORT NUMBER(S)

12. DISTRIBUTION / AVAILABILITY STATEMENT

APPROVED FOR PUBLIC RELEASE; DISTRIBUTION UNLIMITED.

13. SUPPLEMENTARY NOTES

14. ABSTRACT

A new theory and algorithm for scatterer classification in SAR imagery is presented. The automated classification process is operationally efficient compared to existing image segmentation methods requiring human supervision.

The algorithm reconstructs coarse resolution subimages from subdomains of the SAR phase history. It analyzes local peaks in the subimages to determine locations and geometric shapes of scatterers in the scene. Scatterer locations are indicated by the presence of a stable peak in all subimages for a given subaperture, while scatterer shapes are indicated by changes in pixel intensity. A new multi-peak model is developed from physical models of electromagnetic scattering to predict how pixel intensities behave for different scatterer shapes. The algorithm uses a least squares classifier to match observed pixel behavior to the model. Classification accuracy improves with increasing fractional bandwidth and is subject to the high-frequency and wide-aperture approximations of the multi-peak model.

For superior computational efficiency, an integrated fast SAR imaging technique is developed to combine the coarse resolution subimages into a final SAR image having fine resolution. Finally, classification results are overlaid on the SAR image so that analysts can deduce the significance of the scatterer shape information within the image context.

15. SUBJECT TERMS

Synthetic Aperture Radar, Radar Imaging, Electromagnetic Scattering, Scattering Model, Scatterer Classification, Domain Decomposition, Target Classification, Time-Frequency Analysis

16. SECURITY CLASSIFICATION OF:			17. LIMITATION OF ABSTRACT	18. NUMBER OF PAGES	19a. NAME OF RESPONSIBLE PERSON
a. REPORT	b. ABSTRACT	c. THIS PAGE			Professor Michael A. Saville (ENG)
U	U	U	UU	194	19b. TELEPHONE NUMBER *(include area code)* (937) 255-2024; Michael.Saville@.wpafb.af.mil